



Defence Research and
Development Canada

Recherche et développement
pour la défense Canada



Advanced beamformers for 3D ultrasound systems deploying linear and planar phased array probes

*Stergios Stergiopoulos
Amar Dhanantwari*

DISTRIBUTION STATEMENT A
Approved for Public Release
Distribution Unlimited

Defence R&D Canada – Toronto
Technical Report
DRDC Toronto TR 2002-058
May 2002

Canada

20030129 150

Advanced beamformers for 3D ultrasound systems deploying linear and planar phased array probes

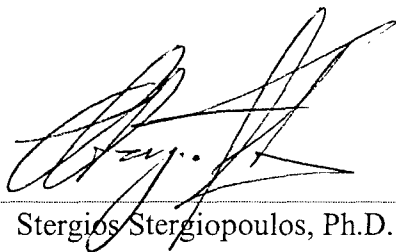
Stergios Stergiopoulos
Amar Dhanantwari

Defence R&D Canada – Toronto

Technical Report

DRDC Toronto TR 2002-058

May 2002



Stergios Stergiopoulos, Ph.D.

Author



Amar Dhanantwari, Ph.D.

Approved by



Pang Shek, PhD

Head, Operational Medicine Section

Approved for release by



K.M. Sutton

Chair, Document Review and Library Committee

Abstract

The present report outlines the development of an advanced digital ultrasound imaging technology leading to a next-generation field-portable 4D diagnostic imaging system. The proposed technology consists of:

- Adaptive beamforming algorithms to provide high image-resolution for ultrasound diagnostic systems;
- 3D visualization imaging techniques to assist imaging during field-deployable minimally invasive operations;
- time-reversal pulse design for ultrasound signals to eliminate aberration effects, which cause fuzziness in reconstructed ultrasound images; and
- investigations on computing architectures and planar ultrasound sensor arrays allowing system integration of the proposed technologies as a compact-portable system for field-deployable operations.

The aim is to investigate a new ultrasonic sensing and imaging technology that would lead to the design of portable, compact and field deployable 3D ultrasound diagnostic systems. The performance characteristics of the proposed diagnostic systems include minimization of the aberration effects and significant improvement in image resolution to allow for tissue identification and 3D tomographic imaging of internal body-organs. The adaptive processing schemes of this study are characterized as Dual-Use technologies and have been tested in operational active sonars of the Canadian Navy. Real data results have shown that they provide array gain improvements for signals embedded in anisotropic noise fields, similar to those in the human body.

Résumé

Le présent rapport traite de la mise au point d'une technologie d'imagerie à ultrasons numérique évoluée en vue de créer un système d'imagerie 4D de prochaine génération pouvant être utilisé sur place à des fins de diagnostic. La technologie proposée comprend les travaux suivants :

- techniques de formation de faisceaux adaptatives [1-6] permettant de créer des images à haute résolution pour les systèmes de diagnostic à ultrasons;
- techniques d'imagerie 3D afin de faciliter l'imagerie durant les opérations avec effraction minimale effectuées sur place;
- concept d'impulsions à inversion temporelle pour les signaux ultrasons afin d'éliminer les effets d'aberration, qui rendent floues les images reconstruites des échographies;
- études sur les architectures informatiques et les réseaux plans de capteurs d'ultrasons afin de permettre l'intégration des technologies proposées dans un système portable compact utilisable pour les opérations sur place.

Notre objectif consiste à étudier une nouvelle technologie de détection et d'imagerie ultrasoniques qui permettrait de concevoir des systèmes à ultrasons 3D portatifs, compacts et utilisables sur place aux fins de diagnostic. Les caractéristiques de performance des systèmes de diagnostic proposés comprendraient la réduction des effets d'aberration et une amélioration considérable de la résolution des images afin de permettre l'identification des tissus et l'imagerie tomographique 3D des organes internes du corps. Les techniques de traitement adaptatif utilisées dans la présente étude sont appelées technologies à double usage et ont été mises à l'essai dans des sonars actifs opérationnels de la Marine canadienne [1,4-6]. Les résultats obtenus en situation réelle ont démontré que ces techniques permettent d'améliorer dans les réseaux le gain des signaux incorporés dans des champs sonores anisotropes similaires à ceux qu'on retrouve dans le corps humain.

Executive summary

The aim of this report is to bring together some of the most recent theoretical developments on ultrasound beamformers; and provide suggestions of how modern technology can be applied to the development of current and next generation 3D ultrasound systems. It will focus on the development of an advanced beamforming structure that allows the implementation of adaptive and synthetic aperture signal processing techniques in ultrasound systems deploying multi-dimensional arrays of sensors.

The primary objective is to develop an Ultrasonic Sensing and Imaging Technology that will facilitate non-invasive medical imaging for treatment assessment of injured CF personnel, combat casualties, and victims rescued during search and rescue operations. The requirements for non-invasive medical diagnostic procedures can be addressed with the development of compact, portable and field-deployable 3D ultrasound medical imaging systems. Because imaging is of critical importance in facilitating rapid diagnosis and therapy, the major manufacturers of imaging equipment are introducing CT & MRI machines that allow surgical procedures to be performed under direct imaging using minimally invasive techniques. However, these imaging approaches are expensive and would occupy a complete surgical suite. Unlike CT or MRI, which are often located in dedicated suites specifically built to accommodate their needs, ultrasound is a much cheaper and more flexible imaging modality that can be deployed in remote and harsh operational areas of interest to the CF. Moreover, in contrast with clinical CT and MRI, ultrasound systems allow the surgeon or therapist to see what is happening as it occurs, in real time. However, even the most-advanced state-of-the-art medical ultrasound imaging systems suffer from very poor image resolution, which is the result of the very small size of deployed arrays of sensors and the distortion effects caused by the human-body's non-linear propagation characteristics. In summary, the existing ultrasound imaging technology is not field-deployable and incapable of delivering high-quality images.

The development of an advanced 4-Dimensional (4D, i.e. 3D + Time) ultra-sound system technology, detailed in the present report, addresses ultrasound requirements for high-image resolution capabilities with small size arrays for medical diagnostic and non-destructive system applications. The present investigation has been supported by the Technology Investment Fund of Defence R&D Canada (DRDC) and two European-Canadian collaborative projects entitled: "MITTUG: (Minimally Invasive Tumour Therapy 3D Ultrasound Guided)" and "ADUMS: (Adaptive 4D Processing for Digital Ultrasound Medical Systems)" that have been awarded with funds from the European Commission Fifth Framework IST program.

In summary, it is anticipated that the results of our 4D ultra-sound system technology would provide a major support in terms of innovation to the emerging Canadian ultra-sound industrial sector, since the anticipated high image resolution capabilities can be exploited by other medical imaging diagnostic and non-destructive system applications.

Stergios Stergiopoulos and Amar Dhanantwari, 2002, Advanced beamformers for 3D ultrasound systems deploying linear and planar phased array probes, TR 2002-058, DRDC Toronto

Sommaire

Le présent rapport vise à rassembler certaines des avancées théoriques les plus récentes dans le domaine des conformateurs de faisceaux ultrasonores et de suggérer des façons dont la technologie moderne peut être appliquée au développement d'appareils à ultrasons 3D de la génération actuelle et de la prochaine génération. Le rapport portera principalement sur la mise au point d'une structure évoluée de conformation de faisceaux afin de permettre l'utilisation de techniques de traitement d'ouverture synthétique et de traitement adaptatif de signal dans des appareils à ultrasons déployant des réseaux multidimensionnels de capteurs.

Le principal objectif consiste à développer une technologie de détection et d'imagerie ultrasoniques qui facilitera l'application de l'imagerie médicale non effractive à l'évaluation médicale et au traitement du personnel blessé des FC, des blessés au combat et des victimes secourues durant les opérations de recherche et de sauvetage. Les besoins en matière de procédures de diagnostic médical non effractives peuvent être satisfaits grâce à la mise au point de systèmes d'imagerie médicale à ultrasons 3D compacts, portatifs et utilisables sur place. Étant donné que l'imagerie revêt une importance critique dans l'établissement rapide d'un diagnostic et d'un traitement, les principaux fabricants d'équipement d'imagerie ont introduit des appareils de tomodesitométrie et d'imagerie par résonance magnétique (IRM) qui permettent de réaliser des interventions chirurgicales à l'aide de techniques d'imagerie directe avec effraction minimale. Cependant, ces techniques d'imagerie sont dispendieuses et nécessiteraient l'utilisation d'une salle de chirurgie complète. Contrairement aux appareils de tomodesitométrie et d'IRM, qui sont souvent installés dans des salles spécialisées conçues spécialement en fonction de leurs besoins, l'échographie est une méthode d'imagerie bien moins chère et plus souple qui peut être déployée dans des secteurs opérationnels éloignés et hostiles qui intéressent les FC. De plus, à l'inverse des tomodesitomètres ou des appareils d'IRM cliniques, les systèmes à ultrasons permettent au chirurgien ou au thérapeute de voir immédiatement ce qui se produit, en temps réel. Toutefois, même dans les systèmes d'imagerie médicale à ultrasons évolués, à la fine pointe, la résolution des images est faible en raison de la très petite taille des réseaux de capteurs déployés et des effets de distorsion causés par les caractéristiques de propagation non linéaires du corps humain. En résumé, la technologie d'imagerie à ultrasons existante ne peut pas être déployée sur place et ne permet pas de fournir des images de grande qualité.

Le développement d'une technologie d'échographie 4D (3D + temps) évoluée, présentée en détail dans le présent rapport, répond aux besoins en matière de haute capacité de résolution des images et de petite taille des réseaux pour des utilisations dans le domaine du diagnostic médical et dans des systèmes non destructeurs. La présente étude a reçu l'appui du Fonds d'investissement technologique de RDRC et de deux projets intitulés : MITTUG (traitement de tumeurs avec effraction minimale sous échoguidage 3D) et ADUMS (traitement adaptatif 4D pour système d'échographie médicale numérique) issus de la collaboration entre le Canada et l'Europe et financés par le Cinquième programme cadre IST de la Commission européenne.

En résumé, on prévoit que les résultats de notre étude sur la technologie d'échographie 4D serviront de fondement important à l'innovation dans le secteur industriel canadien des dispositifs à ultrasons en émergence, étant donné que les capacités d'imagerie à haute résolution prévues pourront être exploitées dans d'autres applications d'imagerie destinées au diagnostic médical et à des systèmes non destructeurs.

Table of contents

Abstract.....	i
Résumé	ii
Executive summary.....	iii
Sommaire	iv
Table of contents.....	v
List of figures.....	viii
List of tables.....	x
Acknowledgements.....	xi
1. Background.....	1
1.1 Current State-of-the-Art of 3D Ultrasound System Technology	1
1.1.1 Current Beamforming Structure of Ultrasound Systems	2
1.1.2 Current Technology Concept of 3D Visualization Methods for Ultrasound Systems	6
1.2 Next Generation Real-Time 3D Ultrasound System Technology.....	8
1.2.1 Synthetic Aperture Processing in the Beamforming Structure of Ultrasound Systems	8
1.2.2 Adaptive Beamforming Structure with Near-Instantaneous Convergence for Ultrasound Systems.....	10
1.2.3 Advanced Beamforming Structure for Line and Planar Arrays of Ultrasound Systems	11
2. Theoretical Remarks	14
2.1 Space-Time Processing.....	14
2.2 Definition of Basic Parameters	16
2.3 Detection and Estimation.....	17
2.4 Cramer-Rao Lower Bound (CRLB) Analysis.....	21
3. Optimum Estimators for Array Signal Processing.....	24
3.1 Generic Multi-Dimensional Conventional Beamforming Structure.....	25

3.1.1	Line-Array Conventional Beamformer	25
3.1.2	Circular Array Conventional Beamformer	29
3.2	Multidimensional (3-D) Array Conventional Beamformer	30
3.2.1	Decomposition Process for 2-D & 3-D Sensor Array Beamformers	30
3.3	Influence of the Medium's Propagation Characteristics on the Performance of a Receiving Array	35
3.4	Array Gain	38
4.	Advanced Beamformers.....	40
4.1	Synthetic Aperture Processing.....	40
4.2	Adaptive Beamformers.....	42
4.2.1	Minimum Variance Distortionless Response (MVDR).....	43
4.2.2	Generalized Sidelobe Canceller (GSC)	43
4.2.3	Steered Minimum Variance Broadband Adaptive (STMV)	45
5.	Implementation Considerations	50
5.1	Signal Cancellation Effects of the Adaptive Algorithms.....	51
5.2	Generic Multi-Dimensional Sub-Aperture Structure for Adaptive Schemes	53
5.2.1	Sub-Aperture Configuration for Line Arrays	54
5.2.2	Sub-Aperture Configuration for Circular Array	54
5.2.3	Sub-Aperture Configuration for Cylindrical Array	55
5.2.4	Sub-Aperture Configuration for Planar and Spherical Arrays.....	57
5.3	Signal Processing Flow of a 3-D Generic Sub-Aperture Structure	60
6.	Concept Demonstration: Simulations & Experimental Results.....	61
6.1	Computing Architecture	62
6.1.1	Experimental Platform.....	64
6.1.2	Algorithm Implementation	64
6.2	Details of a Real 3D Ultrasound System Deploying a Planar Array	69
6.2.1	Requirements	69
6.2.2	Signal Conditioning and Data Acquisition Unit	70
6.2.3	Bandwidth Requirements.....	73
6.3	Synthetic Data.....	77
6.3.1	Synthetic Data Results for Ultrasound Systems Deploying Line Arrays	77

6.3.2 Synthetic Data Results for Ultrasound Systems Deploying Planar
Arrays 84

6.3.3 Real Data Results for Ultrasound Systems Deploying Linear Arrays86

7.	Conclusion	89
8.	References.....	90
9.	List of symbols / abbreviations / acronyms / initialisms.....	95

List of figures

Figure 1. Typical beamformers for linear arrays of ultrasound systems. The shaded sub-apertures indicate the selected spatial locations for the formation of synthetic aperture according to ETAM algorithm.....	3
Figure 2. Tomography images of electronic chip obtained with different ultrasound systems. <u>Left</u> image represents output of a low-end ultra-sound system with a linear array of 96-sensor and 32-sensor beamformer with frequency range centered at 7-MHz with 6-MHz bandwidth. <u>Right</u> image was provided by high-end cardiac ultrasound system deploying a curvilinear 128-sensor array with 48-sensor beamformer with frequency range centered at 3.5-MHz with 3-MHz bandwidth.	4
Figure 3. Mechanical scanning of ultrasound probes for image acquisition of 2D B-scans to obtain 3D ultrasound images through volume rendering.....	7
Figure 4. Conventional 3D Beamforming structure for 2D planar array.....	12
Figure 5. A model of space-time signal processing. It shows that ultrasound signal processing is two dimensional in the sense that it involves both temporal and spatial spectral analysis. The temporal processing provides characteristics for target classification and the spatial processing provides estimates of the directional characteristics (bearing, range-depth) of detected echoes (active case) or signals of interest (passive case).....	15
Figure 6. Geometric configuration and coordinate system for a line array.....	26
Figure 7. Geometric configuration and coordinate system for a circular array of sensors.	29
Figure 8. Coordinate system and geometric representation of the concept of decomposing a cylindrical array beamformer. The $\mathbf{N} = NM$ sensor cylindrical array beamformer consists of N circular arrays with M being the number of sensors in each circular array. Then, the beamforming structure for cylindrical arrays is reduced into coherent sub-sets of circular (for $0^\circ - 360^\circ$ azimuth bearing estimates) and line array (for $0^\circ - 180^\circ$ angular elevation bearing estimates) beamformers.	33
Figure 9. Basic processing structure for the memoryless GSC.....	44
Figure 10. Realization of the steered covariance adaptive beamformer.	48
Figure 11. Concept of adaptive sub-aperture structure for line arrays. Schematic diagram shows the steps: (1) formation of J sub-apertures, (2) for each sub-aperture formation of S conventional beams, (3) for a given beam direction, θ formation of line arrays that consist of J number of directional sensors (beams).	53
Figure 12. Concept of adaptive sub-aperture structure for circular arrays, which is similar to that for line arrays shown in Figure 11.....	54

Figure 13. Geometric representation of the concept of adaptive sub-aperture structure for cylindrical arrays. In this example the number of sub-apertures was $G=3$. The $\mathbf{x} = NM$ sensor cylindrical array beamformer consists of N circular arrays with M being the number of sensors in each circular array. Then, the sub-aperture adaptive structure for cylindrical arrays is reduced to the steps of adaptive sub-aperture structures for circular and line arrays as defined in the schematics of Fig. 11 & 12.	58
Figure 14. Signal processing of generic structure decomposing the 3-D beamformer for cylindrical arrays of sensors into coherent sub-sets of line and circular array beamformers.	59
Figure 15. Special purpose ultrasound imaging system to assess image resolution improvements of the adaptive beamformers.....	61
Figure 16. <u>Left</u> picture shows the general purpose ultrasound system. <u>Right</u> picture shows the data acquisition system providing digitization of the RF data from the probe of the system at the left.	62
Figure 17. Volume 4D Digital Scanning for Ultrasound Applications using Radar & Sonar Phased Array Adaptive Beamforming of DRDC Toronto real 3D ultrasound system development.....	70
Figure 18. Structure of the PC-based computing architecture development for the real 3D ultrasound system development.....	72
Figure 19. Beam pattern resulting from Case I.....	78
Figure 20. Reconstructed Images resulting from Case 1	80
Figure 21: Reconstructed Images resulting from Case II.....	80
Figure 22. Beam pattern resulting from Case II.....	81
Figure 23. Beam pattern resulting from Case III.	82
Figure 24. Images resulting from Case III.	83
Figure 25. Images resulting from Case IV.....	83
Figure 26. C-scans derived from the 3D reconstructed images of the simulated spherical shell, <u>Left image</u> , reconstructed with the 3D conventional beamformer. <u>Right image</u> , reconstructed with the 3D adaptive beamformer.....	85
Figure 27. 3D volume reconstruction of the simulated spherical shell, <u>Left image</u> , reconstructed with the 3D conventional beamformer. <u>Right image</u> , reconstructed with the 3D adaptive beamformer.	85
Figure 28. Results with wire phantom.	87
Figure 29. Results with Ball Phantom.	88

List of tables

Table 1. Cluster node configuration.....	64
Table 2: Parameters for Cases I, II and III.	77
Table 3: Parameters for Case IV.	78

Acknowledgements

The authors wish to express their appreciation to the DRDC Technology Investment Fund and the European Commission IST Funding Agency for providing financial support for the investigation discussed in the present report.

This page intentionally left blank.

1. Background

In general, the mainstream conventional signal processing of ultrasound systems consists of a selection of temporal and spatial processing algorithms [1,60]. These algorithms are designed to increase the signal-to-noise ratio for improved signal detectability while simultaneously providing parameter estimates such as Doppler and bearing for incorporation into the image reconstruction process. Their implementation in real time systems had been directed at providing high-quality, artifact-free conventional beamformers, currently used in operational ultrasound. However, aberration effects associated with ultrasound system applications suggest that fundamentally new concepts need to be introduced into the signal processing structure of next-generation ultrasound.

To provide a context for the material contained in this report, it would seem appropriate to review briefly the beamforming functionality of a conventional 3D ultrasound system and to contrast this functionality with the basic requirements of high-performance 3D systems deploying multi-dimensional arrays of sensors.

1.1 Current State-of-the-Art of 3D Ultrasound System Technology

The requirements for non-invasive and minimally invasive medical diagnostic procedures can be addressed with the development of high-resolution 3D ultrasound medical imaging systems. However, even the most-advanced state-of-the-art medical ultrasound imaging systems suffer from very poor image resolution, which is the result of the very small size of deployed arrays of sensors and the distortion effects caused by the human-body's non-linear propagation characteristics. In particular, some of the limitations (e.g. resolution) of ultrasound imaging are related to fundamental physical aspects of the ultrasound transducer and the interaction of ultrasound with tissues (e.g. aberration effects). In addition to fundamental limitations are limitations related to the display of the ultrasound image in an efficient manner allowing the physician to extract relevant information accurately and reproducibly. Specifically, in this report we will address the following limitations:

- Conventional ultrasound images are 2D, hence, the physician must mentally integrate multiple images to develop a 3D impression of the anatomy/pathology during procedure. This practice is time-consuming, inefficient, and requires a highly skilled operator, all of which can potentially lead to incorrect diagnostic and therapeutic decisions.
- Often the physician requires accurate estimation of tumour and organ volume. The variability in ultrasound imaging and volume measurements using a conventional 2D technique is high, because current ultrasound volume measurement techniques assume an idealized elliptical shape and use only simple measures of the width in two views [64]. 3D images will provide means to obtain accurate and precise organ and tumor volume estimates [65].

- It is difficult to localize the thin 2D ultrasound image plane in the organ, and difficult to reproduce a particular image location at a later time, making 2D ultrasound a limited imaging modality for monitoring of disease progression/regression and follow-up patient studies.

In summary, on issues of 3D visualization, we propose to overcome these limitations by combining the proposed advanced 3D beamforming structure defined in the present report with existing 3D visualization display technologies [60, 63-68]. To contrast, however, the proposed 3D ultra-sound technology development, it is essential to review the current state-of-the-art of ultrasound technology on 3D visualization and beamforming processing.

1.1.1 Current Beamforming Structure of Ultrasound Systems

A state-of-the-art transducer array of an operational ultra-sound system is either linear or curvilinear depending on the application; and for each deployed array, the number of transducers is in the range of 96 to 256 elements. However, only a small number of transducers of a given array are beamformed coherently to reconstruct a tomography image of interest.

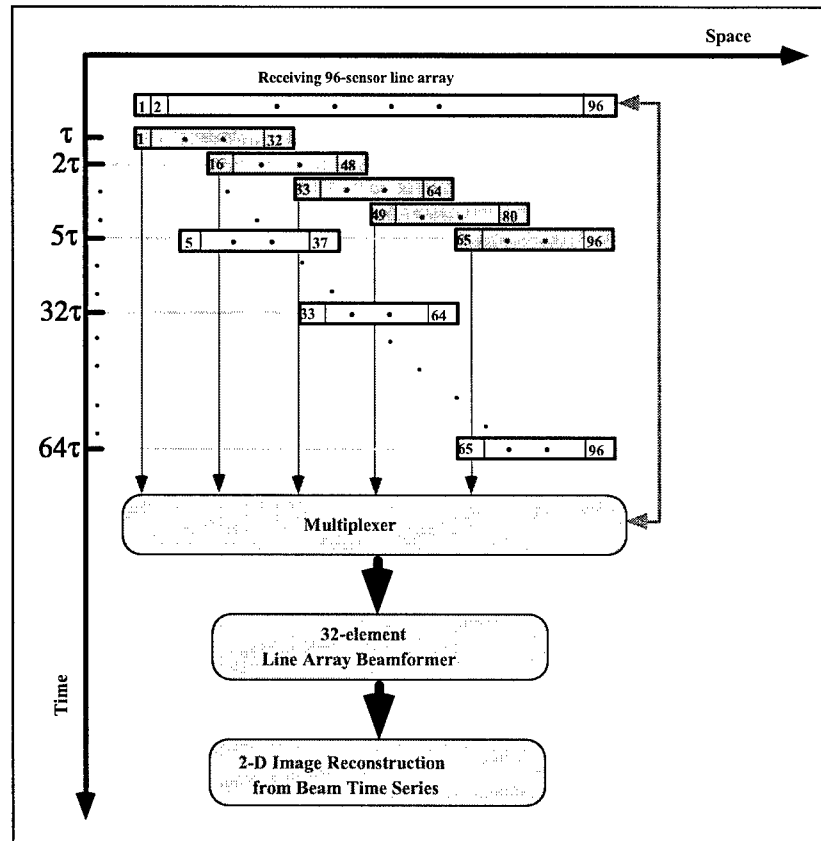


Figure 1. Typical beamformers for linear arrays of ultrasound systems. The shaded sub-apertures indicate the selected spatial locations for the formation of synthetic aperture according to ETAM algorithm.

A typical number of transducers that may be included in the beamforming structure of an ultrasound system is in the range of 32 to 128 elements. Thus, the system array gain may be smaller by approximately $10 \times \log_{10}(3) \approx 5$ dBs than that available by the deployed array. Figure 1 illustrates the basic processing steps associated with the ultrasound beamforming process. For the sake of simplicity and without any loss of generality, the array in Figure 1 is considered to be linear with 96-elements that can be used to transmit and receive the radiated ultrasound field. As shown in Figure 1, for each active transmission, the ultrasound beamformer processes coherently the received signal of 32-elements only, which is a sub-aperture of the 96-element deployed array. The active transmission takes place approximately every $\tau = 0.3\text{ms}$, depending on the desired penetration depth in the body. The beam steering process is at the broadside.

When an active transmission is completed, the receiving 32-element sub-aperture is shifted to the right, as shown in Figure 1. Thus, to make use of all the 96-elements of the deployed array, the 32-element beamforming process

is repeated 64 times, generating 64 broadside beams. In other words, it takes approximately $64 \times 0.3 \text{ ms} \approx 20 \text{ ms}$ to reconstruct a 2-D tomography image of interest. As a result, the resolution characteristics of the reconstructed image are defined by the array gain of the beamformer and the temporal sampling of the beam or element time series, for analog or digital beamformers, respectively. In the specific case of Figure 1, the pixel resolution along the horizontal x-axis of a reconstructed tomography image is defined by the angular resolution along azimuth of the 32-element beamformer. This resolution is usually being improved by means of interpolation, which defines the basic difference between beamformers of different ultrasound systems.

The pixel resolution along the vertical y-axis of the reconstructed image is defined by the sampling rate, which is always very high and it is not a major concern in ultrasound system applications. Thus, improvements of image resolution in ultrasound system applications requires mainly higher angular resolution or very narrow beamwidth, which means longer arrays and longer sub-apertures for the beamforming process with consequent technical and operational implications and higher system manufacturing cost.

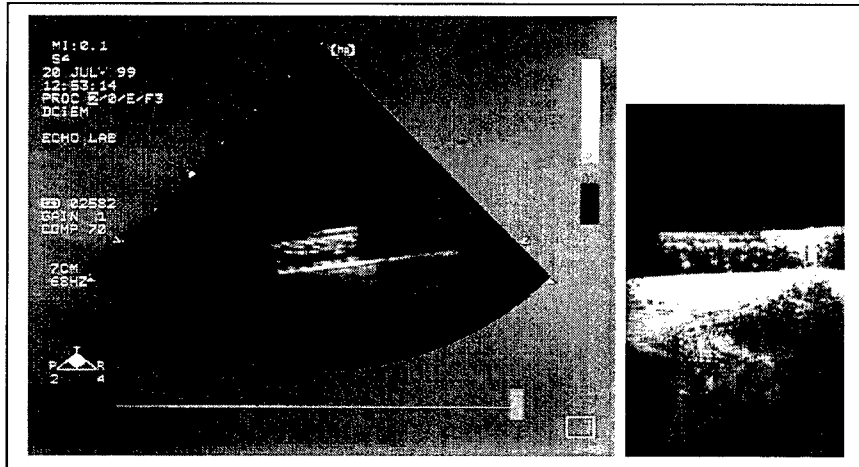


Figure 2. Tomography images of electronic chip obtained with different ultrasound systems. Left image represents output of a low-end ultra-sound system with a linear array of 96-sensor and 32-sensor beamformer with frequency range centered at 7-MHz with 6-MHz bandwidth. Right image was provided by high-end cardiac ultrasound system deploying a curvilinear 128-sensor array with 48-sensor beamformer with frequency range centered at 3.5-MHz with 3-MHz bandwidth.

To emphasize the limitations of the current ultrasound technology, Figure 2 provides two tomography images of an electronic chip that have been obtained with two different ultrasound systems. The image at the left of Figure 2 represents the output of a low-cost ultra-sound system with a linear array of 96 elements and with a 32 element beamformer at a frequency range centered at 7 MHz with 6 MHz bandwidth. The cost of this system was \$30,000. The image at the right of Figure 2 was provided by a high-end cardiac ultrasound system deploying a curvilinear 128-element array with a 48-element beamformer at a frequency range centered at 3.5 MHz with 3

MHz bandwidth. The cost of this system was \$280,000. Since the beamforming characteristics for both these two ultrasound systems are similar, the resolution characteristics of the reconstructed images of Figure 2 are very similar, as expected.

The main advantages of this simplified beamforming structure are the following:

The generation of broadside beams allows the use of frequency regimes that are higher than the corresponding spatial-aliasing frequency of the sensor spacing of the ultrasound probe. This is because side-lobe artifacts due to spatial aliasing are insignificant for beams with broadside beamsteering. For example, the probe that was used to generate the left image in Figure 2 with 7-MHz center frequency had 0.35mm sensor spacing that corresponds to 2.2 MHz design frequency for phased array processing to avoid spatial aliasing artifacts.

The advantage (suppression of spatial-aliasing artifacts) provided by the broadside beam-steering process has been used effectively by illumination techniques using higher order-harmonics to achieve deeper penetration with corresponding higher image resolution along the temporal axis.

The field of view of the probe may be larger than the aperture size required by the broadside beamformer. This approach minimizes the hardware complexity of the analog-to-digital converter (A/D) by using a multiplexer to control the data acquisition process of a probe with a larger number of sensors than those being used by the broadside focus beamformer.

Until recently, the above innovative approaches have served well the ultrasound system requirements by providing practical alternatives to technical problems that were due mainly to limitations in the maximum number of channels deployed by A/D units and the limited capabilities of computing architectures. Presently, these type of technology limitations do not exist. Thus, new technology development options have become available to exploit the vast experience from phased array beamformers that have been advanced by the sonar and radar research communities.

In fact, the introduction of linear phased array probes for cardiac applications is the first successful step toward this direction.

The use, however, of linear arrays introduces another major problem in terms of false targets, a problem that has been identified by both the ultrasound and sonar researchers using towed sonar arrays [60]. In particular, a linear array provides angular resolution within the tomography plane (B-scan) that the beam steering is formed. The angular resolution, however, of the beam steering vectors of linear arrays is omnidirectional in the plane perpendicular to the B-scan plane. Thus, reflections from surrounding organs cannot be spatially resolved by the steered beams of a line array; and they appear as

false targets in towed array sonars, or false components of a reconstructed image by a linear ultrasound probe.

To address the problem of false components in the reconstructed image, the 1.5D and 1.75D ultrasound array probes have been introduced that consist of linear arrays stacked as partially planar arrays. In particular, the GE 1.75D ultrasound array probe consists of 8 linear arrays with 128-sensors each and with 0.2mm sensor spacing. The linear array spacing is 1.5mm. Moreover, the 1.5D array probes consist of 4 linear arrays with 128-sensors each.

Thus, the steered beams for both the 1.5D and 1.75D type of array probes are 3-dimensional (3D) and have the property to resolve the angular components of ultrasound reflected signals along azimuth and elevation. Although the 3D beams of 1.75D arrays may be viewed as the first step for 3D ultrasound imaging, they do not have sufficient angular resolution capabilities along elevation to generate 3D ultrasound volumes. The proposed 3D beamforming structure and the relevant 3D ultrasound system development based on a (32x32) planar array probe attempt to address the above limitations and the results are discussed in the present report. However, at this point, it is considered appropriate to briefly review the current state of the art in 3D ultrasound technology.

1.1.2 Current Technology Concept of 3D Visualization Methods for Ultrasound Systems

Current 3D Ultrasound imaging systems have 3 components: image acquisition, reconstruction of the 3D image, and display [66,67]. The first component is crucial in ensuring that optimal image quality is achieved. In producing a 3D image, the conventional transducer is moved over the anatomy while 2D images are digitized and stored in a microcomputer, as shown in Figure 3. To reconstruct the 3D geometry without geometric distortion, the relative position and angulation of the acquired 2D images must be known accurately. Over the past 6 years there have been numerous developments and evaluating techniques for obtaining 3D ultrasound images using two approaches: mechanical scanning and freehand scanning [65,66,68-71].

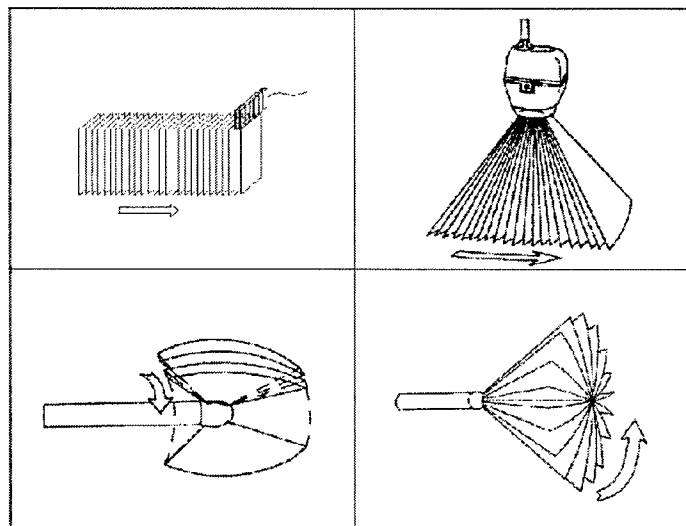


Figure 3. Mechanical scanning of ultrasound probes for image acquisition of 2D B-scans to obtain 3D ultrasound images through volume rendering.

Mechanical Scanning: Based on earlier work, Fraunhofer (National Research Center, Darmstadt, Germany) and the Robarts Research Institute (RRI of the University of Western Ontario, London Canada), have developed systems in which the ultrasound transducer is mounted in a special assembly, which can be driven by a motor to move in a linear fashion over the skin or tilted in equal angular steps. The movement can be continuous, or intermittent at cardiac and/or respiratory intervals [65,70]. In addition, the spatial-sampling frequency of the image acquisition can be adjusted based on the elevational resolution of the transducer and the depth of the region-of-interest. For linear scanning, they collect 140 images (336 x 352 pixels each) at 0.5 mm intervals in a time that depends on the ultrasound machine frame rate and whether cardiac gating is used. All scanning parameters can be adjusted depending on the experiment and type of acquisition. For example for 3D B-mode - they typically use 2 or 3 focal zones resulting in about 15 frames/sec and a total 3-D scanning time of 9 sec for 140 images.

Freehand Scanning: Although the mechanical scanning approach produces accurate 3D ultrasound images, the mechanical assembly is bulky and not convenient for the operator. In addition, the mechanical constraint does not permit its use in imaging larger structures such as the liver or fetus. Thus, alternative techniques have been introduced that maintain the flexibility of the 2D exams yet produce 3D images. These techniques include freehand scanning systems, in which a magnetic positioning and orientation measurement (POM) device is mounted on the transducer [63,68,71-73]. To produce a 3D image, the operator manually moves the hand-held transducer, while the POM device transfers the position and orientation coordinates of

the transducer to a microcomputer. At the same time, 2D images are digitized by the same computer and associated with the appropriate coordinates. After the necessary number of 2D images are acquired (typically 60 - 160), the computer reconstructs the 3D image. Care is taken to scan the patient sufficiently slowly so that the region of interest is scanned with no gaps. Typically, the scan lasts 4 - 11 sec. while the patient holds its breath. Although this technique does produce useful images, it still suffers from major limitations that precludes its use for general diagnostic procedures.

Most importantly, the manual scanning of the 3D space with a linear array does not eliminate the false components of the reconstructed B-scan images that were discussed in the previous section.

1.2 Next Generation Real-Time 3D Ultrasound System Technology

As part of our DRDC's Technology Investment Fund (TIF) project objectives, the development of an ultrasound imaging technology leading to a next-generation high-resolution real 3D diagnostic imaging system has been initiated. The proposed technology includes:

- Synthetic aperture processing to sample large size 2D arrays for 3D phased array beamforming,
- adaptive beamforming to effectively increase the angular resolution
- 32x32-sensor phased planar arrays with uniform 0.4mm sensor spacing to achieve maximum sensitivity.
- Integration of Fraunhofer's 3D and 4D visualization schemes with the image reconstruction process of the 3D ultrasound beamformer.

As stated above, the long term objective of the present development is to replace the existing beamformers of ultrasound systems with an adaptive beamforming structure in order to maximize the array gain and image resolution capabilities of 2D and 3D ultrasound systems.

1.2.1 Synthetic Aperture Processing in the Beamforming Structure of Ultrasound Systems

At this point it is important to review a few fundamental physical arguments associated with synthetic aperture processing for sonar and ultrasound systems. In the past [13] there was a conventional wisdom regarding synthetic aperture techniques, which held that practical limitations prevent them from being applicable to real-world systems. The issues were threefold.

1. Since passive synthetic aperture can be viewed as a scheme that converts temporal gain to spatial gain, most signals of interest do not have sufficient temporal coherence to allow a long spatially coherent aperture to be synthesized.
2. Since past algorithms required *a priori* knowledge of the source frequency in order to compute the phase correction factor [13], the method was essentially useless in any bearing estimation problem since Doppler would introduce an unknown bias on the frequency observed at the receiver.
3. Since synthetic aperture processing essentially converts temporal gain to spatial gain, there was no "new" gain to be achieved, and therefore, no point to the method.

Recent work [12,13,60] has shown that there can be realistic conditions in sonar applications under which all of these objections are either not relevant or do not constitute serious impediments to practical applications of synthetic aperture processing in operational systems [30]. Theoretical discussions have shown [13] that the above three arguments are valid for cases that include the formation of synthetic aperture by a single sensor and in mediums with isotropic noise characteristic. However, when the noise characteristics of the received signal are non-isotropic and the receiving array includes more than one sensor, then there is spatial gain available from passive synthetic aperture processing and this has been discussed analytically in [1,13,60]. Since the medium propagation characteristics of sonar and ultrasound system application are very similar and non-isotropic, synthetic aperture techniques that are successful in sonar systems can be successful in ultrasound applications as well. Furthermore, formation of a synthetic aperture in sonar systems requires the movement of the receiving line array. In ultrasound systems, however, the formation of a synthetic aperture can be derived from the sub-aperture measurements of a longer receiving array, as shown in Figure 1, which eliminates the phase errors associated with the movement of the receiving array.

A summary of these research efforts has been reported in a special issue in the IEEE J. Oceanic Eng. [13]. The synthetic aperture processing scheme that has been used in broadband sonar applications [1,60] is based on the Extended Towed Array Measurements (ETAM) algorithm, [12,30]. The basic concept of this algorithm is a phase-correction factor that is used to combine coherently successive measurements of a moving receiving line array to extend the effective array length.

The dark shaded sub-apertures in Figure 1 show the proposed experimental implementation of the ETAM algorithm for ultrasound applications in terms of the sub-aperture line array size and sensor positions as a function of time and space. Between two successive positions of the 32-sensor sub-aperture there are a number of sensor pairs of space samples of the acoustic field that

have the same spatial information, their difference being a phase factor [1,12,13,60] related to the time delay these measurements were taken. The optimum overlap size, which is related to the variance of the phase correction estimates, has been shown [13] to be equal to the half size of the deployed sub-aperture. For the particular example of Figure 1, the spatial overlap size will be 16-sensors. Thus, by cross-correlating the 16-sensor pairs of the sensor time series that overlap, the desired phase correction factor is derived, which compensates for the time delay between these measurements and the phase fluctuations caused by the variability and non-isotropic propagation characteristics of the human body; this is called the *overlap correlator*. Following the above, the key parameters in the ETAM algorithm is the time increment τ between two successive sets of measurements. This may be the interval of 0.3ms between two active ultrasound transmissions. Then, the total number of sets of measurements required by the 32-sensor sub-aperture to achieve an extended aperture size equal to the deployed array (i.e. 96-sensor array) is five.

The performance characteristics and expectations from the ETAM algorithm have been evaluated experimentally for sonar applications and the related results have been reported [12,13,30].

Thus, if we consider the ultrasound system in Figure 1, the proposed synthetic aperture processing will coherently synthesize the spatial measurements derived from the 32-element sub-apertures of the ultrasound receiving array into a longer aperture equivalent to the 96-sensor deployed array using only 5 sub-aperture measurements instead of 64. In this way, the required hardware modifications of an ultrasound system will be minimized since the A/DC will remain the same. Moreover, the time required to reconstruct a tomography image will be reduced from the current 20ms time interval to $5 \times 0.3 \text{ ms} \approx 1.5 \text{ ms}$. In parallel to this improvement, there will be an increase in the array gain and the angular resolution of the ultrasound beamforming structure by 5dBs.

1.2.2 Adaptive Beamforming Structure with Near-Instantaneous Convergence for Ultrasound Systems

The adaptive processing schemes proposed in this investigation are characterised as Dual-Use technologies and have been tested in operational active sonars [60,61]. Real data results have shown that they provide array gain improvements for signals embedded in anisotropic noise fields, similar to those in the human body.

Despite the geometric differences between the line and planar arrays, the underlying beamforming processes for these arrays are time delay beamforming estimators, which are basically spatial filters. However, optimum beamforming requires the beamforming filter coefficients to be chosen based on the covariance matrix of the received data by the N -sensor

array in order to optimize the array response [60,61]. The family of algorithms for optimum beamforming that use the characteristics of the noise, are called *Adaptive Beamformers* [1,60]. In this investigation we consider the implementation in ultrasound systems for various partially adaptive variants of the Linear Constraint Minimum Variance (LCMV) method and a Generalized Sidelobe Canceller (GSC) adaptive beamformer [60,61] that have been tested successfully in real time active-passive sonar applications. Thus, the implementation of adaptive schemes in ultrasound systems will not be restricted into one method. In fact, the generic concept of the sub-aperture multi-dimensional array to be considered in this investigation would allow for the implementation of a wide variety of adaptive schemes in ultrasound systems [62]. As for the implementation of adaptive processing schemes in active systems, the following issues need to be addressed.

For ultrasound applications that include matched filter processing for Doppler shift estimates, the outputs of the adaptive algorithms are required to provide coherent beam time series to facilitate the post-processing. This means that these algorithms should exhibit near-instantaneous convergence and provide continuous beam time series that have sufficient temporal coherence to correlate with the reference replica in matched filter processing [1,60].

1.2.3 Advanced Beamforming Structure for Line and Planar Arrays of Ultrasound Systems

As discussed in the previous section (1.1.1), deployment of planar arrays in ultrasound medical imaging systems has been gaining increasing popularity because of its advantage to provide real 3-D images of organs under medical examination. However, operational ultrasound systems deploying planar arrays are not yet available. Moreover, if we consider that a state-of-the-art phased array line array ultrasound system consists of 128 sensors, then a planar array ultrasound system should include at least $128 \times 128 = 16,384$ sensors in order to achieve the angular resolution performance of a line array system and the additional 3D image reconstruction capability provided by the elevation beam steering of a planar array. Thus, increased angular resolution in azimuth and elevation beam steering for ultrasound systems means larger sensor arrays, with consequent technical and higher cost implications. As it will be shown in this report, the alternative is to implement synthetic aperture and adaptive beam processing in ultrasound systems that deploy a planar array with 1024 (64×16 or 32×32) sensors, which consist of 32 line arrays with 32 sensors each. Then, the anticipated array gain improvements by the adaptive beamformer would be equivalent to those provided by a 96-sensor line array for azimuth beam-steering and a 96-sensor vertical line array for elevation beam steering for real 3D ultrasound imaging. In summary, the array gain improvements for an adaptive 1024-sensor planar array will be equivalent to those that could be provided by a conventional $96 \times 96 = 9216$ -sensor planar array. This is because for line arrays, our preliminary

quantitative assessment shows that the image resolution improvements of the proposed advanced beamformers, will be equivalent to a three-time longer physical aperture.

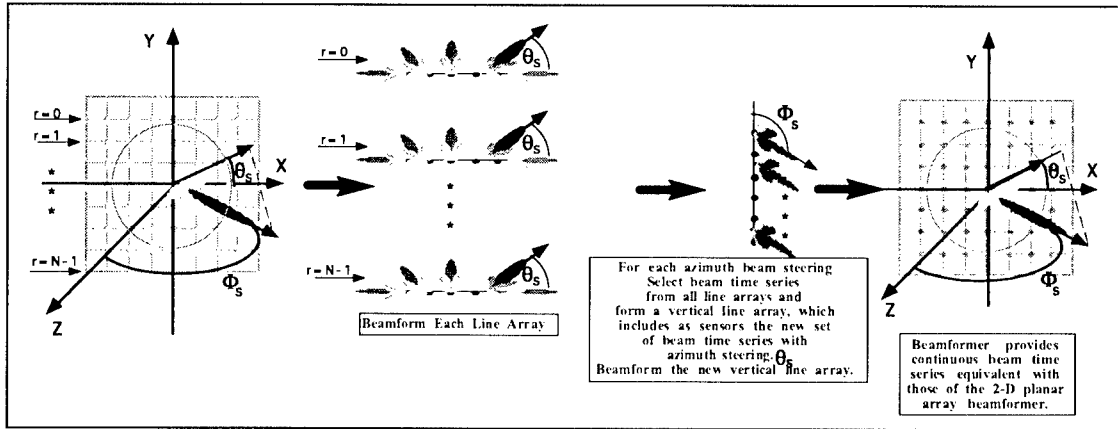


Figure 4. Conventional 3D Beamforming structure for 2D planar array.

To address this requirement and to allow for a flexible system design for line and or planar array ultrasound systems, the present investigation attempts to develop an advanced beamforming structure applicable to both line and planar arrays. The proposed approach is conceptually similar to previous investigations [7,26,61] carried out for sonar system applications by the authors of this report.

Briefly, these previous studies have shown that a planar array beamformer can be decomposed into two line array beamforming steps. For example, let us consider the discrete planar array in Figure 4, with \aleph sensors where $\aleph = NM$ and M, N are the number of sensors along x-axis and y-axis, respectively. The first step includes an M -sensor line-array beamforming along the x-axis of the planar array providing beam time series with azimuth beam steering. The line array beamformer will be repeated N -times to get the vector that includes the beam times series $\bar{B}_y(f, \theta_s)$, where the index $y = 0, 1, \dots, N-1$ is along the axis y . For a given azimuth beam steering, the second step includes line array beamforming along y-axis by treating the vector $\bar{B}_y(f, \theta_s)$ as the input signal for the line array beamformer to get the output $B(f, \theta_s, \phi_s)$, which is the output of a planar array beamformer for a given azimuth θ_s and elevation beamsteering ϕ_s , respectively.

Figure 4 shows the involved steps of decomposing the 2-D planar array beamformer into two steps of line-array beamformers. The decomposition of the planar array beamformer into these two line-array beamforming steps leads to an efficient implementation based on the following two factors.

First, the number of the involved sensors for each of these line array beamformers is much less than the total number of sensors, N of the planar array. This type of decomposition process for the 2-D beamformer eliminates the need for very large memory and CPU's with very high throughput requirements in one board for real time system applications. Secondly, all these line array beamformers can be executed in parallel, which allows their implementation in much simpler parallel architectures with simpler CPU's, which is a practical requirement for real time system application. Besides the advantage of the efficient implementation, the proposed decomposition approach makes the application of the spatial window much simpler to be incorporated. Furthermore, both the synthetic aperture and adaptive processing schemes of Sections 2.3.1 and 2.3.2 that will be developed for line arrays, will be directly applicable to planar arrays through the proposed decomposition of the planar array beamforming process into two line array beamforming steps.

2. Theoretical Remarks

Active ultrasound operations involve the transmission of well defined ultrasound signals, called replicas, which illuminate the human body medium. The reflected ultrasound energy from an extended target or body organ provides the array receiver with a basis for detection and estimation. The image reconstruction process is a passive ultrasound beamforming operation.

All the above active-passive beamforming issues have been discussed in several review articles [1-6] that form a good basis for interested readers to become familiar with “main stream” beamforming signal processing developments. Therefore, discussions of issues of conventional signal processing, detection, estimation and influence of medium on ultrasound system performance are beyond the scope of this report. Only a very brief overview of the above issues will be highlighted in this section in order to define the basic terminology required for the presentation of the main theme of the present article. Let us start with a basic system model that reflects the interrelationships between the extended target or the human body (medium) and the receiving sensor array of an ultrasound system.

A schematic diagram of this basic system is shown in Figure 5, where array signal processing is shown to be two-dimensional [1,5,10,12,18] in the sense that it involves both temporal and spatial spectral analysis. The temporal processing provides spectral characteristics that are used for classification and the spatial processing provides estimates of the directional characteristics, (i.e. bearing and depth), of a detected signal. Thus, *Space-Time Processing* is the fundamental processing concept in ultrasound systems and it will be the subject of our discussion in the next section.

2.1 Space-Time Processing

For geometrical simplicity and without any loss of generality, we consider here a combination of N equally spaced sensors in a linear array, which may form a phased array system that can be used to estimate the directional properties of echoes and acoustic signals. As shown in Fig. 5, a direct analogy between sampling in space and sampling in time is a natural extension of the sampling theory in space-time signal representation and this type of space-time sampling is the basis in array design that provides a description of an array system response. When the sensors are arbitrarily distributed, each element will have an added degree of freedom, which is its position along the axis of the array.

This is analogous to non-uniform temporal sampling of a signal. In this report we extend our discussion to multi-dimensional array systems.

Sources of sound that are of interest in ultrasound system applications provide harmonic narrowband and broadband signals that satisfy the wave equation [2,10]. Furthermore, their solutions have the property that their associated temporal-spatial characteristics are separable [10]. Therefore, measurements of the pressure field $z(\vec{r}, t)$ which is excited by acoustic source signals, provide the spatial-temporal output response, designated by $x(\vec{r}, t)$

of the measurement system. The vector \vec{r} refers to the source-sensor relative position and t is the time.

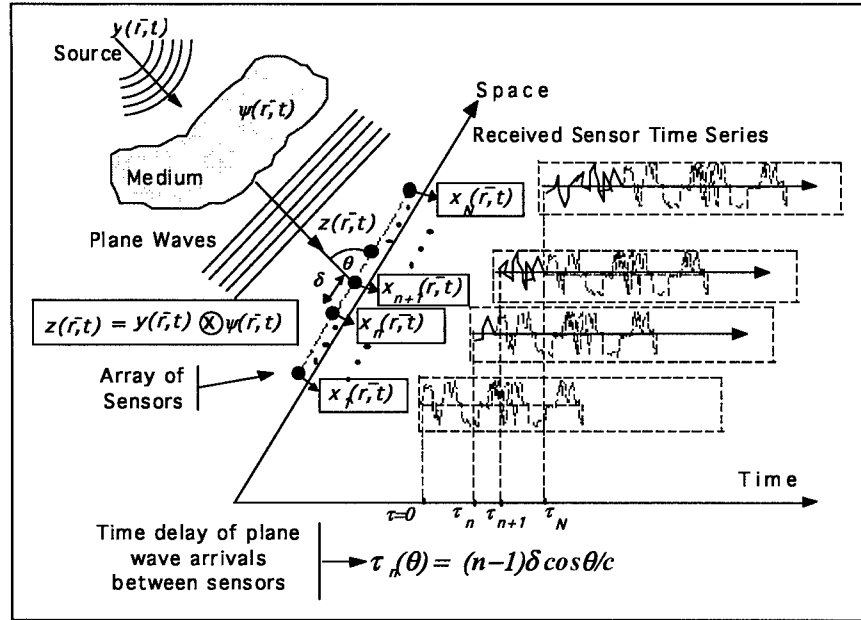


Figure 5. A model of space-time signal processing. It shows that ultrasound signal processing is two dimensional in the sense that it involves both temporal and spatial spectral analysis. The temporal processing provides characteristics for target classification and the spatial processing provides estimates of the directional characteristics (bearing, range-depth) of detected echoes (active case) or signals of interest (passive case).

The output response $x(\vec{r}, t)$ is the convolution of $z(\vec{r}, t)$ with the line array system response $h(\vec{r}, t)$ [10,30]

$$x(\vec{r}, t) = z(\vec{r}, t) \otimes h(\vec{r}, t) \quad (4)$$

where \otimes refers to convolution. Since $z(\vec{r}, t)$ is defined at the input of the receiver, it is the convolution of the source's characteristics $y(\vec{r}, t)$ with the underwater medium's response $\psi(\vec{r}, t)$,

$$z(\vec{r}, t) = y(\vec{r}, t) \otimes \psi(\vec{r}, t) \quad (5)$$

Fourier transformation of Equation (3) provides:

$$X(\omega, \vec{k}) = \{Y(\omega, \vec{k}) \cdot \Psi(\omega, \vec{k})\} H(\omega, \vec{k}) \quad (6)$$

where, ω, \bar{k} are the frequency and wavenumber parameters of the temporal and spatial spectrums of the transform functions in Equations (4) & (5). Signal processing, in terms of beamforming operations, of the receiver's output $x(\bar{r}, t)$, provides estimates of the source bearing and possibly of the source range. This is a well-understood concept of the forward problem, which is concerned with determining the parameters of the received signal $x(\bar{r}, t)$ given that we have information about the other two functions $z(\bar{r}, t)$ and $h(\bar{r}, t)$ [5]. The inverse problem is concerned with determining the parameters of the impulse response of the medium $\psi(\bar{r}, t)$ by extracting information from the received signal $x(\bar{r}, t)$ assuming that the function $h(\bar{r}, t)$ is known [5]. The ultrasound problems, however, are quite complex and include both forward and inverse problem operations. In particular, detection, estimation and tracking-localization processes of ultrasound systems are typical examples of the forward problem, while target classification for passive-active diagnostic ultrasound imaging are typical examples of the inverse problem. In general, the inverse problem is a computationally very costly operation and typical examples in acoustic signal processing are seismic deconvolution and acoustic tomography.

2.2 Definition of Basic Parameters

This section outlines the context in which the ultrasound problem can be viewed in terms of simple models of acoustic signals and noise fields. The signal processing concepts that are discussed in this report have been included in sonar and radar investigations with sensor arrays having circular, planar, cylindrical and spherical geometric configurations [7,25,26,28]. Thus, we consider a multi-dimensional array of equally spaced sensors with spacing δ . The output of the n th sensor is a time series denoted by $x_n(t_i)$, where $(i=1, \dots, M_s)$ are the time samples for each sensor time series. * denotes complex conjugate transposition so that $\bar{\mathbf{X}}^*$ is the row vector of the received \mathbf{N} - sensor time series $\{x_n(t_i), n=1, 2, \dots, \mathbf{N}\}$.

Then $x_n(t_i) = s_n(t_i) + \varepsilon_n(t_i)$, where $s_n(t_i)$, $\varepsilon_n(t_i)$ are the signal and noise components in the received sensor time series. $\bar{\mathbf{S}}$, $\bar{\mathbf{\varepsilon}}$ denote the column vectors of the signal and noise components of the vector $\bar{\mathbf{X}}$ of the sensor outputs (i.e. $\bar{\mathbf{X}} = \bar{\mathbf{S}} + \bar{\mathbf{\varepsilon}}$).

$X_n(f) = \sum_{i=1}^{M_s} x_n(t_i) \exp(-j2\pi f t_i)$ is the Fourier transform of $x_n(t_i)$ at the signal with frequency f , $c = f\lambda$ is the speed of sound in the underwater, or human-body medium and λ is the wavelength of the frequency f . $\mathbf{S} = E\{\bar{\mathbf{S}} \bar{\mathbf{S}}^*\}$ is the spatial correlation matrix of the signal vector $\bar{\mathbf{S}}$, whose n th element is expressed by,

$$s_n(t_i) = s_n[t_i + \tau_n(\theta, \phi)] \quad (7)$$

$E\{\dots\}$ denotes expectation and $\tau_n(\theta, \phi)$ is the time delay between the $(n-1)^{\text{st}}$ and the n^{th} sensor of the array for an incoming plane wave with direction of propagation of azimuth

angle θ and an elevation angle ϕ , as depicted in Figure 3. In the frequency domain, the spatial correlation matrix \mathbf{S} for the plane wave signal $s_n(t_i)$ is defined by:

$$\mathbf{S}(f_i, \theta, \phi) = A_s(f_i) \overline{\mathbf{D}}(f_i, \theta, \phi) \overline{\mathbf{D}}^*(f_i, \theta, \phi), \quad (8)$$

where $A_s(f_i)$ is the power spectral density of $s(t_i)$ for the i^{th} frequency bin; and $\overline{\mathbf{D}}(f, \theta, \phi)$ is the steering vector with the n^{th} term being denoted by $d_n(f, \theta, \phi)$. Then matrix $\mathbf{S}(f_i, \theta, \phi)$ has as its n^{th} row and m^{th} column defined by, $S_{nm}(f_i, \theta, \phi) = A_s(f_i) d_n(f_i, \theta, \phi) d_m^*(f_i, \theta, \phi)$. Moreover, $\mathbf{R}(f_i)$ is the spatial correlation matrix of received sensor time series with elements, $R_{nm}(f, d_{nm})$. $\mathbf{R}_\epsilon'(f_i) = \sigma_n^2(f_i) \mathbf{R}_\epsilon(f_i)$ is the spatial correlation matrix of the noise for the i^{th} frequency bin with $\sigma_n^2(f_i)$ being the power spectral density of the noise, $\epsilon_n(t_i)$. In what is considered as an estimation procedure in this report, the associated problem of detection is defined in the classical sense as a hypothesis test that provides a detection probability and a probability of false alarm [31-33]. This choice of definition is based on the standard CFAR (constant false alarm rate) processor, which is based on the Neyman-Pearson criterion [31]. The CFAR processor provides an estimate of the ambient noise or clutter level so that the threshold can be varied dynamically to stabilize the false alarm rate. Ambient noise estimates for the CFAR processor are provided mainly by noise normalization techniques [34] that account for the slowly varying changes in the background noise or clutter. The above estimates of the ambient noise are based upon the average value of the received signal, the desired probability of detection and probability of false alarms.

At this point, a brief discussion on the fundamentals of detection and estimation process is required in order to address implementation issues of signal processing schemes in ultrasound systems.

2.3 Detection and Estimation

In passive systems, in general, we do not have the *a priori* probabilities associated with the hypothesis H_1 that the signal is assumed present and the null hypothesis is H_0 that the received time series consists only of noise. As a result, costs can not be assigned to the possible outcomes of the experiment. In this case, the Neyman-Pearson (N-P) Criterion [31] is applied because it requires only a knowledge of the signal's and noise's probability density functions (*pdf*).

Let $x_{n=1}(t_i)$, ($i=1, \dots, M$) denote the received vector signal by a single sensor. Then for hypothesis H_1 , which assumes that the signal is present, we have:

$$H_1: x_{n=1}(t_i) = s_{n=1}(t_i) + \epsilon_{n=1}(t_i),$$

where $s_{n=I}(t_i)$ and $\varepsilon_{n=I}(t_i)$ are the signal and noise vector components in the received signal and $p_I(x)$ is the pdf of the received signal $x_{n=I}(t_i)$ given that H_I is true. Similarly, for hypothesis H_0 :

$$H_0: x_{n=I}(t_i) = \varepsilon_{n=I}(t_i)$$

and $p_0(x)$ is the pdf of the received signal given that H_0 is true. The N-P criterion requires maximization of probability of detection for a given probability of false alarm. So, there exists a non-negative number η such that if hypothesis H_I is chosen then

$$\lambda(x) = \frac{p_I(x)}{p_0(x)} \geq \eta \quad (9)$$

which is the likelihood ratio. By using the analytic expressions for $p_0(x)$ (the pdf for H_0) and $p_I(x)$ (the pdf for H_I) in Eq. (9) and by taking the $\ln [\lambda(x)]$, we have [31],

$$\lambda_\tau = \ln [\lambda(x)] = \overline{s}^* R_\varepsilon' \overline{x} \quad (10)$$

where, λ_τ is the log likelihood ratio and R_ε' is the covariance matrix of the noise vector, as defined in the previous section 2.2. For the case of white noise with $R_\varepsilon' = \sigma_n^2 I$ and I the unit matrix, the test statistic in expression (10) is simplified into a simple correlation receiver (or replica correlator)

$$\lambda_\tau = \overline{s}^* \otimes \overline{x} \quad (11)$$

For the case of anisotropic noise, however, an optimum detector should include the correlation properties of the noise in the correlation receiver as this is defined in Eq. (10).

For plane wave arrivals that are observed by an N -sensor array receiver the test statistics are [31]:

$$\lambda_\tau = \sum_{i=1}^{\frac{M_s-1}{2}} \overline{X}^*(f_i) \cdot R_\varepsilon'(f_i) \cdot S(f_i, \phi, \theta) \cdot [S(f_i, \phi, \theta) + R_\varepsilon'(f_i)]^{-1} \cdot \overline{X}(f_i) \quad (12)$$

where, the above statistics are for the frequency domain with parameters defined in Eqs. (7), (8) in the previous section 2.2. Then, for the case of an array of sensors receiving plane wave signals, the log likelihood ratio λ_τ in Eq. (12) is expressed by the following equation,

which is the result of simple matrix manipulations based on the frequency domain expressions (7), (8) and their parameter definitions presented in Section 2.2. Thus,

$$\lambda_\tau = \sum_{i=1}^{\frac{M}{2}-1} \left| \varphi(f_i) \overline{D}^*(f_i, \phi, \theta) R_\varepsilon'(f_i)^{-1} \overline{X}(f_i) \right|^2, \quad (13)$$

where [31],

$$\varphi^2(f_i) = \frac{A_s(f_i) / \sigma_n^2(f_i)}{1 + A_s(f_i) \overline{D}^*(f_i, \phi, \theta) R_\varepsilon'^{-1}(f_i) \overline{D}(f_i) / \sigma_n^2(f_i)}. \quad (14)$$

Eq. (13) can be written also as follows,

$$\lambda_\tau = \sum_{i=1}^{\frac{M}{2}-1} \left[\sum_{n=1}^N \zeta_n^*(f_i, \phi, \theta) X_n(f_i) \right]^2. \quad (15)$$

This last expression (15) of the log likelihood ratio indicates that an optimum detector in this case requires the filtering of each one of the N -sensor received time series $X_n(f_i)$ with a set of filters being the elements of the vector,

$$\overline{\zeta}(f_i, \phi, \theta) = \varphi(f_i) \overline{D}^*(f_i, \phi, \theta) R_\varepsilon'(f_i)^{-1}. \quad (16)$$

Then, the summation of the filtered sensor outputs in frequency domain according to Eq. (16) provides the test statistics for optimum detection. For the simple case of white noise

$R_\varepsilon' = \sigma_n^2 I$ and for a line array receiver, the filtering operation in (16) indicates plane wave conventional beamforming in the frequency domain,

$$\lambda_\tau = \sum_{i=1}^{\frac{M}{2}-1} \left[\psi \sum_{n=1}^N d_n^*(f_i, \theta) X_n(f_i) \right]^2, \quad (17)$$

where, $\psi = \zeta / (1 + N\zeta)$, is a scalar, which is a function of the signal-to-noise ratio, $\zeta = A_s^2 / \sigma_n^2$.

For the case of narrowband signals embedded in spatially and/or temporally correlated noise, it has been shown [13] that the deployment of very long arrays or application of acoustic synthetic aperture will provide sufficient array gain and will achieve optimum detection and estimation for the parameters of interest.

For the general case of broadband and narrowband signals embedded in a spatially anisotropic and temporally correlated noise field, expression (17) indicates that the filtering operation for optimum detection and estimation requires adaptation of the ultrasound signal processing according to the human body's noise characteristics, respectively. The family of algorithms for optimum beamforming that use the characteristics of the noise, are called *Adaptive Beamformers* [3,17-20,22,23]; and a detailed definition of an adaptation process requires knowledge of the correlated noise's covariance matrix $R_e'(f_i)$. However, if the required knowledge of the noise's characteristics is inaccurate, the performance of the optimum beamformer will degrade dramatically [18,23]. As an example, the case of cancellation of the desired signal is often typical and significant in adaptive beamforming applications [18,24]. This suggests that the implementation of useful adaptive beamformers in real time operational systems is not a trivial task. The existence of numerous articles on adaptive beamforming suggests the dimensions of the difficulties associated with this type of implementation. In order to minimize the generic nature of the problems associated with adaptive beamforming the concept of partially adaptive beamformer design was introduced. This concept reduces the degrees of freedom, which results in lowering the computational requirements and often improving the adaptive response time [17,18]. However, the penalty associated with the reduction of the degrees of freedom in partially adaptive beamformers is that they cannot converge to the same optimum solution as the fully adaptive beamformer.

Although a review of the various adaptive beamformers would seem relevant at this point, we believe that this is not necessary since there are excellent review articles [3,17,18,21] that summarize the points that have been considered for the material of this report. There are two main families of adaptive beamformers, the Generalized Sidelobe Cancellers (GSC) [44,45] and the Linearly Constrained Minimum Variance Beamformers (LCMV) [18]. A special case of the LCMV is Capon's Maximum Likelihood Method [22], which is called Minimum Variance Distortionless Response (MVDR) [17,18,22,23,38,39]. This algorithm has proven to be one of the more robust of the adaptive array beamformers and it has been used by numerous researchers as a basis to derive other variants of MVDR [18]. In this report we will address implementation issues for various partially adaptive variants of the MVDR and a GSC adaptive beamformer [1], which are discussed in Section 4.2.

In summary, the classical estimation problem assumes that the *a priori* probability of the signal's presence $p(H_1)$ is unity [31-33]. However, if the signal's parameters are not known *a priori* and $p(H_1)$ is known to be less than unity, then a series of detection decisions over an exhaustive set of source parameters constitutes a detection procedure, where the results incidentally provide an estimation of source's parameters. As an example, we consider the case of a matched filter, which is used in a sequential manner by applying a series of matched filter detection statistics to estimate the range and speed of the target, which are not known *a priori*. This type of estimation procedure is not optimal since it does not constitute an appropriate form of Bayesian minimum variance or minimum mean square error procedure.

Thus, the problem of detection [31-33] is much simpler than the problem of estimating one or more parameters of a detected signal. Classical decision theory [31-33] treats signal detection and signal estimation as separate and distinct operations. A detection decision as to the presence or absence of the signal is regarded as taking place independently of any

signal parameter or waveform estimation that may be indicated as the result of detection decision. However, interest in joint or simultaneous detection and estimation of signals arises frequently. Middleton and Esposito [46] have formulated the problem of simultaneous optimum detection and estimation of signals in noise by viewing *estimation* as a generalized detection process. Practical considerations, however, require different cost functions for each process [46]. As a result, it is more effective to retain the usual distinction between detection and estimation.

Estimation, in ultrasound systems, includes both the temporal and spatial structure of an observed signal field. For active systems, correlation processing and Doppler (for moving target indications) are major concerns that define the critical distinction between these two approaches (i.e. *passive, active*) to ultrasound processing. In this report, we restrict our discussion only to topics related to spatial signal processing for estimating signal parameters, which is associated with the image reconstruction process of ultrasound systems. However, spatial signal processing has a direct representation that is analogous to the frequency-domain representation of temporal signals. Therefore, the spatial signal processing concepts discussed here have direct applications to temporal spectral analysis.

2.4 Cramer-Rao Lower Bound (CRLB) Analysis

Typically, the performance of an estimator is represented as the variance in the estimated parameters. Theoretical bounds associated with this performance analysis are specified by the Cramer-Rao bound [31-33] and that has led to major research efforts by the sonar signal processing community in order to define the idea of an optimum processor for discrete sensor arrays [12,16, 56-60]. If the *a priori* probability of detection is close to unity then the minimum variance achievable by any unbiased estimator is provided by the *Cramer-Rao Lower Bound* (CRLB) [31,32,46].

More specifically, let us consider that the received signal by the n^{th} sensor of a receiving array is expressed by,

$$x_n(t_i) = s_n(t_i) + \varepsilon_n(t_i) \quad (18)$$

where, $s_n(t_i, \bar{\Theta}) = s_n[t_i + \tau_n(\theta, \phi)]$, defines the received signal model with $\tau_n(\theta, \phi)$ being the time delay between the $(n-1)^{\text{st}}$ and the n^{th} sensor of the array for an incoming plane wave with direction of propagation of azimuth angle and an elevation angle ϕ , as depicted in Figure 3. The vector $\bar{\Theta}$, includes all the unknown parameters considered in relation (18). Let $\sigma_{\theta_i}^2$ denote the variance of an unbiased estimate of an unknown parameter θ_i in the vector $\bar{\Theta}$. The Cramer-Rao [31-33] bound states that the best unbiased estimate $\tilde{\Theta}$ of the parameter vector $\bar{\Theta}$ has the covariance matrix

$$\text{cov} \tilde{\Theta} \geq J(\bar{\Theta})^{-1}, \quad (19)$$

where J is the Fisher information matrix whose elements are:

$$J_{ij} = -E \left(\frac{\partial^2 \ln P(\bar{X} | \bar{\Theta})}{\partial \theta_i \partial \theta_j} \right). \quad (20)$$

In Eq. (20), $P(\bar{X} | \bar{\Theta})$, is the probability density function (pdf) governing the observations:

$\bar{X} = [x_1(t_i), x_2(t_i), x_3(t_i), \dots, x_N(t_i)]^*$, for each of the N and M_s independent spatial and temporal samples respectively that are described by the model in Eq. (18). The variance of the unbiased estimates $\tilde{\Theta}$ has a lower bound (called the CRLB), which is given by the diagonal elements of expression (19). This CRLB is used as standard of performance and provides a good measure for the performance of a signal-processing algorithms which gives unbiased estimates $\tilde{\Theta}$ for the parameter vector $\bar{\Theta}$. In this case, if there exists a signal processor to achieve the CRLB, it will be the maximum-likelihood estimation (MLE) technique. The above requirement associated with the *a priori* probability of detection is very essential because if it is less than one, then the estimation is biased and the theoretical CRLBs do not apply. This general framework of optimality is very essential in order to account for Middleton's [32] warning that a system optimized for the one function (detection or estimation) may not be necessarily optimized for the other. For a given model describing the received signal by a sonar or ultrasound system, the CRLB analysis can be used as a tool to define the information inherent in a sonar system. This is an important step related to the development of the signal processing concept for a sonar system as well as in defining the optimum sensor configuration arrangement under which we can achieve, in terms of system performance, the optimum estimation of signal parameters of our interest. This approach has been applied successfully to various studies related to the present development [12,15,56-60].

As an example, let us consider the simplest problem of one source with bearing θ_1 being the unknown parameter. Following relation (20), the results of the variance $\sigma_{\theta_1}^2$ in the bearing estimates are,

$$\sigma_{\theta_1}^2 = \frac{3}{2\psi N} \left(\frac{B_w}{\pi \sin \theta_1} \right)^2, \quad (21)$$

where, $\psi = M_s A_1^2 / \sigma_N^2$, the parameter $B_w = \lambda / (N-1)\delta$ gives the beamwidth of the physical aperture that defines the angular resolution associated with the

estimates of θ_1 . The signal to noise ratio (SNR) at the sensor level is

$$SNR = 10 \times \log_{10}(\psi) \text{ or}$$

$$SNR = 20 \times \log_{10}(A_1 / \sigma_1) + 10 \times \log_{10}(M_s) \quad (22)$$

It is obvious from the above relations (21) and (22) that the variance of the bearing $\sigma_{\theta_1}^2$ can get smaller when the observation period $T = M_s / f_s$ becomes long and the receiving array size, $L = (N - 1)\lambda$ gets very long.

The next question needed to be addressed is about the unbiased estimator that can exploit this available information and provide results asymptotically reaching the CRLBs. For each estimator it is well known that there is a range of *Signal-to-Noise Ratio* (SNR) in which the variance of the estimates rises very rapidly as SNR decreases. This effect, which is called the *threshold effect of the estimator*, determines the range of SNR of the received signals for which the parameter estimates can be accepted. In passive sonar systems the SNR of signals of interest are often quite low and probably below the threshold value of an estimator. In this case, high frequency resolution in both time and spatial domains for the parameter estimation of narrowband signals is required. In other words, the threshold effect of an estimator determines the frequency resolution for processing and the size of the array receivers required in order to detect and estimate signals of interest that have very low SNR [12,14,53,61,62]. The CRLB analysis has been used in many studies to evaluate and compare the performance of the various non-conventional processing schemes [17,18,55] that have been considered for implementation in the generic beamforming structure to be discussed in Section 4.1. In general, array signal processing includes a large number of algorithms for a variety of systems that are quite diverse in concept. There is a basic point that is common in all of them, however, and this is the beamforming process, which we are going to examine in Section 3.

3. Optimum Estimators for Array Signal Processing

An one dimensional (1-D) device such as a line sensor array satisfies the basic requirements of a spatial filter. It provides direction discrimination, at least in a limited sense, and a signal-to-noise ratio improvement relative to an omni-directional sensor. Because of the simplified mathematics and reduced number of the involved sensors, relative to multi-dimensional arrays, most of the researchers have focused on the investigation of the line sensor arrays in system applications [1-6]. Furthermore, implementation issues of synthetic aperture and adaptive techniques in real time systems have been extensively investigated for line arrays as well [1,5,6,12,17,19,20]. However, the configuration of the array depends on the purpose for which it is to be designed. For example, if a wide range of horizontal angles is to be observed, a circular configuration may be used, that provides beam characteristics that are independent of the direction of steering. Vertical direction may be added by moving into cylindrical configuration [8]. In a more general case, where both vertical and horizontal steering is to be required and where a large range of angles is to be covered, a spherically symmetric array would be desirable [9]. In modern ultrasound imaging systems, planar arrays are required to reconstruct real-time 3-D images. However, the huge computational load required for multi-dimensional conventional and adaptive beamformers makes the applications of these 2-D & 3-D arrays in real-time systems non feasible.

Furthermore, for modern ultrasound systems, it has become a necessity these days that all possible active and passive modes of operation should be exploited under an integrated processing structure that reduces redundancy and provides cost effective real time system solutions [6]. Similarly, the implementation of computationally intensive data adaptive techniques in real time systems is also an issue of equal practical importance. However, when these systems include multi-dimensional (2-D, 3-D) arrays with hundreds of sensors, then the associated beamforming process requires very large memory and very intensive throughput characteristics, something that makes its implementation in real time systems a very expensive and difficult task.

To counter this implementation problem, the present report introduces a generic approach of implementing conventional beamforming processing schemes with integrated passive and active modes of operations in systems that may include, planar, cylindrical or spherical arrays [25-28]. This approach decomposes the 2-D and 3-D beamforming process into sets of line and/or circular array beamformers. Because of the decomposition process, the fully multi-dimensional beamformer can now be divided into sub-sets of coherent processes that can be implemented in small size CPU's that can be integrated under the parallel configuration of existing computing architectures. Furthermore, application of spatial shading for multidimensional beamformers to control side-lobe structures can now be easily incorporated. This is because the problem of spatial shading for line arrays has been investigated thoroughly [36] and the associated results can be integrated into a circular and a multi-dimensional beamformer, which can be decomposed now into coherent sub-sets of line and or circular beamformers of the proposed generic processing structure.

As a result of the decomposition process, provided by the generic processing structure, the implementation effort for adaptive schemes is reduced to implementing adaptive processes

in line and circular arrays. Thus, a multi-dimensional adaptive beamformer can now be divided into two coherent modular steps which lead to efficient system oriented implementations. In summary, the proposed approach demonstrates that the incorporation of adaptive schemes with near-instantaneous convergence in multi-dimensional arrays is feasible [7,25-28].

At this point it is important to note that the proposed decomposition process of 2-D and 3-D conventional beamformers into sets of line and/or circular array beamformers is an old concept that has been exploited over the years by sonar system designers. Thus, references on this subject may exist in reports of Navy laboratories and industrial institutes that are not always readily available and the authors' of this document are not aware of any type of reports in this area. Previous efforts attempted to address practical implementation issues and had been focused on cylindrical arrays. As an example, a cylindrical array beamformer is decomposed into time-delay line array beamformers providing beams along elevation angles of the cylindrical array. These are called staves. Then, the beam time series associated with a particular elevation steering of interest are provided at the input of a circular array beamformer.

In this report the attempt is to provide a higher degree of development than the one discussed above for cylindrical arrays. The task is to develop a generic processing structure that integrates the decomposition process of multi-dimensional planar, cylindrical and spherical array beamformers into line and or circular array beamformers. Furthermore, the proposed generic processing structure integrates passive and active modes of operation into a single signal processing scheme.

3.1 Generic Multi-Dimensional Conventional Beamforming Structure

3.1.1 Line-Array Conventional Beamformer

Consider an N -sensor line array receiver with uniform sensor spacing δ , shown in Figure 5, receiving plane-wave arrivals with direction of propagation θ . Then, as a follow up of the parameter definition in Section 2,

$$\tau_n(\theta) = (n-1)\delta \cos \theta / c , \quad (23)$$

is the time delay between the 1st and the n^{th} sensor of the line array for an incoming plane wave with direction θ , as this is illustrated in Figures 5 and 6.

$$d_n(f_i, \theta) = \exp \left[j 2 \pi \frac{(i-1)f_s}{M} \tau_n(\theta) \right] , \quad (24)$$

is the n^{th} term of the steering vector $\bar{D}(f, \theta)$. Moreover, because of relations (16) and (17) the plane wave response of the N -sensor line array steered at a direction θ_s can be expressed by,

$$B(f, \theta_s) = \bar{D}^*(f, \theta_s) \bar{X}(f). \quad (25)$$

Previous studies [1] have shown that for a single source this conventional beamformer without shading is an optimum processing scheme for bearing estimation. The side lobe structure can be suppressed at the expense of a beam width increase by applying different weights (i.e., spatial shading window) [36]. The angular response of a line-array is ambiguous with respect to the angle θ_s , responding equally to targets at angle θ_s and $-\theta_s$ where θ_s varies over $[0, \pi]$.

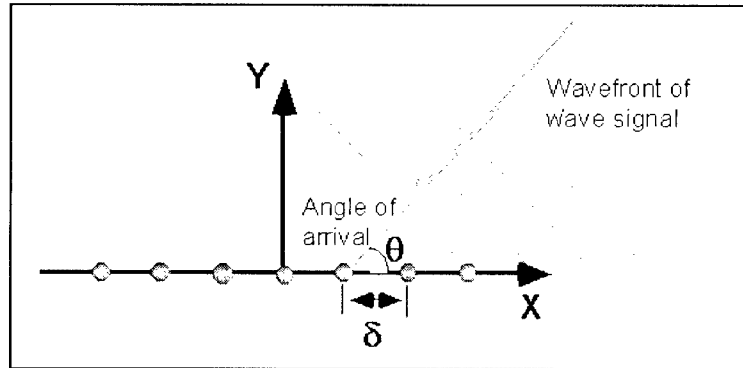


Figure 6. Geometric configuration and coordinate system for a line array.

Eq. (25) is basically a mathematical interpretation of Figure 6 and shows that a line array is basically a spatial filter because by steering a beam in a particular direction we spatially filter the signal coming from that direction, as this is illustrated in Figure 5. On the other hand, Eq. (25) is fundamentally a discrete Fourier transform relationship between the hydrophone weightings and the beam pattern of the line array and as such it is computationally a very efficient operation. However, Eq. (25) can be generalized for non-linear 2-dimensional and 3-dimensional arrays and this is discussed in the next section.

As an example, let us consider a distant monochromatic source. Then the plane wave signal arrival from the direction θ received by a N -hydrophone line array is expressed by Eq. (24). The beam power pattern $P(f, \theta_s)$ is given by $P(f, \theta_s) = B(f, \theta_s) \times B^*(f, \theta_s)$ that takes the form

$$P(f, \theta_s) = \sum_{n=1}^N \sum_{m=1}^N X_n(f) X_m^*(f) \exp \left[\frac{j 2 \pi f \delta_{nm} \cos \theta_s}{c} \right], \quad (26)$$

where δ_{nm} is the spacing $\delta(n-m)$ between the n^{th} and m^{th} sensors. As a result of Eq. (26), the expression for the power beam pattern $P(f, \theta_s)$, is reduced to:

$$P(f, \theta_s) = \left\{ \frac{\sin \left[N \frac{\pi \delta}{\lambda} (\sin \theta_s - \sin \theta) \right]}{\sin \left[\frac{\pi \delta}{\lambda} (\sin \theta_s - \sin \theta) \right]} \right\}^2. \quad (27)$$

Let us consider for simplicity the source bearing θ to be at array broadside, $\delta = \lambda/2$ and $L = (N-1)\delta$ is the array size. Then Equation (27) is modified as [4,10]:

$$P(f, \theta_s) = \frac{N^2 \sin^2 \left[\frac{\pi L \sin \theta_s}{\lambda} \right]}{\left(\frac{\pi L \sin \theta_s}{\lambda} \right)^2}, \quad (28)$$

which is the farfield radiation or directivity pattern of the line array as opposed to near field regions. The results in Equations (27) and (28) are for a perfectly coherent incident acoustic signal and an increase in array size L results in additional power output and a reduction in beamwidth, which are similar arguments with those associated with the CRLB analysis expressed by Eq. (21). The side-lobe structure of the directivity pattern of a line array, which is expressed by Eq. (27), can be suppressed at the expense of a beamwidth increase by applying different weights. The selection of these weights will act as spatial filter coefficients with optimum performance [5,17,18]. There are two different approaches to select the above weights: **pattern optimization and gain optimization**. For pattern optimization the desired array response pattern $P(f, \theta_s)$ is selected first. A desired pattern is usually one with a narrow main lobe and low sidelobes. The weighting or shading coefficients in this case are real numbers from well known window functions that modify the array response pattern. Harris' review [36] on the use of windows in discrete Fourier transforms and temporal spectral analysis is directly applicable in this case to spatial spectral analysis for towed line array applications.

Using the approximation $\sin \theta \cong \theta$ for small θ at array broadside, the first null in Eq. (25) occurs at $\pi L \sin \theta / \lambda = \pi$ or $\Delta \theta \times L / \lambda \cong 1$. The major conclusion drawn here for line array applications is that [4,10]:

$$\Delta \theta \approx \lambda / L \quad \text{and} \quad \Delta f \times T = 1 \quad (29)$$

where $T=M_s/F_s$ is the sensor time series length. Both the above relations in Eq. (29) express the well known temporal and spatial resolution limitations in line array applications that form the driving force and motivation for adaptive and synthetic aperture signal processing that we will discuss later.

An additional constraint for sonar and ultrasound applications requires that the frequency resolution Δf of the hydrophone time series for spatial spectral analysis that is based on FFT beamforming processing must be such that

$$\Delta f \times \frac{L}{c} \ll 1 \quad (30)$$

in order to satisfy *frequency quantization* effects associated with discrete frequency domain beamforming following the FFT of sensor data [17,42]. This is because, in conventional beamforming **F**inite-duration **I**mpulse **R**esponse (FIR) filters are used to provide realizations in designing digital phase shifters for beam steering. Since fast-convolution signal processing operations are part of the processing flow of a sonar signal processor, the effective beamforming filter length needs to be considered as the overlap size between successive snapshots. In this way, the overlap process will account for the wraparound errors that arise in the fast-convolution processing [1,40-42]. It has been shown [42] that an approximate estimate of the effective beamforming filter length is provided by Eqs. (28) and (30).

Because of the linearity of the conventional beamforming process, an exact equivalence of the frequency domain narrowband beamformer with that of the time-domain beamformer for broadband signals can be derived [42,43]. Based on the model of Figure 3, the time-domain beamformer is simply a time delaying [43] and summing process across the hydrophones of the line array, which is expressed by,

$$b(\theta_s, t_i) = \sum_{n=1}^N x_n(t_i - \tau_s) \quad (31)$$

Since,

$$b(\theta_s, t_i) = \text{IFFT}\{B(f, \theta_s)\} \quad (32)$$

by using FFTs and fast convolution procedures, continuous beam-time sequences can be obtained at the output of the frequency domain beamformer [42]. This is a very useful operation when the implementation of beamforming processors in sonar systems is considered.

The beamforming operation in Eq. (31) is not restricted only for plane wave signals. More specifically, consider an acoustic source at the near field of a line array with r_s the source range and θ its bearing. Then the time delay for steering at θ is

$$\tau_s = (r_s^2 + d_{nm}^2 - 2r_s d_{nm} \cos \theta)^{1/2} / c \quad (33)$$

As a result of Eq. (33), the steering vector $d_n(f, \theta_s) = \exp[j2\pi f \tau_s]$ will include two parameters of interest, the bearing θ and range r_s of the source. In this case the beamformer is called *focussed beamformer*, which is used mainly in ultrasound system applications. There are, however, practical considerations restricting the application of the focused beamformer in passive sonar line array systems and these have to do with the fact that effective range focussing by a beamformer requires extremely long arrays.

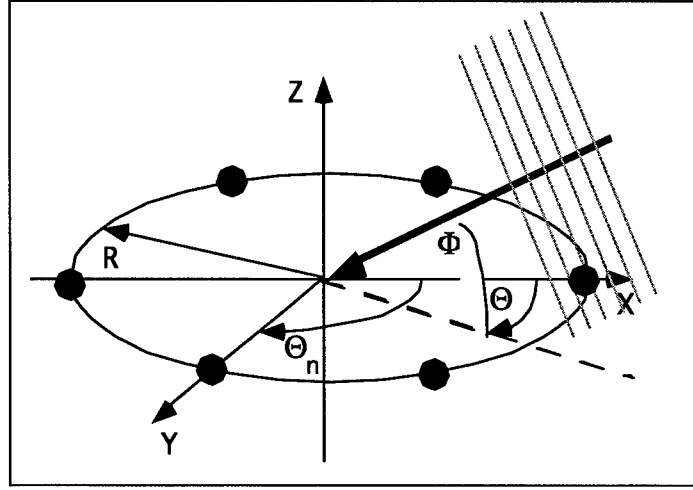


Figure 7. Geometric configuration and coordinate system for a circular array of sensors.

3.1.2 Circular Array Conventional Beamformer

Consider M -sensors distributed uniformly on a ring of radius R receiving plane-wave arrivals at an azimuth angle θ and an elevation angle ϕ as shown in Figure 7. The plane-wave response of this circular array for azimuth steering θ_s and an elevation steering ϕ_s can be written as follows:

$$B(f, \theta_s, \phi_s) = \bar{D}^*(f, \theta_s, \phi_s) W(\theta_s) \bar{X}(f) \quad (34)$$

where $\bar{D}(f, \theta_s, \phi_s)$ is the steering vector with the n^{th} term being expressed by $d_n(f, \theta_s, \phi_s) = \exp(j2\pi f R \sin \phi_s \cos(\theta_s - \theta_n) / c)$ and $\theta_n = 2\pi n / M$ is the angular location of the n^{th} sensor with $m = 0, 1, \dots, M-1$. $W(\theta_s)$ is a diagonal matrix with the off diagonal terms being zero and the diagonal terms being the weights of a spatial window to

reduce the side-lobe structure [36]. This spatial window, in general, is not uniform and depends on the sensor location (θ_m) and the beam steering direction (θ_s). The beam power pattern $P(f, \theta_s, \phi_s)$ is given by $P(f, \theta_s, \phi_s) = B(f, \theta_s, \phi_s) \times B^*(f, \theta_s, \phi_s)$. The azimuth angular response of the circular array covers the range $[0, 2\pi]$ and therefore there is no ambiguity with respect to the azimuth angle θ .

3.2 Multidimensional (3-D) Array Conventional Beamformer

Presented in this section is a generic approach to decompose the planar, cylindrical and spherical array beamformers into coherent sub-sets of line and/or circular array beamformers. In this report, we will restrict the discussion to 3D arrays with cylindrical and planar geometric configuration. The details of the decomposition process for spherical arrays are similar and can be found in [7,25-28].

3.2.1 Decomposition Process for 2-D & 3-D Sensor Array Beamformers

3.2.1.1 Cylindrical Array Beamformer

Consider the cylindrical array shown in Fig. 8 with \aleph sensors and $\aleph = NM$, where N is the number of circular rings and M is the number of sensors on each ring. The angular response of this cylindrical array to a steered direction at (θ_s, ϕ_s) can be expressed as

$$B(f, \theta_s, \phi_s) = \sum_{r=0}^{N-1} \sum_{m=0}^{M-1} w_{r,m} X_{r,m}(f) d_{r,m}^*(f, \theta_s, \phi_s) \quad (35)$$

where $w_{r,m}$ is the $(r,m)^{\text{th}}$ term of a 3-D spatial window, $X_{r,m}(f)$ is the $(r,m)^{\text{th}}$ term of the matrix $\underline{X}(f)$, or $X_{r,m}(f)$ is the Fourier transform of the signal received by the m^{th} sensor on the r^{th} ring and

$$d_{r,m}(f, \theta_s, \phi_s) = \exp\{j2\pi f[(r\delta_z \cos \phi_s + R \sin \phi_s \cos(\theta_s - \theta_m)/c)]\}$$

is the $(r,m)^{\text{th}}$ steering term of $\overline{D}(f, \theta_s, \phi_s)$. R is the radius of the ring, δ_z is the distance between each ring along z-axis, r is the index for the r^{th} ring and $\theta_m = 2\pi m / M$,

$m = 0, 1, \dots, M-1$. Assuming $w_{r,m} = w_r \times w_m$, Eq. (35) can be rearranged as follows:

$$B(f, \theta_s, \phi_s) = \sum_{r=0}^{N-1} w_r d_r^*(f, \theta_s, \phi_s) \left[\sum_{m=0}^{M-1} X_{r,m}(f) w_m d_m^*(f, \theta_s, \phi_s) \right] \quad (36)$$

where $d_r(f, \theta_s, \phi_s) = \exp\{j2\pi f(r\delta_z \cos \phi_s / c)\}$ is the r^{th} term of the steering vector for line-array beamforming, w_r is the r^{th} term of a spatial window for line array spatial shading, $d_m(f, \theta_s, \phi_s) = \exp\{j2\pi f(R \sin \phi_s \cos(\theta_s - \theta_m) / c)\}$ is the m^{th} term of the steering vector for a circular beamformer, discussed in Section 3.1, and w_m is the m^{th} term of a spatial window for circular array shading. Thus, Eq. (36) suggests the decomposition of the cylindrical array beamformer into two steps, which is a well-known process in array theory. The first step is to perform circular array beamforming for each of the N rings with M sensors on each ring. The second step is to perform line array beamforming along the z -axis on the N -beam time series outputs of the first step. This type of implementation, which is based on the decomposition of the cylindrical beamformer into line and circular array beamformers is shown in Figure 8. The coordinate system is identical to that shown in Figure 6. The decomposition process of Eq. (36) makes also the design and incorporation of 3-D spatial windows much simpler. Non-uniform shading windows can be applied to each circular beamformer to improve the angular response with respect to the azimuth angle, θ . A uniform shading window can then be applied to the line array beamformer to improve the angular response with respect to the elevation angle, ϕ . Moreover, the decomposition process, shown in Figure 8, leads to an efficient implementation in computing architectures based on the following two factors:

- The number of sensors for each of these circular and line array beamformers is much less than the total number of sensors, N , of the cylindrical array. The proposed decomposition process for the 3-D beamformer eliminates the need for very large memory and CPU's with very high throughput requirements in one board for real time system applications.
- All the circular and line array beamformers can be executed in parallel, which allows their implementations in much simpler parallel architectures with simpler CPU's,

which is a practical requirement for real time system applications.

Thus, under the restriction $w_{r,m} = w_r \times w_m$ for 3-D spatial shading, the decomposition process provides equivalent beam time series as with those that would have been provided by a 3-D cylindrical beamformer, as this is shown by Eqs. (35) & (36).

3.2.1.2 Planar Array Beamformer

Consider the discrete planar array shown in Figure 4 with \aleph sensors where $\aleph = NM$ and M, N are the number of sensors along x-axis and y-axis, respectively. The angular response of this planar array to a steered direction (θ_s, ϕ_s) can be expressed as,

$$B(f, \theta_s, \phi_s) = \sum_{r=0}^{N-1} \sum_{m=0}^{M-1} w_{r,m} X_{r,m}(f) d_{r,m}^*(f, \theta_s, \phi_s), \quad (37)$$

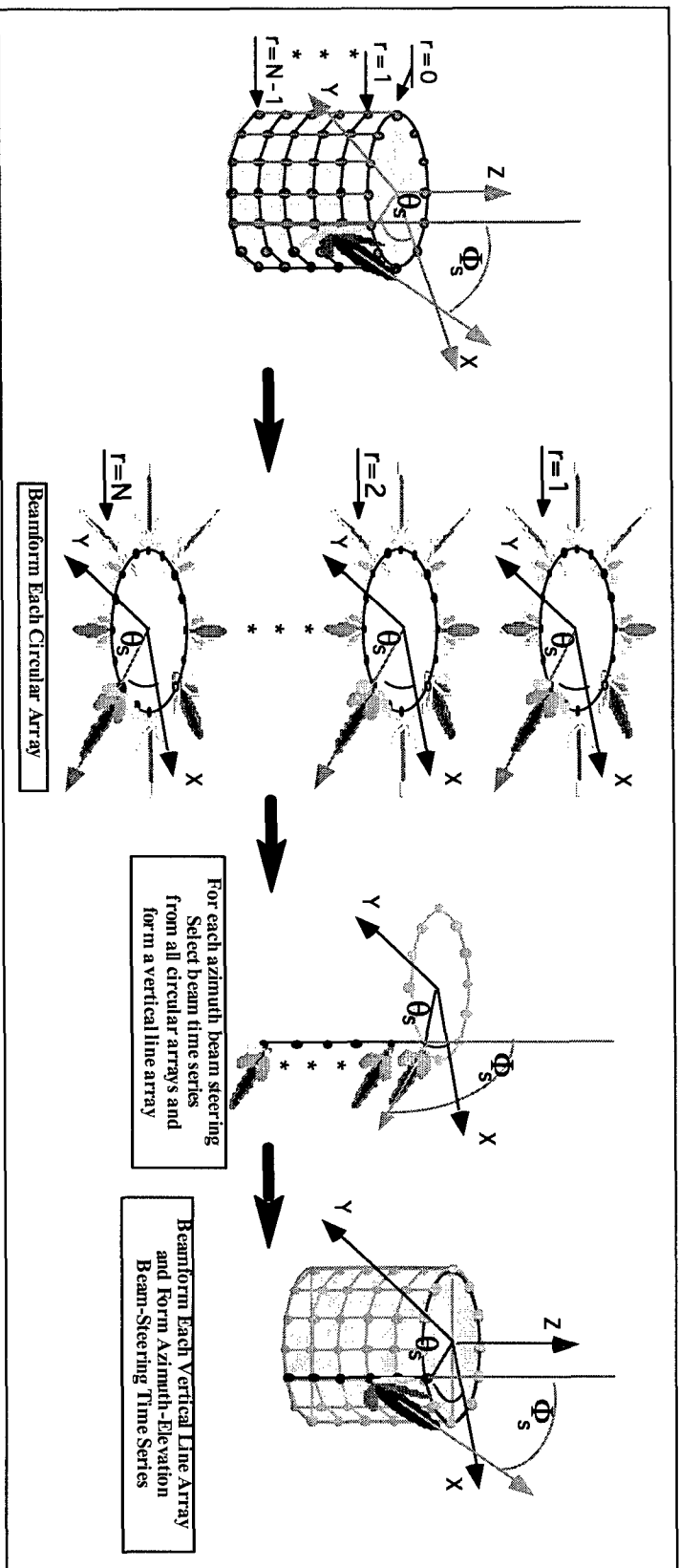


Figure 8. Coordinate system and geometric representation of the concept of decomposing a cylindrical array beamformer. The $N = NM$ sensor cylindrical array beamformer consists of N circular arrays with M being the number of sensors in each circular array. Then, the beamforming structure for cylindrical arrays is reduced into coherent sub-sets of circular (for $0^\circ - 360^\circ$ azimuth bearing estimates) and line array (for $0^\circ - 180^\circ$ angular elevation bearing estimates) beamformers.

where $w_{r,m}$ is the $(r,m)^{\text{th}}$ term of matrix $W(\theta, \phi)$ including the weights of a 2-D spatial window, $X_{r,m}(f)$ is the $(r,m)^{\text{th}}$ term of the matrix $\underline{X}(f)$ including the Fourier transform of the received signal by the $(m,r)^{\text{th}}$ sensor along x-axis and y-axis, respectively. $\underline{D}(f, \theta_s, \phi_s)$ is the steering matrix having its $(r,m)^{\text{th}}$ term defined by

$$d_{r,m}(f, \theta_s, \phi_s) = \exp(j2\pi f(m\delta_x \sin \theta_s + r\delta_y \cos \theta_s \cos \phi_s) / c)$$

Assuming that the matrix of spatial shading (weighting) $W(\theta, \phi)$ is separable (i.e., $\underline{W}(\theta, \phi) = \underline{W}_1(\theta)\underline{W}_2(\phi)$), Eq. 37 can be simplified as follows:

$$B(f, \theta_s, \phi_s) = \sum_{r=0}^{N-1} w_{1,r} d_r^*(f, \theta_s, \phi_s) \left[\sum_{m=0}^{M-1} w_{2,m} X_{r,m}(f) d_m^*(f, \theta_s, \phi_s) \right], \quad (38a)$$

where, $d_r(f, \theta_s, \phi_s) = \exp(j2\pi f r \delta_y \cos \theta_s \cos \phi_s / c)$, is the r^{th} term of the steering vector, $\overline{D}_y(f, \theta_s, \phi_s)$ and $d_m(f, \theta_s, \phi_s) = \exp(j2\pi f m \delta_x \sin \theta_s / c)$ is the m^{th} term of the steering vector, $\overline{D}_x(f, \theta_s, \phi_s)$. The summation term enclosed by parenthesis in Eq. (38a) is equivalent to the response of a line array beamformer along x-axis. Then all the steered beams from this summation term form a vector denoted by $\overline{B}_y(f, \theta_s)$. This vector defines a line array with directional sensors, which are the beams defined by the second summation process of Eq. (38a). Therefore Eq. (38a) can be expressed as:

$$B(f, \theta_s, \phi_s) = \overline{D}_y^*(f, \theta_s, \phi_s) \underline{W}_1(\theta) \overline{B}_y(f, \theta_s). \quad (38b)$$

Eq. (38b) suggests that the 2-D planar array beamformer can be decomposed into two line array beamforming steps. The first step includes a line-array beamforming along x-axis and will be repeated N - times to get the vector $\overline{B}_y(f, \theta_s)$ that includes the beam times series $b_r(f, \theta_s)$, where the index $r = 0, 1, \dots, N-1$ is along the axis y. The second step includes line array beamforming along y-axis and will be done only once by treating the vector $\overline{B}_y(f, \theta_s)$ as the input signal for the line array beamformer to get the output $B(f, \theta_s, \phi_s)$. The separable spatial windows can now be applied separately on each line-array beamformer to suppress sidelobe structures. Figure 4 shows the involved steps of

decomposing the 2-D planar array beamformer into two steps of line-array beamformers. The line array coordinate system is identical with that shown in Figure 6. The decomposition of the planar array beamformer into these two line-array beamforming steps leads to an efficient implementation based on the following two factors. First, the number of the involved sensors for each of these line array beamformers is much less than the total number of sensors, N , of the planar array. The proposed decomposition process for the 2-D beamformer eliminates the need for very large memory and CPU's with very high throughput requirements in one board for real time system applications. Secondly, all these line array beamformers can be executed in parallel, which allows their implementation in much simpler parallel architectures with simpler CPU's, which is a practical requirement for real time system application. Besides the advantage of the efficient implementation, the proposed decomposition approach makes the application of the spatial window much simpler to be incorporated.

3.3 Influence of the Medium's Propagation Characteristics on the Performance of a Receiving Array

In ocean acoustics and medical ultrasound imaging, the wave propagation problem is highly complex due to the spatial properties of the non-homogeneous underwater and human body mediums. For stationary source and receiving arrays, the space time properties of the acoustic pressure fields include a limiting resolution imposed by these mediums. This limitation is due either to the angular spread of the incident energy about a single arrival as a result of the scattering phenomena, or to the multipaths and their variation over the aperture of the receiving array.

More specifically, an acoustic signal that propagates through anisotropic mediums will interact with the transmitting medium microstructure and the rough boundaries, resulting in a net field that is characterized by irregular spatial and temporal variations. As a consequence of these interactions, a point source detected by a high-angular resolution receiver is perceived as a source of finite extent. It has been suggested [47] that due to the above spatial variations the sound field consists not of parallel, but of superimposed wavefronts of different directions of propagation. As a result, coherence measurements of this field by a receiving array give an estimate for the spatial coherence function. In the model for the spatial uncertainty of the above study [47], the width of the coherence function is defined as the coherence length of the medium and its reciprocal value is a measure of the angular uncertainty caused by the scattered field of the underwater environment.

By the *coherence* of acoustic signals in the sea or in the human body, we mean the degree to which the acoustic pressures are the same at two points in the medium of interest located a

given distance and direction apart. Pressure sensors placed at these two points will have phase coherent outputs if the received acoustic signals are perfectly coherent; if the two sensor outputs, as a function of space or time, are totally dissimilar, the signals are said to be incoherent. Thus, the loss of spatial coherence results in an upper limit on the useful aperture of a receiving array of sensors [10]. Consequently, knowledge of the angular uncertainty of the signal caused by the medium is considered essential in order to determine quantitatively the influence of the medium on the array gain, which is also influenced significantly by a partially directive anisotropic noise background. Therefore, for a given non-isotropic medium, it is desirable to estimate the optimum array size and achievable array gain for sonar and ultrasound array applications.

For geometrical simplicity and without any loss of generality we consider the case of a receiving line array. Quantitative estimates of the spatial coherence for a receiving line array are provided by the cross spectral density matrix in frequency domain between any set of two sensor time series of the line array. An estimate of the cross spectral density matrix $R(f)$ with its nm^{th} term defined by

$$R_{nm}(f, \delta_{nm}) = E[X_n(f)X_m^*(f)] \quad , \quad (39)$$

The above space-frequency correlation function can be related to the angular power directivity pattern of the source, $\Psi_s(f, \theta)$, via a Fourier transformation by using a generalization of Bello's concept [48] of time-frequency correlation function $[t \Leftrightarrow 2\pi f]$ into space $[\delta_{nm} \Leftrightarrow 2\pi f \sin \theta / c]$, which gives

$$R_{nm}(f, \delta_{nm}) = \int_{-\pi/2}^{\pi/2} \Psi_s(f, \theta) \exp\left[\frac{-j2\pi f \delta_{nm} \theta}{c}\right] d\theta \quad , \quad (40)$$

or

$$\Psi_s(f, \theta) = \int_{-N\delta/2}^{N\delta/2} R_{nm}(f, \delta_{nm}) \exp\left[\frac{j2\pi f \delta_{nm} \theta}{c}\right] d(\delta_{nm}) \quad , \quad (41)$$

The above transformation can be converted into the following summation:

$$R_{nm}(f_o, \delta_{nm}) = \Delta\theta \sum_{g=-G/2}^{G/2} \Psi_s(f_o, \theta_g) \exp\left[\frac{-j2\pi f_o \delta_{nm} \sin(g\Delta\theta)}{c}\right] \cos(g\Delta\theta) \quad , \quad (42)$$

where $\Delta\theta$ is the angle increment for sampling the angular power directivity pattern, $\theta_g = g\Delta\theta$, g is the index for the samples and G is the total number of samples.

For line array applications, the power directivity pattern (calculated for a homogeneous free space) due to a distant source, which is treated as a point source, should be a delta function.

Estimates, however, of the source's directivity from a line array operating in an anisotropic ocean are distorted by the underwater medium. In other words, the directivity pattern of the received signal is the convolution of the original pattern and the angular directivity of the medium (i.e., the angular scattering function of the underwater environment). As a result of the above, the angular pattern of the received signal, by a receiving line array system, is the scattering function of the medium.

In this report, the concept of spatial coherence is used to determine the statistical response of a line array to the acoustic field. This response is the result of the multipath and scattering phenomena discussed before, and there are models [10,47] to relate the spatial coherence with the physical parameters of an anisotropic medium for measurement interpretation. In these models, the interaction of the acoustic signal with the transmitting medium is considered to result in superimposed wavefronts of different directions of propagation. Then Eqs. (24), (25), which define a received sensor signal from a distant source, are expressed by

$$x_n(t_i) = \sum_{l=1}^J A_l \exp \left[-j2\pi f_l \left(t_i - \frac{\delta(n-1)}{c} \theta_l \right) \right] + \varepsilon_{n,i}(0, \sigma_e) , \quad (43)$$

where $l = 1, 2, \dots, J$, and J is the number of superimposed waves. As a result, a generalized form of the crosscorrelation function between two sensors, which has been discussed by Carey and Moseley [10], is

$$R_{nm}(f, \delta_{nm}) = \tilde{X}^2(f) \exp \left[- \left(\frac{\delta_{nm}}{L_c} \right)^k \right], \quad k = 1, \text{ or } 1.5 \text{ or } 2, \quad (44)$$

where L_c is the correlation length and $\tilde{X}^2(f)$ is the mean acoustic intensity of a received sensor time sequence at the frequency bin f . A more explicit expression for the Gaussian form of Eq. (44) is given in [47],

$$R_{nm}(f, \delta_{nm}) \approx \tilde{X}^2(f) \exp \left[- \left(\frac{2\pi f \delta_{nm} \sigma_\theta}{c} \right)^2 / 2 \right], \quad (45)$$

and the crosscorrelation coefficients are given from

$$\rho_{nm}(f, \delta_{nm}) = R_{nm}(f, \delta_{nm}) / \tilde{X}^2(f). \quad (46)$$

At the distance $L_c = c / (2\pi f \sigma_\theta)$, called "*the coherence length*", the correlation function in Eq. (46) will be 0.6. This critical length is determined from experimental coherence measurements plotted as a function of δ_{nm} . Then a connection between the medium's angular uncertainty and the measured coherence length is derived as

$$\sigma_\theta = 1 / L_c, \quad \text{and} \quad L_c = 2 \pi \delta_{lm} f / c \quad (47)$$

here δ_{lm} is the critical distance between the first and the m th sensors at which the coherence measurements get smaller than 0.6. Using the above parameter definition, the effective aperture size and array gain of a deployed towed line array can be determined [10,47] for a specific underwater ocean environment.

Since the correlation function for a Gaussian acoustic field is given by Eq. (45), the angular scattering function $\Phi(f, \theta)$ of the medium can be derived. Using Eq. (41) and following a rather simple analytical integral evaluation, we have

$$\Phi(f, \theta) = \frac{1}{\sigma_\theta \sqrt{2\pi}} \exp \left[-\frac{\theta^2}{2\sigma_\theta^2} \right] \quad (48)$$

where $\sigma_\theta = c/(2\pi f \delta_{lm})$. This is an expression for the angular scattering function of a Gaussian underwater ocean acoustic field [10,47].

It is apparent from the above discussion that the estimates of the cross-correlation coefficients $\rho_{nm}(f, \delta_{nm})$ are necessary in order to define experimentally the coherence length of an underwater or human body medium. For details on experimental studies on coherence estimation for underwater sonar applications the reader may review the references [10, 30].

3.4 Array Gain

The performance of an array of sensors to an acoustic signal embodied in a noise field is characterized by the "array gain" parameter, **AG**. The mathematical relation of this parameter is defined by

$$AG = 10 \log \frac{\sum_{n=1}^N \sum_{m=1}^N \tilde{\rho}_{nm}(f, \delta_{nm})}{\sum_{n=1}^N \sum_{m=1}^N \tilde{\rho}_{\epsilon, nm}(f, \delta_{nm})} \quad (49)$$

where $\rho_{nm}(f, \delta_{nm})$ and $\rho_{\epsilon, nm}(f, \delta_{nm})$ denote the normalized crosscorrelation coefficients of the signal and noise field, respectively. Estimates of the correlation coefficients are given from Eq. (46). If the noise field is isotropic that it is not partially directive, then the

denominator in Eq. (49) is equal to N , (i.e. $\sum_{n=1}^N \sum_{m=1}^N \tilde{\rho}_{\epsilon, nm}(f, \delta_{nm}) = N$),

because the non diagonal terms of the cross-correlation matrix for the noise field are negligible. Then Equation (49) simplifies to,

$$AG = 10 \log \frac{\sum_{n=1}^N \sum_{m=1}^N \tilde{\rho}_{nm}(f, \delta_{nm})}{N} \quad (50)$$

For perfect spatial coherence across the line array the normalized crosscorrelation coefficients are $\rho_{nm}(f, \delta_{nm}) \equiv 1$ and the expected values of the array gain estimates are, $AG = 10 \times \log N$. For the general case of isotropic noise and for frequencies smaller than the towed array's design frequency the array gain term **AG** is reduced to the quantity called Directivity Index,

$$DI = 10 \times \log[(N-1)\delta/(\lambda/2)]. \quad (51)$$

When $\delta \ll \lambda$ and the conventional beamforming processing is employed, Eq. (29) indicates that the deployment of very large aperture arrays is required in order to achieve sufficient array gain and angular resolution for precise bearing estimates. Practical deployment considerations, however, usually limit the overall dimensions of an array of sensors. In addition, the medium's spatial coherence [10, 30] sets an upper limit on the effective array length. In general, the medium's spatial coherence length is of the order of $O(10^2)\lambda$ [10,30].

Alternatives to large aperture arrays are signal processing schemes discussed in [1]. Theoretical and experimental investigations have shown that bearing resolution and detectability of weak signals in the presence of strong interferences can be improved by applying non-conventional beamformers such as adaptive beamforming [1-5,17-24], or acoustic synthetic aperture processing [1,11-16] to the sensor time series of deployed short ultrasound arrays, which are discussed in the next section.

4. Advanced Beamformers

4.1 Synthetic Aperture Processing

Various synthetic aperture techniques have been investigated to increase signal gain and improve angular resolution for line array systems. There is a difference, however, between the synthetic aperture concept of ultrasound systems with that for sonar and radar applications. In particular, the concept of synthetic aperture processing in sonar and radar system applications exploits the movement of an array of sensors to synthesize a longer aperture. In ultrasound system applications, the synthetic aperture processing concept integrates the acquired data from sub-apertures of a larger physical array. Thus, for ultrasound systems, the synthetic aperture concept is simpler since there is no movement of the array, while for radar and sonar systems the movement of the array introduces numerous errors and artifacts. In what follows, we will review synthetic aperture techniques for sonar applications that have been tested successfully with real data [11-16]. The same techniques can be implemented successfully in ultrasound systems and this will be demonstrated later in the section of this report that includes results from numerical simulations and experimental data.

Let us start with a few theoretical remarks. The plane wave response of a line array to a distant monochromatic signal, received by the n^{th} element of the array, is expressed by Eqs. (23), (24) and (25). In the above expressions, the frequency f includes the Doppler shift due to a combined movement of the receiving array and the source (or object reflecting the incoming acoustic wavefront) radiating signal. Let v , denote the relative speed; it is assumed here that the component of the source's velocity along its bearing is negligible. If f_o is the frequency of the stationary field, then the frequency of the received signal is expressed by

$$f = f_o(1 \pm v \sin \theta / c) \quad (52)$$

and an approximate expression for the received sensor time series (18) and (43) is given by

$$x_n(t_i) = A \exp \left[j 2 \pi f_o \left(t_i - \frac{v t_i + (n-1) \delta}{c} \sin \theta \right) \right] + \varepsilon_{n,i} \quad (53)$$

τ seconds later, the relative movement between the receiving array and the radiated source is $v\tau$. By proper choice of the parameters v and τ , we have $v\tau = q\delta$, where q represents the number of sensor positions that the array has moved, and the received signal, $x_n(t_i + \tau)$ is expressed by,

$$x_n(t_i + \tau) = \exp(j 2 \pi f_o \tau) A \exp \left[j 2 \pi f_o \left(t_i - \frac{v t_i + (q + n - 1) \delta}{c} \sin \theta \right) \right] + \varepsilon_{n,i}^\tau \quad (54)$$

As a result, we have the Fourier transform of $x_n(t_i + \tau)$, as

$$\tilde{X}_n(f)_\tau = \exp(j2\pi f_o \tau) \tilde{X}_n(f) \quad (55)$$

where, $\tilde{X}_n(f)_\tau$ and $\tilde{X}_n(f)$ are the DFTs of $x_n(t_i + \tau)$, and $x_n(t_i)$, respectively. If the phase term $\exp(-j2\pi f_o \tau)$ is used to correct the line array measurements shown in (55), then

the spatial information included in the successive measurements at $t=t_i$ and $t=t_i + \tau$ is equivalent to that derived from a line array of $(q+N)$ sensors. When idealized conditions are assumed, the phase correction factor for (52) in order to form a synthetic aperture, is

$\exp(-j2\pi f_o \tau)$. However, this phase correction estimate requires *a priori* knowledge of

the source receiver relative speed, v and accurate estimates for the frequency f of the received signal. An additional restriction is that the synthetic aperture processing techniques have to compensate for the disturbed paths of the receiving array during the integration period that the synthetic aperture is formed. Moreover, the temporal coherence of the source signal should be greater or at least equal to the integration time of the synthetic aperture.

1. At this point it is important to review a few fundamental physical arguments associated with passive synthetic aperture processing. In the past [13] there was a conventional wisdom regarding synthetic aperture techniques, which held that practical limitations prevent them from being applicable to real-world systems. The issues were threshold.
2. Since passive synthetic aperture can be viewed as a scheme that converts temporal gain to spatial gain, most signals of interest do not have sufficient temporal coherence to allow a long spatially coherent aperture to be synthesized.
3. Since past algorithms required *a priori* knowledge of the source frequency in order to compute the phase correction factor, as shown by (52)-(55), the method was essentially useless in any bearing estimation problem since Doppler would introduce an unknown bias on the frequency observed at the receiver.

Since synthetic aperture processing essentially converts temporal gain to spatial gain, there was no "new" gain to be achieved, and therefore, no point to the method.

Recent work [12-16] has shown that there can be realistic conditions under which all of these objections are either not relevant or do not constitute serious impediments to practical applications of synthetic aperture processing in operational systems [1]. Theoretical discussions have shown [13] that the above three arguments are valid for cases that include the formation of synthetic aperture in mediums with isotropic noise characteristic. However, when the noise characteristics of the received signal are non-isotropic and the receiving array includes more than one sensor, then there is spatial gain available from passive synthetic aperture processing and this has been discussed analytically in [13]. Recently, there have been only two passive synthetic aperture techniques [11-16, 54] and an MLE estimator [12] published in the open literature that deal successfully with the above

restrictions. For more details about these techniques the reader may review the references [11-16,54,55].

For ultrasound applications, the method that does not require adaptations to address the depth focusing requirements of ultrasound systems is the spatial overlap correlator method (ETAM Algorithm), which is discussed in detail in [1, 11-16].

4.2 Adaptive Beamformers

Despite the geometric differences between the line and circular arrays, the underlying beamforming processes for these arrays, as expressed by Eqs. (11) & (12) respectively, are time delay beamforming estimators, which are basically spatial filters. However, optimum beamforming requires the beamforming filter coefficients to be chosen based on the covariance matrix of the received data by the N -sensor array in order to optimize the array response [15,16], as discussed in Section 2. The family of algorithms for optimum beamforming that use the characteristics of the noise, are called *Adaptive Beamformers* [3,17,18,19,20,22,23]. In this section we will address implementation issues for various partially adaptive variants of the MVDR method and a GSC adaptive beamformer [1,37].

Furthermore, the implementation of adaptive schemes in real time systems is not restricted into one method, such as the MVDR technique that is discussed next. In fact, the generic concept of the sub-aperture multi-dimensional array introduced in the paper allows for the implementation of a wide variety of adaptive schemes in operational systems [7,25-28]. As for the implementation of adaptive processing schemes in active systems, the following issues need to be addressed.

For applications that require Doppler processing, the outputs of the adaptive algorithms are required to provide coherent beam time series to facilitate the post-processing. This means that these algorithms should exhibit near-instantaneous convergence and provide continuous beam time series that have sufficient temporal coherence to correlate with the reference signal in matched filter processing [1].

In a previous study [1], possible improvement in convergence periods of two algorithms in the sub-aperture configuration was investigated. The Griffiths-Jim Generalized Sidelobe Canceller (GSC) [18,44] coupled with the Normalized Least Mean Square (NLMS) adaptive filter [45] has been shown to provide near-instantaneous convergence under certain conditions [1,37]. The GSC/NLMS in the sub-aperture configuration was tested under a variety of conditions to determine if it could yield performance advantages, and if its convergence properties could be exploited over a wider range of conditions [1,37]. The Steered Minimum Variance Beamformer (STMV) is a variant of the Minimum Variance Distortionless Response (MVDR) beamformer [38]. By applying narrowband adaptive processing on bands of frequencies, extra degrees of freedom are introduced. The number of degrees of freedom is equal to the number of frequency bins in the processed band. In other words, increasing the number of frequency bins processed decreases the convergence time by a corresponding factor. This is due to the fact that convergence now depends on the observation time bandwidth product, as opposed to observation time in the MVDR algorithm [38,39].

The STMV beamformer in its original form was a broadband processor. In order to satisfy the requirements for matched filter processing, it was modified to produce coherent beam time series [1]. The ability of the STMV narrowband beamformer to produce coherent beam time series has been investigated in another study [37]. Also, the STMV narrowband processor was implemented in the sub-aperture configuration to produce near-instantaneous convergence and to reduce the computational complexity required. The convergence properties of both the full aperture and sub-aperture implementations have been investigated for line arrays of sensors [1,37].

4.2.1 Minimum Variance Distortionless Response (MVDR)

The goal is to optimize the beamformer response so that the output contains minimal contributions due to noise and signals arriving from directions other than the desired signal direction. For this optimization procedure it is desired to find a linear filter vector $\bar{W}(f_i, \theta)$ which is a solution to the constrained minimization problem that allows signals from the look direction to pass with a specified gain [17,18],

$$\text{Minimize: } \sigma_{MV}^2 = \bar{W}^*(f_i, \theta) R(f_i) \bar{W}(f_i, \theta), \text{ subject to} \\ \bar{W}^*(f_i, \theta) \bar{D}(f_i, \theta) = 1 \quad (56)$$

where $\bar{D}(f_i, \theta)$ is the conventional steering vector based on Eq. (24). The solution is given by,

$$\bar{W}(f_i, \theta) = \frac{R^{-1}(f_i) \bar{D}(f_i, \theta)}{\bar{D}^*(f_i, \theta) R^{-1}(f_i) \bar{D}(f_i, \theta)} \quad (57)$$

The above solution provides the adaptive steering vectors for beamforming the received signals by the N -hydrophone line array. Then in frequency domain, an adaptive beam at a steering θ_s is defined by

$$B(f_i, \theta_s) = \bar{W}^*(f_i, \theta_s) \bar{X}(f_i) \quad (58)$$

and the corresponding conventional beams are provided by Equation (25).

4.2.2 Generalized Sidelobe Canceller (GSC)

The Generalized Sidelobe Canceller (GSC) [44] is an alternative approach to the MVDR method. It reduces the adaptive problem to an unconstrained minimization process. The GSC formulation produces a much less computationally intensive implementation. In general GSC implementations

have complexity $O(N^2)$, as compared to $O(N^3)$ for MVDR implementations, where N is the number of sensors used in the processing. The basis of the reformulation of the problem is the decomposition of the adaptive filter vector $\bar{W}(f_i, \theta)$ into two orthogonal components, \bar{w} and $-\bar{v}$, where \bar{w} and \bar{v} lie in the range and the null space of the constraint of Eq. (56), such that $\bar{W}(f_i, \theta) = \bar{w}(f_i, \theta) - \bar{v}(f_i, \theta)$. A matrix C which is called signal blocking matrix, may be computed from $C \bar{I} = 0$ where \bar{I} is a vector of ones. This matrix C whose columns form a basis for the null space of the constraint of Eq. (56) will satisfy $\bar{v} = C\bar{u}$, where \bar{u} is defined below by Eq. (60). The adaptive filter vector may now be defined as $\bar{W} = \bar{w} - C\bar{u}$ and yields the realization shown in Figure 9. Then the problem is reduced to:

$$\text{Minimize: } \sigma_u^2 = \{[\bar{w} - C\bar{u}]^* R [\bar{w} - C\bar{u}]\} \quad (59)$$

which is satisfied by:

$$\bar{u}_{opt} = (C^* R C)^{-1} C^* R \bar{w} \quad (60)$$

u_{opt} being the value of the weights at convergence.

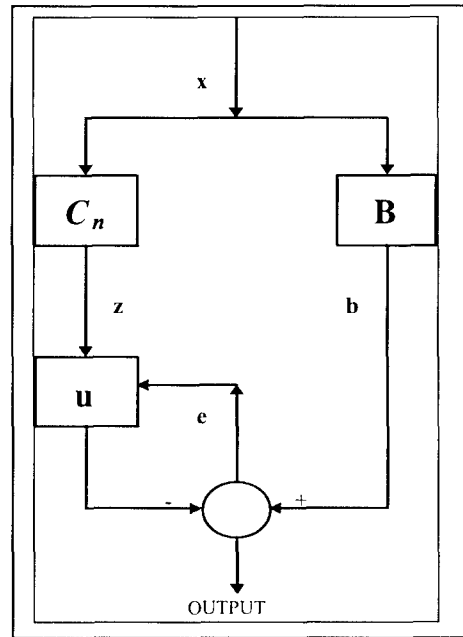


Figure 9. Basic processing structure for the memoryless GSC.

The Griffiths-Jim Generalized Sidelobe Canceller (GSC) in combination with the Normalized Least Mean Square (NLMS) adaptive algorithm has been shown to yield near instantaneous convergence [44,45]. Figure 9 shows the basic structure of the so called Memoryless Generalized Sidelobe Canceller. The time delayed by $\tau_n(\theta_s)$ sensor time series defined by Equations (7),

(23) form the pre-steered sensor time series, which are denoted by $x_n(t_i, \tau_n(\theta_s))$. In frequency domain these pre-steered sensor data are denoted by $X_n(f_i, \theta_s)$ and form the input data vector for the adaptive scheme in Figure 8. On the left hand side branch of this figure the intermediate vector $\bar{Z}(f_i, \theta_s)$ is the result of the signal blocking matrix C being applied to the input $\bar{X}(f_i, \theta_s)$.

Next, the vector $\bar{Z}(f_i, \theta_s)$ is an input to the NLMS adaptive filter. The output of the right hand branch is simply the shaded conventional output. Then, the output of this processing scheme is the difference between the adaptive filter output, and the "conventional" output:

$$e(f_i, \theta_s) = b(f_i, \theta_s) - \bar{u}^*(f_i, \theta_s) \bar{Z}(f_i, \theta_s) \quad (61)$$

The adaptive filter, at convergence, reflects the sidelobe structure of any interferers present, and it is removed from the conventional beamformer output. In the case of the Normalized LMS (NLMS) this adaptation process can be represented by:

$$\bar{u}_{k+1}(f_i, \theta_s) = \bar{u}_k(f_i, \theta_s) + \frac{\mu \times e_k^*(f_i, \theta_s)}{\alpha + \bar{X}^*(f_i, \theta_s) \bar{X}(f_i, \theta_s)} \bar{Z}(f_i, \theta_s) \quad (62)$$

where, k is the iteration number, α is a small positive number designed to maintain stability. The parameter μ is the convergence controlling parameter or "step size" for the NLMS algorithm.

4.2.3 Steered Minimum Variance Broadband Adaptive (STMV)

Krolik and Swingler [38] have shown that the convergence time for broadband source location can be reduced by using the space-time statistic called the steered covariance matrix (STCM). This method achieves significantly shorter convergence times than adaptive algorithms that are based on the narrowband cross spectral density matrix (CSDM) [17,18] without sacrificing spatial resolution. In fact, the number of statistical degrees of freedom available to estimate the STCM is approximately the time-bandwidth product ($T \times BW$) as opposed to the observation time, ($T = M/F_s$, F_s being the sampling frequency) in CSDM methods. This provides an improvement of approximately BW , the size of the broad-band source bandwidth, in convergence time. The conventional beamformer's output in frequency domain is shown by Eq. (25). The corresponding time domain conventional beamformer output $b(t_i, \theta_s)$ is the weighted sum of the steered sensor outputs, as expressed by Eq. (32). Then, the expected broadband beam power, $B(\theta)$ is given by:

$$B(\theta_s) = E\{[b(\theta_s, t_i)]\} = \bar{h}^* E\{\bar{x}^*(t_i, \tau_n(\theta)) \bar{x}(t_i, \tau_m(\theta))\} \bar{h} \quad (63)$$

where the vector \bar{h} includes the weights for spatial shading [36].

$$\text{The term } \Phi(t_i, \theta_s) = E\{\bar{x}(t_i, \tau_n(\theta_s)) \bar{x}^*(t_i, \tau_m(\theta_s))\} \quad (64)$$

is defined as the steered covariance matrix (STCM) in time domain and is assumed to be independent of t_i in stationary conditions. The name STCM is derived from the fact that the matrix is computed by taking the covariance of the presteered time domain sensor outputs. Suppose $X_n(f_i)$ is the Fourier transform of the sensor outputs $x_n(t_i)$ and assuming that the sensor outputs are approximately band limited. Under these conditions the vector of steered (or time delayed) sensor outputs $x_n(t_i, \tau_n(\theta_s))$ can be expressed by

$$\bar{x}(t_i, \tau_n(\theta_s)) = \sum_{k=l}^{l+H} T_k(f_k, \theta_s) \bar{X}(f_k) \exp(j2\pi f_k t_i) \quad (65)$$

where $T(f_k, \theta)$ is the diagonal steering matrix in Eq. (66) below with elements identical to the elements of the conventional steering vector, $\bar{D}(f_i, \theta)$

$$T(f_k, \theta) = \begin{bmatrix} 1 & & & & 0 \\ 0 & d_1(f_k, \theta) & & & \\ \cdot & & \cdot & & \cdot \\ \cdot & & & \cdot & \cdot \\ \cdot & & & & \cdot \\ 0 & & & & d_N(f_k, \theta) \end{bmatrix} \quad (66)$$

Then it follows directly from the above equations that

$$\Phi(\Delta f, \theta_s) = \sum_{k=l}^{l+H} T(f_k, \theta_s) R(f_k) T^*(\theta_s) \quad (67)$$

where the index $k=l, l+1, \dots, l+H$ refers to the frequency bins in a band of interest Δf , and $R(f_k)$ is the Cross Spectral Density Matrix (CSDM) for the frequency bin f_k . This suggests that $\Phi(\Delta f, \theta_s)$ in Eq. (64) can be estimated from the CSDM, $R(f_k)$ and $T(f_k, \theta)$ expressed by Eq. (66). In the steered minimum variance method (STMV), the broadband spatial power spectral estimate $B(\theta_s)$ is given by [38]:

$$B(\theta_s) = [\bar{I}^* \Phi(\Delta f, \theta_s)^{-1} \bar{I}]^{-1} \quad (68)$$

The Steered Minimum Variance Algorithm differs from the basic MVDR algorithm in that the STMV algorithm yields a STCM that is composed from a band of frequencies and the MVDR algorithm uses a CSDM that is derived from a single frequency bin. Thus, the additional degrees of freedom of STMV compared to those of CSDM provide a more robust adaptive process.

However, estimates of $B(\theta)$ according to Eq. (68) do not provide coherent beam time series, since they represent the broadband beam power output of an adaptive process. In this investigation [1] we have modified the estimation process of the STMV matrix in order to get the complex coefficients of $\Phi(\Delta f, \theta_s)$ for all the frequency bins in the band of interest.

The STMV algorithm may be used in its original form to generate an estimate of $\Phi(\Delta f, \theta)$ for all the frequency bands Δf , across the band of the received signal. Assuming stationarity across the frequency bins of a band Δf , then the estimate of the STMV may be consider to be approximately the same with the narrowband estimate $\Phi(f_o, \theta)$ for the center frequency f_o of the band Δf . In this case, the narrowband adaptive coefficients may be derived from

$$\bar{w}(f_o, \theta) = \frac{\Phi(f_o, \Delta f, \theta)^{-1} \bar{D}(f_o, \theta)}{\bar{D}^*(f_o, \theta) \Phi(f_o, \Delta f, \theta)^{-1} \bar{D}(f_o, \theta)}, \quad (69)$$

The phase variations of $\bar{w}(f_o, \theta)$ across the frequency bins $i=l, l+1, \dots, l+H$ (where H is the number of bins in the band Δf), are modeled by,

$$w_n(f_i, \theta) = \exp[2\pi f_i \Psi(\Delta f, \theta)], \quad i=l, l+1, \dots, l+H \quad (70)$$

where, $\Psi_n(\Delta f, \theta)$ is a time delay term derived from,

$$\Psi_n(\Delta f, \theta) = F[w_n(\Delta f, \theta), 2\pi f_o]. \quad (71)$$

Then by using the adaptive steering weights $w_n(\Delta f, \theta)$, that are provided by Eq. (70), the adaptive beams are formed as shown by Eq. (58). Figure 10 shows the realization of the STMV beamformer and provides a schematic representation of the basic processing steps that include:

1. time series segmentation, overlap and FFT, shown by the group of blocks at the top-left part of the schematic diagram.
2. Formation of steered covariance matrix, [Eqs. (64), (67)] shown by the two blocks at the bottom left hand side of Figure 10.

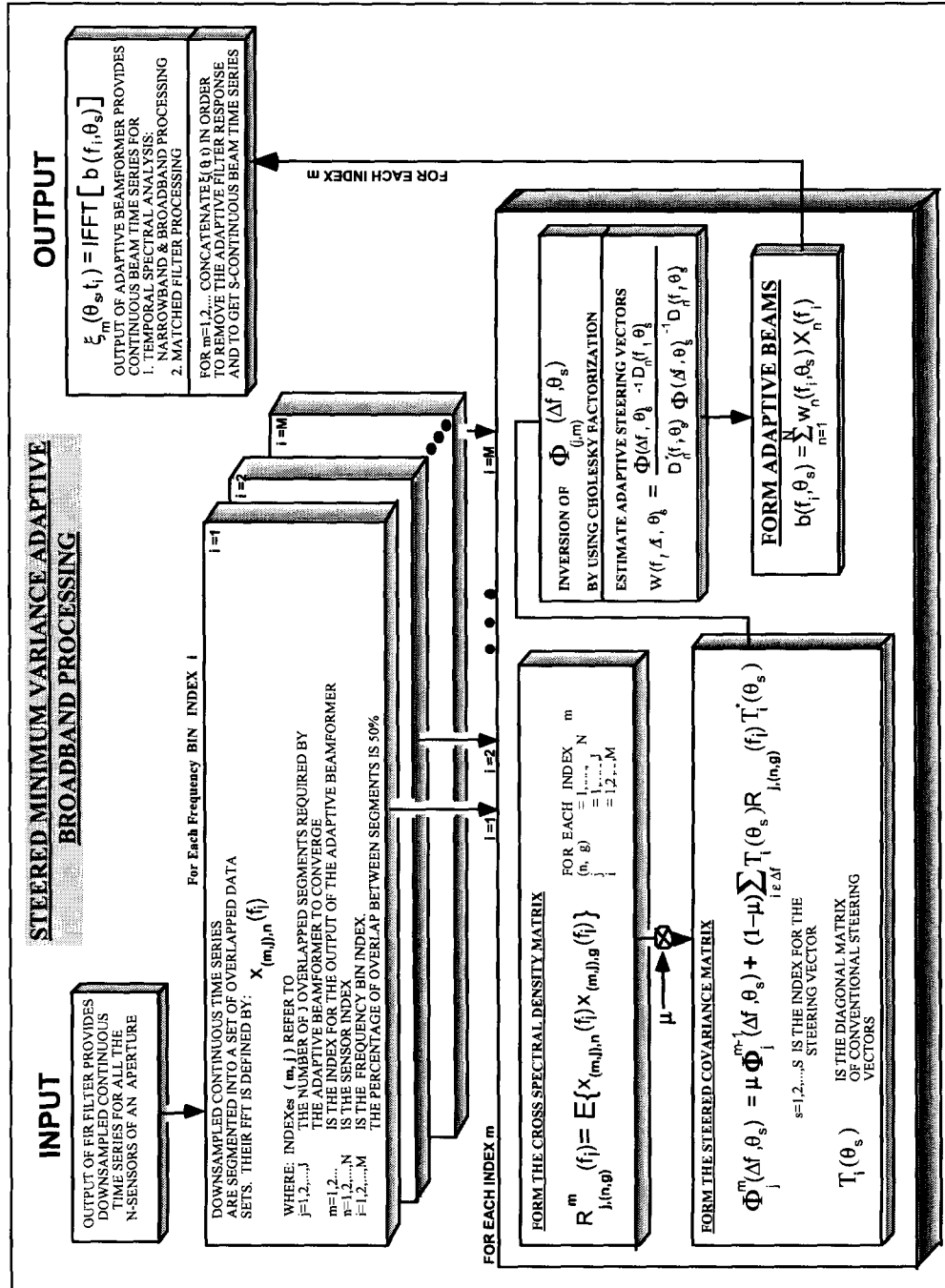


Figure 10. Realization of the steered covariance adaptive beamformer.

3. Inversion of covariance matrix using Cholesky factorization, estimation of adaptive steering vectors and formation of adaptive beams in frequency domain, presented by the middle and bottom blocks at the right hand side of Figure 10; and finally
4. formation of adaptive beams in time domain through IFFT, discarding of overlap and concatenation of segments to form continuous beam time series, which is shown by the top right hand side block.

The various indexes in Figure 10 provide details for the implementation of the STMV processing flow in a generic computing architecture. The same figure indicates that estimates of the Steered Covariance Matrix (STCM) is based on an exponentially weighted time average of the current and previous STCM, which is discussed in the next section.

5. Implementation Considerations

The conventional and adaptive steering vectors for steering angles θ_s, ϕ_s discussed in Section 3 are integrated in a frequency domain beamforming scheme, which is expressed by Eqs. (25), (28), (34) and (58). The beam time series are formed by Eq. (32). Thus, the frequency domain adaptive and conventional outputs are made equivalent to the fast Fourier transform (FFT) of the time domain beamforming outputs with proper selection of beamforming weights and careful data partitioning. This equivalence corresponds to implementing FIR filters via circular convolution [40-42].

Matrix inversion is another major implementation issue for the adaptive schemes discussed in this report. Standard numerical methods for solving systems of linear equations can be applied to solve for the adaptive weights. The range of possible algorithms includes:

Cholesky factorization of the covariance matrix $R(f_i)$, [17,29]. This allows the linear system to be solved by backsubstitution in terms of the received data vector. Note that there is no requirement to estimate the sample covariance matrix and that there is a continuous updating of an existing Cholesky factorization.

QR decomposition [19,21,24] of the received vector $\bar{X}(f_i)$, that includes the conversion of a matrix to upper triangular form via rotations. The QR decomposition method has better stability than the Cholesky factorization algorithm, but it requires twice as much computational efforts than the Cholesky approach.

SVD (Singular Value Decomposition) method [19,21,24],. This is the most stable factorization technique. It requires, however, three times more computational requirements than the QR decomposition method.

In this implementation study we have applied the Cholesky factorization and the QR decomposition techniques in order to get solutions for the adaptive weights. Our experience suggests that there are no noticeable differences in performance between the above two methods [1].

The main consideration, however, for implementing adaptive schemes in real time systems are associated with the requirements derived from Eqs. (57), (68), which require knowledge of second order statistics for the noise field. Although these statistics are usually not known, they can be estimated from the received data [17,18,23] by averaging a large number of independent samples of the covariance matrixes $R(f_i)$ or by allowing the iteration process of the adaptive GSC schemes to converge [1,37]. Thus, if K is the effective number of statistically independent samples of $R(f_i)$, then the variance on the adaptive beam output power estimator detection statistic is inversely proportional to $(K-N+1)$, [17,18,22], where N is the number of sensors. Theoretical suggestions [23] and our empirical observations suggest that K needs to be three to four times the size of N in order to get coherent beam time series at the output of the above adaptive schemes. In other words, for arrays with a

large number of sensors, the implementation of adaptive schemes as statistically optimum beamformers would require the averaging of a very large number of independent samples of $R(f_i)$ in order to derive an unbiased estimate of the adaptive weights [23]. In practice this is the most serious problem associated with the implementation of adaptive beamformers in real time systems.

Owsley [17,29] has addressed this problem with two important contributions. His first contribution is associated with the estimation procedure of $R(f_i)$. His argument is that in practice, the covariance matrix cannot be estimated exactly by time averaging because the received signal vector $\bar{X}(f_i)$ is never truly stationary and/or ergodic. As a result, the available averaging time is limited. Accordingly, one approach to the time-varying adaptive estimation of $R(f_i)$ at time t_k is to compute the exponentially time averaged estimator (geometric forgetting algorithm) at time t_k :

$$R^{t_k}(f_i) = \mu R^{t_{k-1}}(f_i) + (1 - \mu) \bar{X}(f_i) \bar{X}^*(f_i) \quad (72)$$

where μ is a smoothing factor ($0 < \mu < 1$) that implements the exponentially weighted time averaging operation. The same principle has also been applied in the GSC scheme [1,37]. Use of this type of exponential window to update the covariance matrix is a very important factor in the implementation of adaptive algorithms in real time systems.

Owsley's [29] second contribution deals with the dynamics of the data statistics during the convergence period of the adaptation process. As mentioned above, the implementation of an adaptive beamformer with a large number of adaptive weights in a large array sonar system, requires very long convergence periods that will eliminate the dynamical characteristics of the adaptive beamformer to detect the time varying characteristics of a received signal of interest. A natural way to avoid temporal stationarity limitations is to reduce the number of adaptive weights requirements. Owsley's [29] sub-aperture configuration for line array adaptive beamforming reduces significantly the number of degrees of freedom of an adaptation process. His concept has been applied to line arrays, as discussed in References [1,37]. However, extension of the sub-aperture line array concept for multi-dimensional arrays is not a trivial task. In the following sections, the sub-aperture concept is generalized for circular, cylindrical, planar and spherical arrays.

5.1 Signal Cancellation Effects of the Adaptive Algorithms

Testing of the adaptive algorithms of this study for signal cancellation effects was carried out with simulations that included two narrowband signals arriving from 64 degrees and 69 degrees [1,37]. The simulations included full aperture and sub-aperture (SA) implementation, which is discussed in the next section. All of the parameters of the signals were set to the same values for all the beamformers, conventional, GSC/NLMS, GSC-SA/NLMS, STMV and STMV-SA. Details about the above simulated signal cancellation effects can be found in Reference [1,37]. In the narrowband outputs of the conventional

beamformer, the signals appear at the frequency and beam at which they were expected. As anticipated, however, the sidelobes are visible in a number of other beams. The gram outputs [1,37] of the GSC/STMV algorithm indicated that there is signal cancellation.

In each case, the algorithm failed to detect either of the two narrowband signals. This suggests that there is a shortcoming in the GSC/NLMS algorithm, when there is strong correlation between two signals arrivals received by the line array.

The narrowband outputs of the GSC-SA/NLMS algorithm showed that in this case the signal cancellation effects have been minimized and the two signals were detected only at the expected two beams with complete cancellation of the sidelobe structure. For the STMV beamformer, the grams indicated a strong sidelobe structure in many other beams. However, the STMV-SA beamformer successfully suppresses the sidelobe structure that was present in the case of the STMV beamformer. From all these simulations [37], it was obvious that the STMV-SA beamformer, as a narrowband beamformer, is not as robust for narrowband applications as the GSC-SA/NLMS.

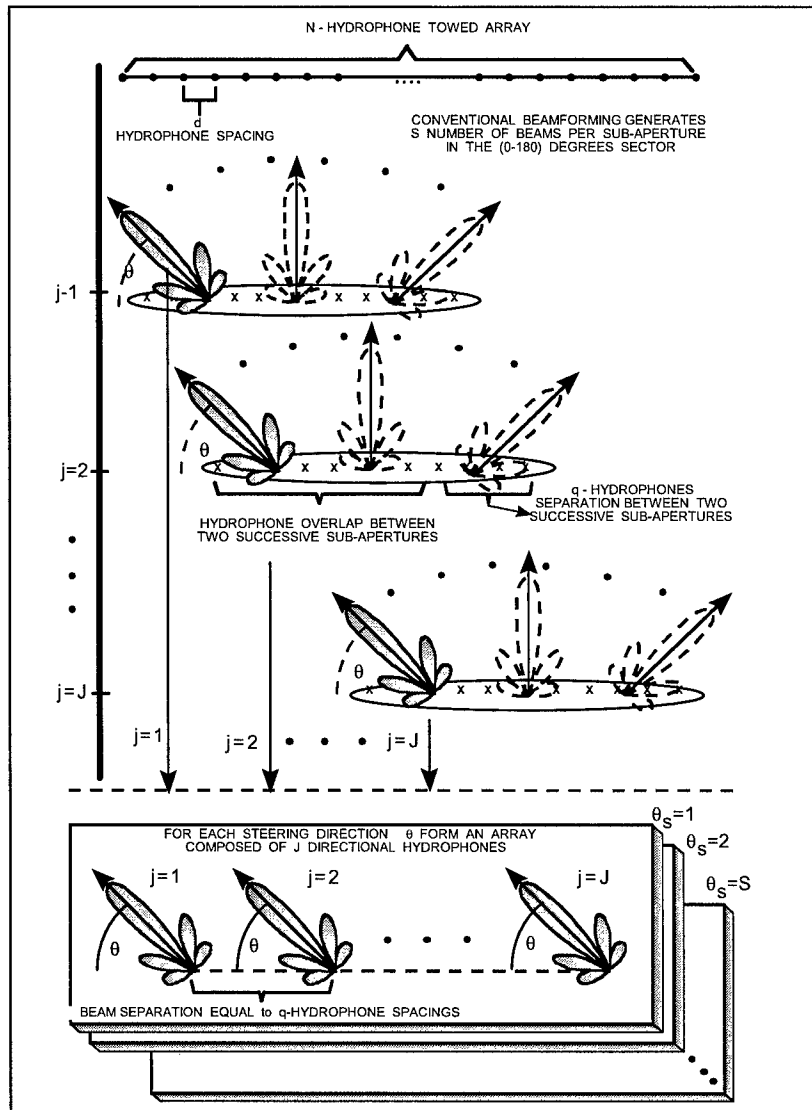


Figure 11. Concept of adaptive sub-aperture structure for line arrays. Schematic diagram shows the steps: (1) formation of J sub-apertures, (2) for each sub-aperture formation of S conventional beams, (3) for a given beam direction, θ formation of line arrays that consist of J number of directional sensors (beams).

5.2 Generic Multi-Dimensional Sub-Aperture Structure for Adaptive Schemes

The decomposition of the 2-D and 3-D beamformer into sets of line and/or circular array beamformers, which has been discussed in Section 3.2, provides a first-stage reduction of the numbers of degrees of freedom for an adaptation process. Furthermore, the sub-aperture configuration is considered in this study as a second stage reduction of the number of degrees of freedom for an adaptive beamformer. Then, the implementation effort for adaptive schemes in multi-dimensional arrays is reduced to implementing adaptive processes

in line and circular arrays. Thus, a multi-dimensional adaptive beamformer can now be divided into two coherent modular steps which lead to efficient system-oriented implementations.

5.2.1 Sub-Aperture Configuration for Line Arrays

For a line array, a sub-aperture configuration includes a large percentage overlap between contiguous sub-apertures. More specifically, a line array is divided into a number of sub-arrays that overlap, as shown in Figure 11. These sub-arrays are beamformed using the conventional approach; and this is the first stage of beamforming.

Then, we form a number of sets of beams with each set consisting of beams that are steered at the same direction but each one of them generated by a different sub-array. A set of beams of this kind is equivalent to a line array that consists of directional sensors steered at the same direction, with sensor spacing equal to the space separation between two contiguous sub-arrays and with the number of sensors equal to the number of sub-arrays. The second stage of beamforming implements an adaptive scheme on the above set of beams, as illustrated in Figure 11.

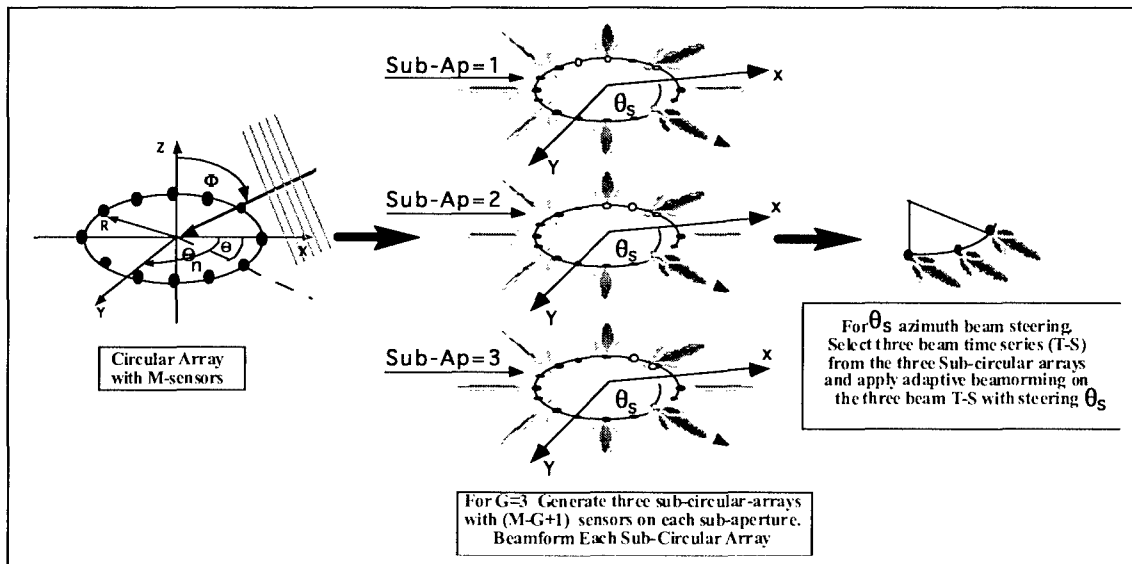


Figure 12. Concept of adaptive sub-aperture structure for circular arrays, which is similar to that for line arrays shown in Figure 11.

5.2.2 Sub-Aperture Configuration for Circular Array

Consider a circular array with M -sensors as shown in Figure 12. The first circular sub-aperture consists of the first $M-G+1$ sensors with $n=1, 2, \dots, M-$

$G+1$, where n is the sensor index and G is the number of sub-apertures. The second circular sub-aperture array consists of $M-G+1$ sensors with $n=2,3,\dots,M-G+2$. The sub-aperture formation goes on until the last sub-aperture consists of $M-G+1$ sensors with $n=G,G+1,\dots,M$. In the first stage, each circular sub-aperture is beamformed as discussed in Section 3.1.2 and this first stage of beamforming generates G sets of beams.

As in the previous section, we form a number of sets of beams with each set consisting of beams that are steered at the same direction but each one of them generated by a different sub-array. For $G < 5$, a set of beams of this kind can be treated approximately as a line array that consists of directional sensors steered at the same direction, with sensor spacing equal to the space separation between two contiguous sub-arrays and with the number of sensors equal to the number of sub-arrays. The second stage of beamforming implements an adaptive scheme on the set of beams, as illustrated in Figure 12, for $G=3$.

5.2.3 Sub-Aperture Configuration for Cylindrical Array

Consider the cylindrical array shown in Figure 13 with the number of sensors $\mathbf{K} = NM$, where N is the number of circular rings and M is the number of sensors on each ring. Let n be the ring index, m be the sensor index for each ring and G be the number of sub-apertures. The formation of sub-apertures is as follows:

The first sub-aperture consists of the first $(N - G + 1)$ rings, where $n = 1, 2, \dots, N-G+1$. In each ring we select the first set of $(M - G + 1)$ sensors, where $m = 1, 2, \dots, M-G+1$. However, each ring has M sensors, but only $(M-G+1)$ sensors are used to form the sub-aperture. These sensors form a cylindrical array cell, as shown in the upper right hand side corner of Fig. 13.

In other words, the sub-aperture includes the sensors of the full cylindrical array except for $G-1$ sensors from $G-1$ rings, which are denoted by small circles in Figure 13, that have been excluded in order to form the sub-aperture. Next, the generic decomposition concept of the conventional cylindrical array beamformer, presented in Section 3.2.1, is applied to the above sub-aperture cylindrical array cell. For a given pair of azimuth and elevation steering angles $\{\theta_s, \phi_s\}$, the output of the generic conventional multi-dimensional sub-aperture beamformer provides beam time series, $b_{g=1}(t_i, \theta_s, \phi_s)$, where the subscript $g=1$ is the sub-aperture index.

The second sub-aperture consists of the next set of $(N - G + 1)$ rings, where $n = 2, \dots, N-G+2$. In each ring we select the next set of $(M - G + 1)$ sensors, where $m = 2, \dots, M-$

$G+2$. However, each ring has M sensors, but only $(M-G+1)$ sensors are used to form the sub-aperture. These sensors form the second sub-aperture cylindrical array cell.

Again, the generic decomposition concept of the conventional cylindrical array beamformer, presented in Section 3.2.1, is applied to the above sub-aperture cylindrical array cell. For a given pair of azimuth and elevation steering angles $\{\theta_s, \phi_s\}$, the output of the generic conventional multi-dimensional sub-aperture beamformer provides beam time series, $b_{g=2}(t_i, \theta_s, \phi_s)$ with sub-aperture index $g=2$.

The proposed sub-aperture formation continues until the last sub-aperture which consists of a set of $(N - G + 1)$ rings, where $n = G, G+1, \dots, N$. In each ring we select the last set of $(M - G + 1)$ sensors, where $m = G, G+1, \dots, M$. Please note also that each ring has M sensors, but only $(M-G+1)$ sensors are used to form the sub-aperture.

As before, the generic decomposition concept of the conventional cylindrical array beamformer is applied to the last sub-aperture cylindrical array cell. For a given pair of azimuth and elevation steering angles $\{\theta_s, \phi_s\}$, the output of the generic conventional multi-dimensional sub-aperture beamformer would provide beam time series, $b_{g=G}(t_i, \theta_s, \phi_s)$ with sub-aperture index $g=G$.

As in Section 5.2.2, we form a number of sets of beams with each set consisting of beams that are steered at the same direction but each one of them generated by a different sub-aperture cylindrical array cell. For $G < 5$, a set of beams of this kind can be treated approximately as a line array that consists of directional sensors steered at the same direction, with sensor spacing equal to the space separation between two contiguous sub-aperture cylindrical array cells and with the number of sensors equal to the number of sub-arrays. Then, the second stage of beamforming implements an adaptive scheme on the above set of beams, as illustrated in Figure 13.

For the particular case, shown in Figure 13, the second stage of beamforming implements an adaptive beamformer on a line array that consists of the $G=3$ beam time series $b_g(t_i, \theta_s, \phi_s), g=1, 2, \dots, G$. Thus, for a given pair of azimuth and elevation steering angles $\{\theta_s, \phi_s\}$, the cylindrical adaptive beamforming process is reduced to an adaptive line array beamformer that includes as input only three beam time series $b_g(t_i, \theta_s, \phi_s), g=1, 2, 3$ with spacing $\delta = \left[(R2\pi / M)^2 + \delta_z^2 \right]^{1/2}$, which is the spacing between two contiguous sub-aperture cylindrical cells, where $(R2\pi / M)$ is the sensor spacing in each ring and δ_z is the distance between each ring along z-axis of

the cylindrical array. The output of the adaptive beamformer provides one or more adaptive beam time series with steering centered on the pair of azimuth and elevation steering angles $\{\theta_s, \phi_s\}$.

As expected, the adaptation process in this case will have near-instantaneous convergence because of the very small number of degrees of freedom. Furthermore, because of the generic characteristics, the proposed 3-D sub-aperture adaptive beamforming concept may include a wide variety of adaptive techniques such as MVDR, GSC and STMV that have been discussed in References [1,37].

5.2.4 Sub-Aperture Configuration for Planar and Spherical Arrays

The sub-aperture adaptive beamforming concepts for planar and spherical arrays are very similar to that of the cylindrical array. In particular, for planar arrays, the formation of sub-apertures is based on the sub-aperture concept of line arrays that has been discussed in Section 5.2.1. The different steps of sub-aperture formation for planar arrays as well as the implementation of adaptive schemes on the G beam time series $b_g(t_i, \theta_s, \phi_s)$, $g=1,2,\dots,G$, that are provided by the G sub-apertures of the planar array, are similar with those in Figure 12 by considering the composition process for planar arrays shown in Figure 7. Similarly, the sub-aperture adaptive concept for spherical arrays is based on the sub-aperture concept of circular arrays, that has been discussed in Section 5.2.2.

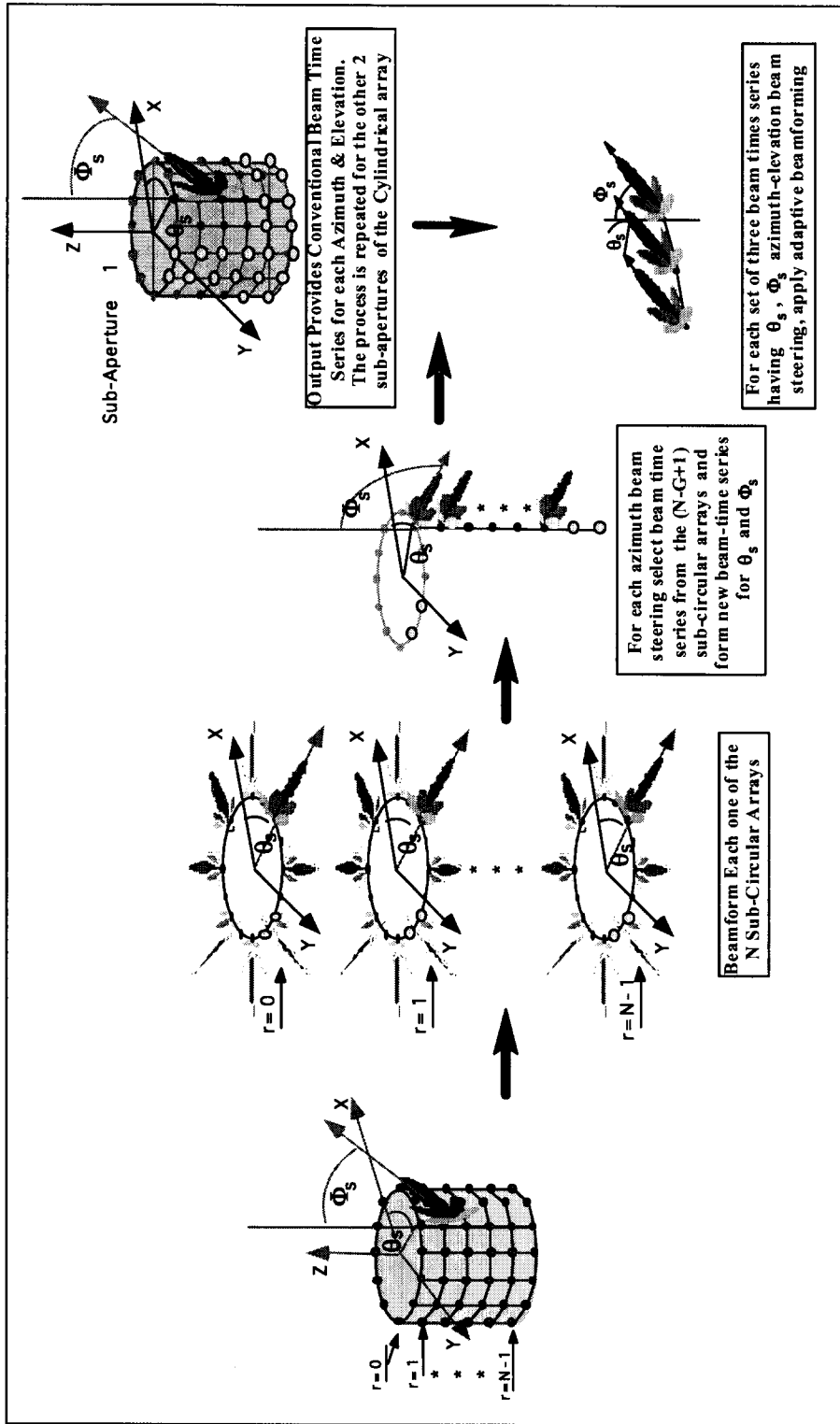


Figure 13. Geometric representation of the concept of adaptive sub-aperture structure for cylindrical arrays. In this example the number of sub-apertures was $G=3$. The $N = NM$ sensor cylindrical array beamformer consists of N circular arrays with M being the number of sensors in each circular array. Then, the sub-aperture adaptive structure for cylindrical arrays is reduced to the steps of adaptive sub-aperture structures for circular and line arrays as defined in the schematics of Fig. 11 & 12.

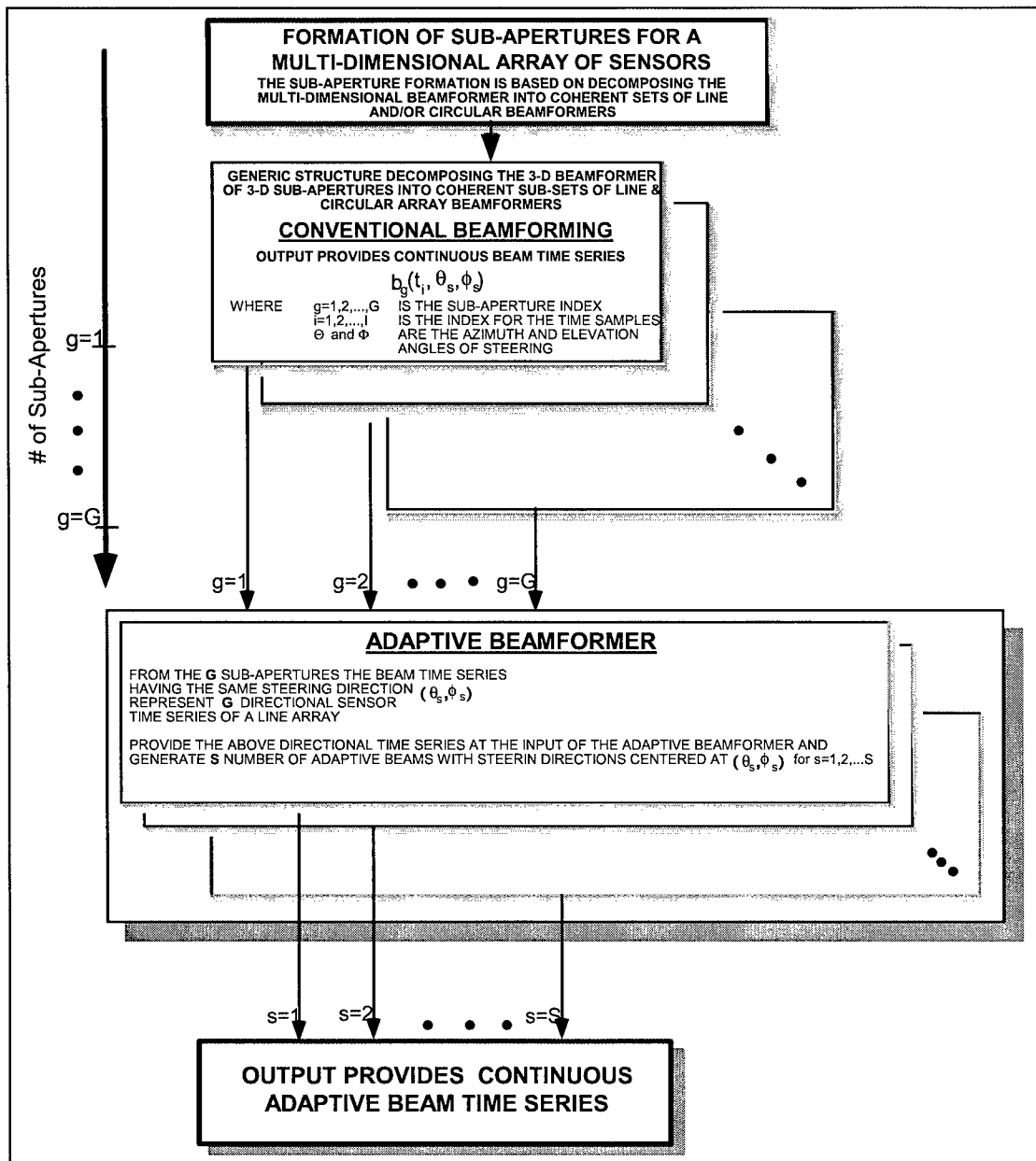


Figure 14. Signal processing of generic structure decomposing the 3-D beamformer for cylindrical arrays of sensors into coherent sub-sets of line and circular array beamformers.

5.3 Signal Processing Flow of a 3-D Generic Sub-Aperture Structure

As it was stated before, the discussion in this report has been devoted in designing a generic sub-aperture beamforming structure that will decompose the computationally intensive multi-dimensional beamforming process into coherent sub-sets of line and/or circular sub-aperture array beamformers for ultrasound, radar and integrated active-passive sonar systems. In a sense, the proposed generic processing structure is an extension of a previous effort discussed in Reference [1].

The previous study [1] included the design of a generic beamforming structure that allows the implementation of adaptive, synthetic aperture and high-resolution temporal and spatial spectral analysis techniques in integrated active-passive line-array SONARs. Figure 11 in Reference [1] shows the configuration of the signal processing flow of an equivalent generic structure for line arrays that allows the implementation of Finite Impulse Response (FIR) filters, conventional, adaptive and synthetic aperture beamformers [1,40,41,42].

Shown in Figure 14 is the proposed configuration of the signal processing flow that includes the implementation of line and circular array beamformers as Finite Impulse Response (FIR) filters [40,41,42]. The processing flow is for 3-D cylindrical arrays. The reconfiguration of the different processing blocks in Figure 14 allows the application of the proposed configuration to a variety of ultrasound systems with planar, cylindrical or spherical arrays of sensors.

As discussed at the beginning of this section, the output of the beamforming processing block in Figure 14 provides continuous beam time series for ultrasound image reconstruction. Then the beam time series are provided at the input of a matched filter for Doppler estimation. This modular structure in the signal processing flow is a very essential processing arrangement in order to allow for the integration of a great variety of processing schemes such as the ones considered in this report. The details of the proposed generic processing flow, as shown in Figure 14, are very briefly the following:

The first processing block includes the formation of sub-apertures as discussed in Section 5.2. Then, the sensor time series from each sub-aperture are beamformed by the generic multi-dimensional beamforming structure that has been introduced in Section 3. Thus, for a given pair of azimuth and elevation steering angles $\{\theta_s, \phi_s\}$, the output of the generic conventional multi-dimensional beamformer would provide G beam time series, $b_g(t_i, \theta_s, \phi_s)$, $g=1,2,\dots,G$. The second stage of beamforming includes the implementation of an adaptive beamformer as discussed in Section 4.2.

6. Concept Demonstration: Simulations & Experimental Results

Concept demonstration of the proposed ultrasonic imaging technology has been carried out with a custom made ultrasound system that has been acquired by DRDC to fulfil the project's development requirements. The system configuration is depicted in Figure 15. The main components include:

- A Line array of 32-transducers for ultrasound imaging applications.
- A general purpose Ultrasound Imaging system for medical diagnostic applications with CPU components:
 - Beamformer, Data manager and Display functionality
- A custom-made A/DC (12-bit, 45MHz sampling frequency per channel),
- a signal conditioning unit and a CPU computer workstation that includes implementation of the advanced beamforming structure discussed in the previous sections.

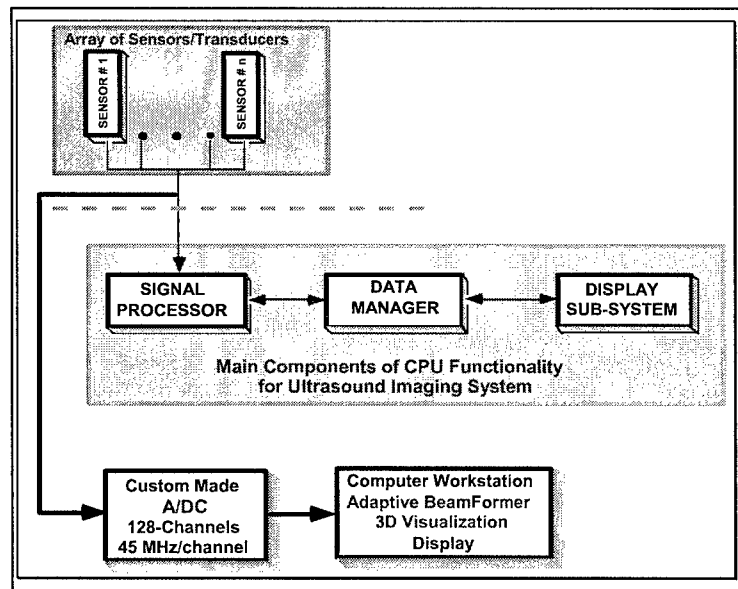


Figure 15. Special purpose ultrasound imaging system to assess image resolution improvements of the adaptive beamformers.

Thus, the sensor time series (RF data) provided by the line array (probe) of the general purpose ultrasound system of Figure 14, were processed with the advanced beamforming

structure of the present investigation; and for comparison the resulting reconstructed images were compared with the corresponding images of the general purpose ultrasound system. Figure 16 presents the actual custom made ultrasound system that is depicted schematically also in Figure 15.

In summary, the basic steps of the concept demonstration process included the following:

- The sensor time series (RF data) that were provided by the line array of the ultrasound 32-transducers were processed by the general purpose ultrasound system providing as an output a complete image of the phantom under investigation.
- The same RF data were processed also by the computer workstation (CPU) including the adaptive beamformers (shown in Figure 15).

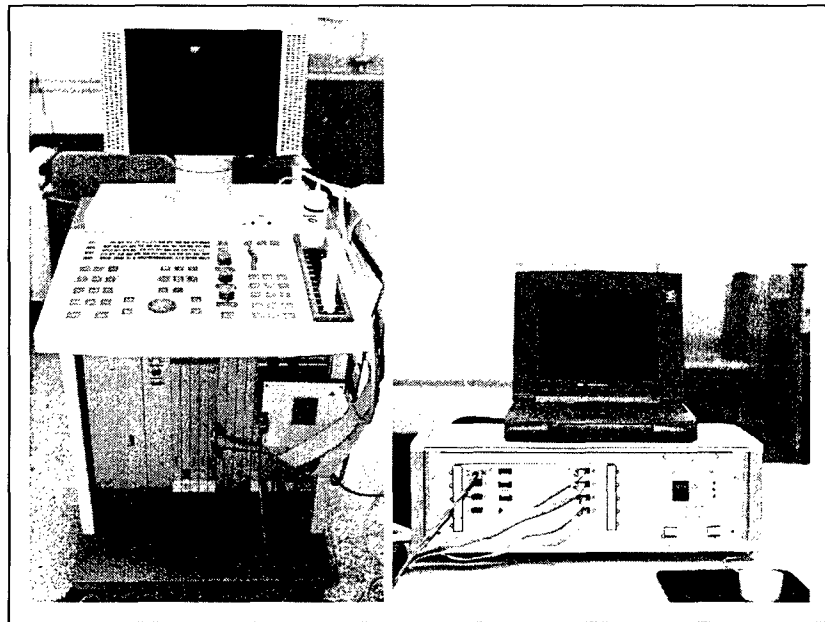


Figure 16. Left picture shows the general purpose ultrasound system. Right picture shows the data acquisition system providing digitization of the RF data from the probe of the system at the left.

6.1 Computing Architecture

The implementation of this investigation's non-conventional processing schemes in ultrasound systems is a non-trivial issue. In addition to the selection of the appropriate algorithms, success is heavily dependent on the availability of suitable computing architectures.

Past attempts to implement matrix-based signal processing methods, such as adaptive beamformers reported in this report, were based on the development of systolic array

hardware because systolic arrays allow large amounts of parallel computation to be performed efficiently since communications occur locally. None of these ideas are new. Unfortunately systolic arrays have been much less successful in practice than in theory. The fixed size problem for which it makes sense to build a specific array is rare. Systolic arrays big enough for real problems cannot fit on one board, much less one chip, and interconnects have problems. A 2-D systolic array implementation will be even more difficult. So, any new computing architecture development should provide high throughput for vector as well as matrix based processing schemes.

A fundamental question, however, that must be addressed at this point is whether it is worthwhile to attempt to develop a system architecture that can compete with a multiprocessor using stock microprocessors. Although recent microprocessors use advanced architectures, improvements of their performance includes a heavy cost in design complexity, which grows dramatically with the number of instructions that can be executed concurrently. Moreover, the recent microprocessors, that claim high performance for peak MFLOP rates, have their net throughput usually much lower and their memory architectures are targeted towards general purpose code.

The above issues establish the requirement for dedicated architectures, such as in the area of operational sonar and radar systems. Sonar applications are computationally intensive [1, 60], and they require high throughput on large data sets. However, the experience gained from sonar computing architecture developments that were based on RISC processors [1], suggested that a cost effective approach in that direction is to develop a multi-CPU computing architecture that will be based on the rapidly evolving microprocessor technology of the CPUs of the power-PCs, such as the family of Pentium CPUs.

Other advanced computing architectures that can cover the throughput requirements of computationally intensive signal processing applications, such as those discussed in this manuscript, have been developed by Mercury Computer Systems. Based on the experience of the authors of this report, the suggestion is that implementation efforts of advanced signal processing concepts should be directed more on the development of generic signal processing structures as in Figure 14, rather than in developing very expensive computing architectures. Moreover, the signal processing flow of advanced processing schemes that include both scalar and vector operations should be very well defined in order to address practical implementation issues. When the signal processing flow is well established, such as in Figure 14, then distribution of the signal processing flow in a number of parallel CPU's of the computing architecture, will be straightforward.

In the following sections, we address the practical system implementation issues by describing the current effort of developing a real 3D Ultrasound system deploying a planar array to address the requirements of the Canadian Forces in non-invasive portable diagnostic devices deployable in operational fields. The same system development of the real 3D ultrasound system may be integrated with the final system results of the European Commission project "Minimally Invasive Tumour Therapy 3D Ultrasound Guided" (MITTUG).

6.1.1 Experimental Platform

To address the computing architecture requirements of this investigation we used a cluster of 16 2-way Pentium III nodes interconnected with a Myrinet network. Myrinet is a low-latency, high-bandwidth, point-to-point system area network (SAN), used widely for clusters of workstations and PCs. By allowing users to directly access the network, without operating system intervention, Myrinet and other SANs dramatically reduce latencies compared to traditional TCP/IP based local area networks. Moreover, to further reduce latencies in SANs, direct memory operations are usually supported; reads and writes to remote memory are performed without remote processor intervention. The exact system configuration is summarised in Table 1 and for more details the reader is referred to [74]. The nodes in the system are connected with a Myrinet interconnection network. Each network interface in our system has a 33 MHz programmable processor and connects the node to the network with two unidirectional links of 160 MByte/s peak bandwidth each. Actual node-to-network bandwidth is usually constrained by the 133 MBytes/s I/O bus on which the NIC sits. All system nodes are connected with a 16-port full crossbar Myrinet switch.

The communication layer we use is the Message Passing Interface (MPI) on top of the SCore system [75]. SCore is a high-performance parallel programming environment for workstation and PC clusters. SCore relies on the PMv2 [76] low-level communication layer. The MPI implementation we use is a port of the MPICH library for the SCore system. For more details about the bandwidth and latency of the basic, un-contended MPI_Send and MPI_Recv operations, the reader is referred to [74].

Table 1. Cluster node configuration

PROCESSORS	2 x Intel Pentium III, 800 MHz
Cache	Column 2 subheading
Memory	32K (L1), 512K (L2)
OS	512MB SDRAM
PCI buses	RedHat Linux Kernel 2.2.16-3smp
NIC	Myricom M3M-PCI64M
Communication library	MPICH/Score 4.0

6.1.2 Algorithm Implementation

Implementations of the signal processing structures outlined in Sections 3 to 5 assumes that input data is delivered directly from the acquisition unit to the

memories of the nodes. This is a realistic assumption, since, in the actual prototype the building of each node will be equipped with a PCI-based data acquisition card that will read part of the data from the sensor array. Next, we present the sequential and parallel implementations of the 3D beamforming algorithm.

6.1.2.1 Sequential Implementation

Our sequential algorithm for performing the computation outlined in Sections 3 to 5 and outlined in Figure 14, consists of the following phases: read input samples, compute FFTs, filter results, perform column steering, reorganize data in memory, perform row steering, perform inverse FFTs, and, finally, output to display.

In addition to dividing the scanned volume to multiple focal zones and using multiple beams to scan it, beamforming algorithms divide the 2D surface to be scanned in multiple tiles. If we view the 2D surface as an array of points, we can divide the rows and columns in ROW, COL groups forming ROW x COL tiles. Each tile is scanned by the full planar sensor array. Thus, channels-per-column (CHC) and channels-per-row (CHR) represent the number of sensors in each dimension of the planar array. Every full snapshot (that generates a single full 3D frame of the scanned volume) requires scanning all tiles and focal zones, as illustrated in Figure 17. For real-time processing we would require at least 10 frames (full snapshots) per second and ideally 20 to 30.

To re-create the depth information the algorithm processes the data based on a number of focal zones (NZONES). Each focal zone is of constant width (depth) which depends on the depth of the volume to be scanned and the number of focal zones. The volume depth is usually constant and defined by the type of objects the ultrasound will scan. For instance, different human organs require different scan depths. In this work we use a fixed maximum focal depth of 16 cm and we vary only the number of focal zones.

For each scanned point of the input volume the program reads the time series data from the corresponding sensor (that may scan multiple points) and stores it in a buffer in host memory. Each sample is 32 bits and is represented as a single precision floating point number.

The number of samples that need to be processed is dictated by the depth of each focal zone. The probing signal used to scan the object reaches different depths of the scanned volume with different delays. The sampling rate used to digitize the received signal dictates the minimum number of samples (and the

minimum FFT size) required to reconstruct depth information. For example, assuming a sampling frequency of $F_s = 30$ MHz, the number of samples needed to reconstruct 20 cm depth can be computed by,

$$N = \frac{2dF_s}{c} = \frac{2 \times 0.2 \times 30 \times 10^6}{1540} = 7792$$

where N is the number of read in samples, c is the speed of sound in meters per second, d is the depth of the reconstruct area in meters. The factor of two is needed to account for the round trip time. Thus, in this example the ultrasound system (acquisition unit) needs to provide the beamformer with 7792 samples for each of the sensor time series of the ultrasound probe. Using more than the minimum number of samples can improve the array gain and result in better quality imaging. However, reading in more samples results not only in more processing but also in longer acquisition times and higher storage requirements. To counter this problem, in our experiments we set the number of acquired samples to 8K and during the processing we vary the size of the FFT operations.

After the time samples are read and converted to frequency domain, a filtering phase is used to reduce the amount of information passed to later stages. The information embedded in the received signals necessary for reconstructing a particular depth region is localized in a certain bandwidth. Using only the relevant frequency components further reduces computational time. Thus, the FFT output samples are filtered (with a Finite Impulse Response (FIR) filter [1]) to exclude unnecessary information and the related processing. The bandwidth depends on the focal depth and the center frequency of the ultrasound pulses. Lower frequency signals usually have better penetration into deeper regions, whereas, higher frequency signals produce sharper beam resolutions. However, center frequencies are usually fixed for each depth. Thus, in this work we use 2 MHz as the center frequency for an input volume with maximum depth of 16 cm. In the applications we are interested in, most objects (human organs) would fall within this range. Given this center frequency the bandwidth of the filter can vary in the range *0.5-4.0 MHz*.

After filtering, the beamformer performs the steering operations and finally samples are converted back to the time domain for displaying. Based on the beam-steering equations (37), the steering of beams along azimuth and elevation, shown in Figure 17, separately using the pre-calculated steering vector to align the

time delay of the signals arriving in different sensors and IFFT transforms the signal from the frequency to the time domain.

6.1.2.2 Optimization

To gain confidence that we start from an efficient sequential implementation, before proceeding with parallelization, we perform a number of measurements to fine tune several aspects of our sequential implementation.

First, we explore various FFT implementations, both our own and those publicly available. We find that, for the processors we use, the most efficient implementation is FFTW that has been developed at MIT, a C library for computing discrete Fourier transforms, which is free for non-commercial use under the GNU General Public License (GPL) [78]. This also minimizes space requirements since the output of this function is a half-complex array that consists of only half the DFT amplitudes; The negative-frequency amplitudes for real data are the complex conjugates of the positive-frequency amplitudes. The side effect of this is that we need to re-organize the output to a common, full-complex array format after the FFT and revert to the half-complex array before the IFFT. Also, FFTW computes an un-normalized transform for the input signal $\text{IFFT}(\text{FFT}(x)) = N \times X$ for size N transforms. Thus, a division by N is needed for each element of the array after the final IFFT.

Second, we experiment with multiple ways of performing the steering and the related dot product operations. We find that the best results are obtained by using the function from the Intel Math Kernel Library (MKL) [78] to compute the necessary dot products and to perform the steering. MKL is optimized for the Pentium family of processors and makes effective use of the MMX (Matrix Multiplication Extensions), SSE (Streaming SIMD Extensions), and similar instructions.

Third, we tune loop ordering and the layout of multidimensional array data structures to improve memory access behaviour and to reduce cache misses.

The overall effect of these optimization steps is a reduction of the overall execution time of the sequential implementation by a factor of about 10. It is a surprising result that hand-tuning can be so effective with all compiler optimizations turned on. However, since in this work we are more interested in the behaviour of the parallel version we omit these results due to space limitations.

6.1.2.3 *Parallel Implementation*

The parallel version of the beamforming algorithm follows closely the structure of the sequential implementation. We see that the data read from each sensor is processed independently until steering. Then, during the steering phase, the beams across the azimuth and elevation directions are independent. Therefore, we choose to divide the computation in two phases. The first phase includes all processing until after the column-steering phase. The second phase includes the rest of the processing, starting at the row-steering phase. Between the two phases, we need to re-organize the data in memory by performing a matrix transpose, which results in an all-to-all communication pattern.

The first phase of the computation for each frame is decomposed in tasks based on the data generated by each sensor. Thus, there is as many tasks as sensors 32×32 of the planar array, shown in Figure 17, which is sufficient for systems with large numbers of processors. The tasks for the second phase are determined by the processing associated with each beam. We use the processing related to a single beam as the basic task and we decompose the second phase to (azimuth-BEAMS) \times (elevation-BEAMS) tasks. For instance, with 8 beams in each direction, there are 64 coarse grain tasks. We expect that for all practical applications, at least 8×8 beams will be necessary and thus we do not consider cases where the number of processors is larger than the total number of beams.

We experiment with two implementations of the parallel algorithm. The first implementation uses dedicated nodes for each phase. However, we find that balancing the number of nodes between the two phases of the computation depends on a large number of parameters. Thus, we provide a second, symmetric, implementation as well, where all nodes in the system perform the same type of processing. Although, the first, dataflow approach has certain advantages in reducing task management costs, we find that the second approach is more flexible and results in better load balancing. Thus, for the rest of this work we only use our symmetric implementation.

6.2 Details of a Real 3D Ultrasound System Deploying a Planar Array

6.2.1 Requirements

DRDC Toronto's medical imaging project investigations include the development of Ultrasound Diagnostic Imaging Systems with adaptive and synthetic aperture beamformers for improved image resolution capabilities to allow for tissue identification. The system will be capable of providing:

2D images by deploying line or curvilinear arrays,

3D volumetric images by deploying planar arrays.

The main R&D activities associated with this investigation include:

1. Planar Array with

32x32 –element receiving component

12x12-element transmitting array

The corresponding data acquisition system, as defined in Figure 18.

2. Development of a PC-based Computing Architecture, defined in Figure 18, to provide real-time processing of raw data provided by the data acquisition system defined above. The bandwidth requirements for the computing architecture are defined in Section 6.2.3 of this report.
3. Mapping and Implementation of the synthetic aperture and adaptive beamformers in the dedicated computing architecture defined above.
4. Development of the synthetic aperture and adaptive beamforming structure for the 2D and 3D ultrasound system of this investigation.
5. Development of 3D, 4D, 6D and 7D image visualization tools for the output beam times series of the processing structure, defined in the above activity (4). The visualization tools have been developed by Prof. Sakas at Fraunhofer (National Research Institute, Darmstadt, Germany) as part of our group's involvement in the European Canadian collaborative projects New-Roentgen, MITTUG, ADUMS and MRI-MARCB [79-82].

6. System integration of R&D efforts of the above activities, (1), (2), (3) and (4).

In the following sections, the system characteristics are defined in terms of the acquisition process, bandwidth of data flow and computing architecture requirements.

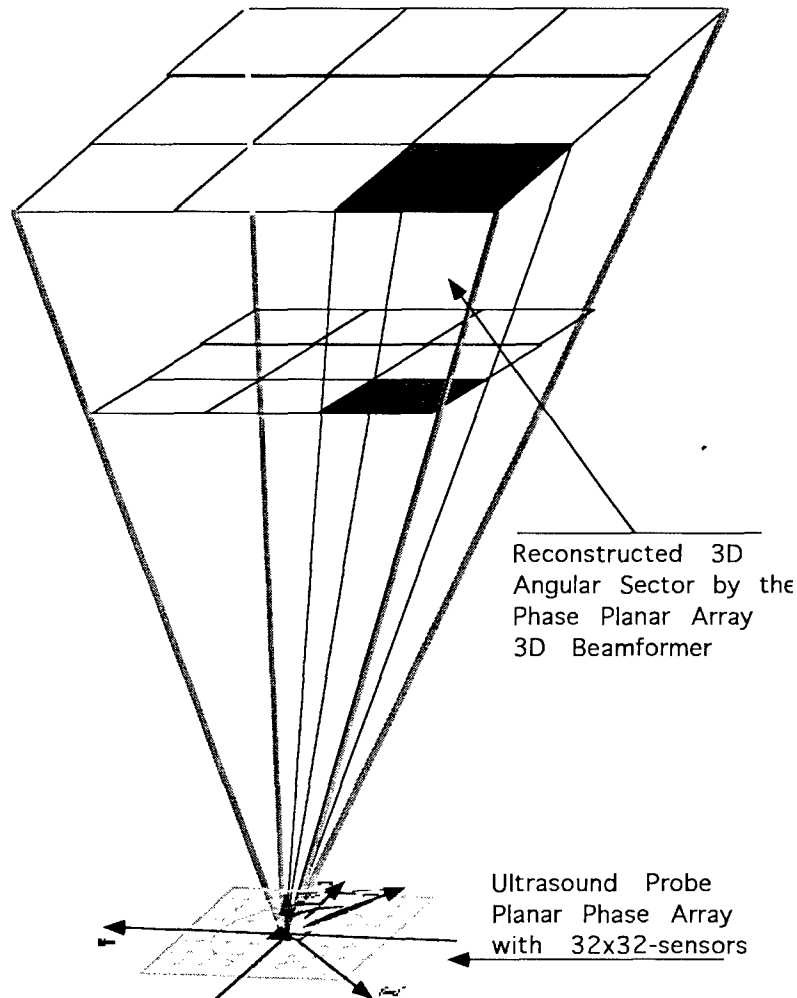


Figure 17. Volume 4D Digital Scanning for Ultrasound Applications using Radar & Sonar Phased Array Adaptive Beamforming of DRDC Toronto real 3D ultrasound system development.

6.2.2 Signal Conditioning and Data Acquisition Unit

The signal conditioning unit and the performance characteristics of the data acquisition system are discussed in Section 6.2.3. Briefly, the requirements

for the data acquisition process of the received ultrasound energy field by the omni-directional receiving transducers of the 32x32 planar array, include:

The digitization process of the 32x8 sub-apertures by a 14-bit 256-channel A/D unit that will provide the signals to a system of pin connectors-cables with suppressed cross-talk characteristics (minimum 35 dB). The sampling frequency is 33 MHz for each of the channels associated with a receiving single sensor. The multiplexer associated with the A/DC allows the sampling of the 32x32-sensors of the planar array in four consecutive active transmissions.

The computing architecture, (see Table 1) includes sufficient data storage capabilities for the sensor time series as indicated by the system requirements of Figures 17 & 18. The A/D and signal conditioning modules of the data acquisition process and the communication interface should be controlled with software drivers that form an integral part of the computing architecture defined in the following section 6.2.3. The PC based computing architecture includes dedicated software that allows control of the data acquisition and storage process.

Computing Architecture Requirements for Volumetric 3D U/S Imaging System Using Planar Phased Arrays

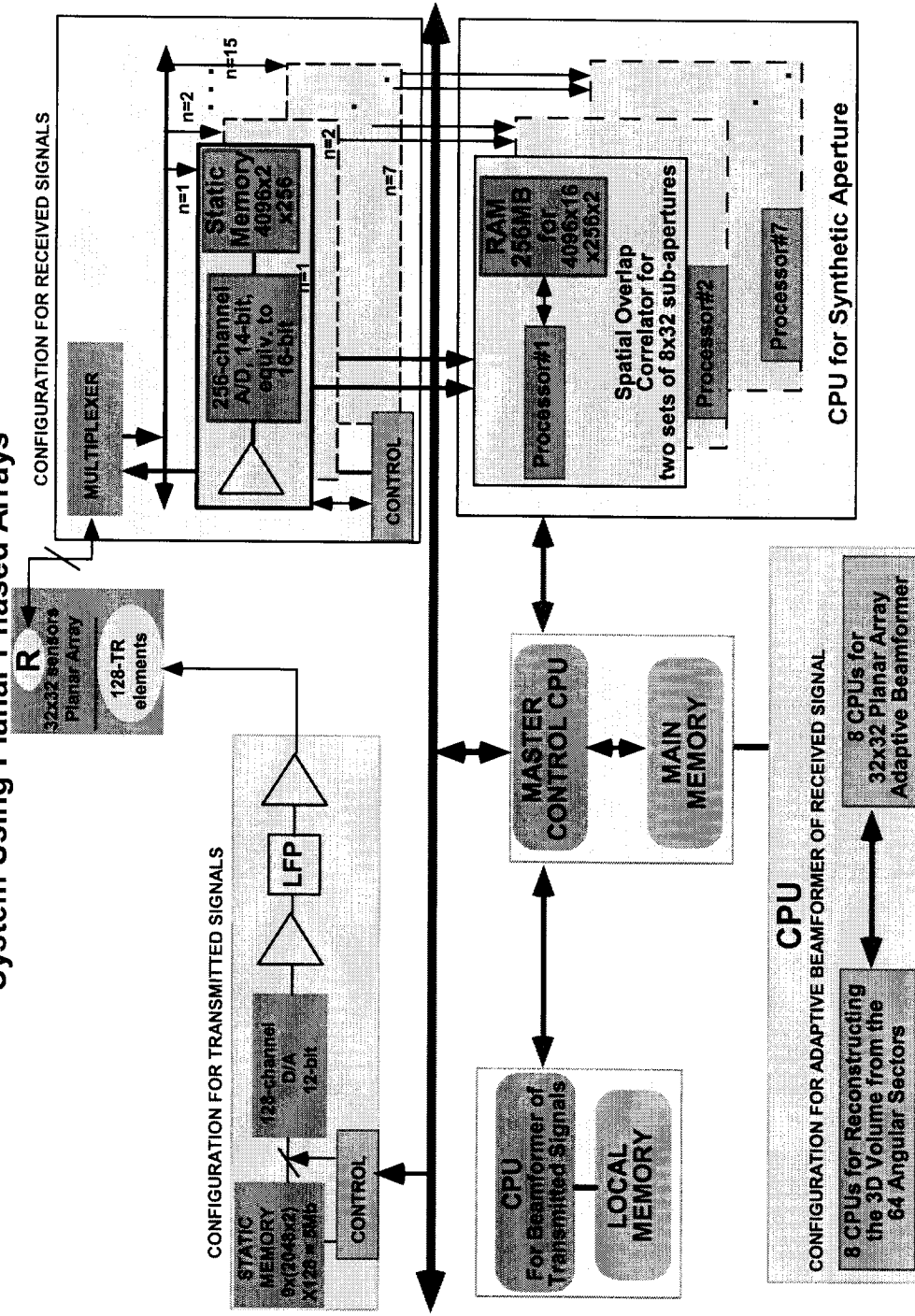


Figure 18. Structure of the PC-based computing architecture development for the real 3D ultrasound system development.

6.2.3 Bandwidth Requirements

The above data acquisition characteristics define the bandwidth of the data transfer process as follows:

1. The volumetric 3D ultrasound system will cover a $40^\circ \times 40^\circ$ angular sector with maximum penetration depth of 15 cm, as depicted in Figure 17. The transmitting beamformer of the 12×12 active planar array steers 4 to 5 beams across azimuth and 4 to 5 beams across elevation. This process defines a maximum of 25 angular sub-sectors, each of $10^\circ \times 10^\circ$ angular size, as shown in Figure 17.
2. For each sub-sector of $10^\circ \times 10^\circ$, four consecutive active transmissions are required to illuminate the specific sub-sector of interest and form a coherent synthetic aperture of 32×32 sensors.
3. For a penetration depth of 15cm, the shortest time delay between two consecutive active transmissions is defined by $(30/154000) = \tau = 0.2 \text{ ms}$.
4. Since the sampling frequency per channel of the A/D unit is $F_s = 33 \text{ MHz}$, the maximum number of samples for each receiving time series is 8000 samples.
5. In this case, the requirement for data transfer is $(256\text{-channels}) \times (4096\text{-samples}) \times (2\text{-bytes}) = 2 \text{ Mb in } 0.2 \text{ ms}$
6. Thus, for a specific focus range, the acquisition process requires:
 - $(4 \text{ transmissions}) \times (0.2 \text{ ms})$, a period of **$T = 1.6 \text{ ms}$** to sample a $10^\circ \times 10^\circ$ sub-sector.
 - In this case, the requirement for data transfer is **$8 \times 2 \text{ Mb} = 16 \text{ Mb in } 1.6 \text{ ms}$**
 - $(9 \text{ transmissions}) \times (4 \text{ transmissions-per-sub-sector}) = 36 \text{ transmissions}$ or a period of **$T = 57.6 \text{ ms}$** to sample the full $30^\circ \times 30^\circ$ angular sector.
 - In this case, the requirement for data transfer is **$9 \times 16 \text{ Mb} = 144 \text{ Mb in } 57.6 \text{ ms}$** .
7. To track cardiac motion effects with the proposed 3D US system, we set as requirement to achieve 10 samples of the $30^\circ \times 30^\circ$ angular sector in 1 second. Although the number of 10 samples is considered small to track most of the heart's complex motion effects, this limit of 10 samples for 4D volumetric visualization of the heart's motion may be increased at a later time without major modifications in the computing architecture structure of the proposed 3D ultrasound system.
8. Thus, the requirement for data transfer for 4D volumetric imaging is **$10 \times 144 \text{ Mb} = 1.44 \text{ Gbytes in } 1 \text{ second}$** and the longest time delay between two consecutive active transmissions may be as long as **$\tau = 1.587 \text{ ms}$** , to accommodate the requirement for a total number of 360 transmissions in 1 second.
9. If the computing architecture characteristics of the data acquisition unit will allocate the **2 MB** of data from each one of the 4 transmissions in separate memory locations through separate bus-lines, as shown in Figure 18, then the bandwidth requirements are defined as follows:
10. For each dedicated bus-line, the requirement of data transfer is reduced to $1260/7 \text{ Mbytes} = 180 \text{ Mbytes in } 1 \text{ second}$, which is achievable.
11. Simultaneous focusing at different depths is achieved by designing digital pulses that include wavelets with different frequency regimes and different frequency

modulation. This approach is conceptually similar with that being used in sonar technology [1].

Figure 18 provides a schematic overview for the PC-based computing architecture of DRDC Toronto's 3D Ultrasound system under development. It consists of two major sections. The upper section defines the computing architecture for the data acquisition unit. The lower section in Figure 18, provides the main components of the PC-based computing architecture for the processing and image reconstruction of the ultrasound sensor time series that has been briefly reviewed in Section 6.1. The lower section of the computing architecture is divided in 5 major CPU structures that should deliver the following functionality:

- 1) CPU for synthetic aperture. The 7-processors of this component, shown in Figure 18, should have direct connection with the bus-lines of the data acquisition unit. The output of the CPU synthetic aperture structure would provide a stream of $(32 \times 4096) \times (32 \times 4096)$ time series for adaptive beamforming. Moreover, the memory requirements should be dedicated to this CPU structure as local memory.
- 2) CPU for the transmitting beamformer, shown at the left hand side of Figure 18. This CPU unit estimates the active steering beams $(12 \times 12) \times 2048$, that drives the digital-to-analog converter (D/AC) unit of the active sensors of the planar array.
The bandwidth requirements for the transmitting beamformer are:
 - 9 sets of 7 identical beam time series, each of size, $(12 \times 12) \times 2048 \times 2 \approx 0.5$ Mb
 - Since, for a given focus depth, the steered beams of the active beamformer will not change during the acquisition process of the $10^\circ \times 10^\circ$ angular sector in 1 second, the computing architecture of the data acquisition unit should have enough memory to store: 9×0.5 Mb = **4.5 Mb** of data for a given focus range. In other words, for a given range, the operation of the 3D ultrasound system will initiate a data transfer of 4.5 Mb to the memory of the D/AC unit of the data acquisition system, before the actual transmission and acquisition process begins. Thus, the bandwidth requirements in this case are very small and are being translated into memory requirements for the computing architecture of the data acquisition unit, associate with the D/AC.
- 3) CPU for the adaptive beamformer, which is shown at the lower part in Figure 16. This CPU sub-structure requires computationally intensive vector operations of size $(32 \times 4096) \times 16$ complex numbers = 2 Mb. The requirement is for several vectors to be processed simultaneously, which leads to a substantial parallelization of the CPU structure with significant memory requirements. DRDC Toronto's adaptive beamforming structure has already been developed and has formed the basis to define the characteristics of the CPU structure in terms of throughput and memory requirements discussed in Section 6.1.
- 4) The output of the CPU adaptive beamformer provides a number of beams, generated by the adaptive beamforming structure with the following beamwidth characteristics:
 - It has been assessed that the proposed adaptive beamforming structure provides an effective beam-width size, which is equivalent to that of a three times longer aperture along azimuth and three times longer along elevation of the deployed planar array. Thus, the deployed receiving 32×32 planar array

would have beamwidth characteristics equivalent with those of a $(32 \times 3) \times (32 \times 3)$ size planar array.

- The beam-width of a receiving 32×32 planar array with element spacing of 0.5 mm for a 3 MHz centre frequency, is approximately 3.7° .
 - Thus the receiving adaptive beams along azimuth would provide:
 - $(3 \text{ sub-angular-sectors}) \times (45 \times 3) = 405$ beam time series with 4096 samples each along azimuth steering,
 - $(3 \text{ sub-angular-sectors}) \times (45 \times 3) = 405$ beam time series with 4096 samples each along elevation steering.
 - The **effective angular resolution of the proposed adaptive system** in terms of beam-width size will in be in angular sectors of less than $1^\circ \times 1^\circ$.
 - The above angular resolution capabilities of the adaptive system lead to the following tissue resolution characteristics:
 - **For C-scan** and for **depth of 10 cm**, the $1^\circ \times 1^\circ$ angular resolution sector corresponds to a $(1.7 \text{ mm}) \times (1.7 \text{ mm}) = 2.89 \text{ mm}^2$ **size of tissue resolution** and for **depth of 5 cm** to a $(0.8 \text{ mm}) \times (0.8 \text{ mm}) = 0.64 \text{ mm}^2$ **size of tissue resolution**.
 - **For B-scan** the **line resolution** will be equivalent to the wavelength of the transmitted centre frequency, which is **0.5 mm**.
 - Thus, the **volume resolution** of the 3D adaptive beamforming structure will be equivalent to $(0.64 \text{ mm}^2) \times (0.5 \text{ mm}) = 0.32 \text{ mm}^3$, **in 3D tissue size at a depth of 5 cm**.
 - Finally, the output of the adaptive beamformer will provide $(405 \times 405) \times 2048$ set of data for B-scan, C-scan and S-scan ultrasound imaging tomography applications and with 10 frames per second to track dynamic characteristics, especially for cardiac imaging applications.
- 5) The CPU structure for the 4D volume visualisation of the output of the beam-time series provides the post-processing functionality for the proposed 3D ultrasound system.

In summary, the computing architecture of the proposed system has the following characteristics:

Real time performance,

PC based,

Parallelization for vector based signal processing including digital beamformers. Figures 16-17 and Sections 5 and 6 provide sufficient details to assess the throughput requirements associated with the project development activity.

The A/DC is well grounded and capable to sample the 256 channels with an equivalent 14-bit resolution and 33 MHz sampling frequency per channel. Moreover, the unit has dedicated memory and separate bus-lines to achieve the data transfer rates defined above.

The multiplexer integrated with the A/DC allows for the sampling of the (32x32) planar array in groups of seven spatially overlapping sub-apertures (8x32). The data acquisition period between two consecutive sub-apertures should be 0.2ms.

The D/AC is capable to drive 144 channels with 12-bit resolution and 33 MHz sampling frequency. The period between two consecutive active transmissions is in the range of 0.2 ms. Moreover, the local memory of the D/AC unit has the capability to store the active beam time series with total memory size of 4.5 Mb, being generated by the main computing architecture for each focus depth and transferred to the local D/AC memory when the transmission-acquisition process begins.

6.3 Synthetic Data

6.3.1 Synthetic Data Results for Ultrasound Systems Deploying Line Arrays

Performance assessment and testing of the generic conventional and sub-aperture adaptive beamformers that have been discussed in this report, have been carried out with the following type of simulated ultrasound data:

Synthetic data sets that have been generated for an active ultrasound system deploying a line array. The simulated line array sensor time series employed:

- An aperture size of linear array: $N=32$ sensors with detector pitch of 0.4mm
- Sampling Frequency = 33 MHz
- Two FM pulses of duration 1.52 μ s.
- The frequency characteristics defined in Table 2 for the first three experiments.
- The position characteristics defined in Table 2 for the first three experiments.
- The position and frequency characteristics defined in Table 3 for the fourth experiment.

Table 2: Parameters for Cases I, II and III.

	Point Source 1 (Left)				Point Source 2 (Right)			
	Fc MHz	BW MHz	Bearing	Depth	Fc MHz	BW MHz	Bearing	Depth
Case I	2.1	1.1	84°	65 mm	2.0	1.0	96°	65 mm
Case II	3.6	2.1	84°	65 mm	3.5	2.0	96°	65 mm
Case III	5.0	3.0	84°	65 mm	5.0	3.0	96°	65 mm

Table 3: Parameters for Case IV.				
	Fc	BW	Bearing	Depth
Source 1	4.0 MHz	2.0 MHz	80°	10 mm
Source 2	4.0 MHz	2.0 MHz	92°	25 mm
Source 3	2.0 MHz	1.0 MHz	84°	40 mm
Source 4	2.0 MHz	1.0 MHz	96°	50 mm

The synthetic data sets generated were processed with:

- Phased array conventional beamformers with angular sector steering between 67.5° and 112.5°, and beam resolution of 0.5°/beam.
- Phased array sub-aperture adaptive STMV beamformers with angular sector steering between 67.5° and 112.5°, and beam resolution of 0.5°/beam.

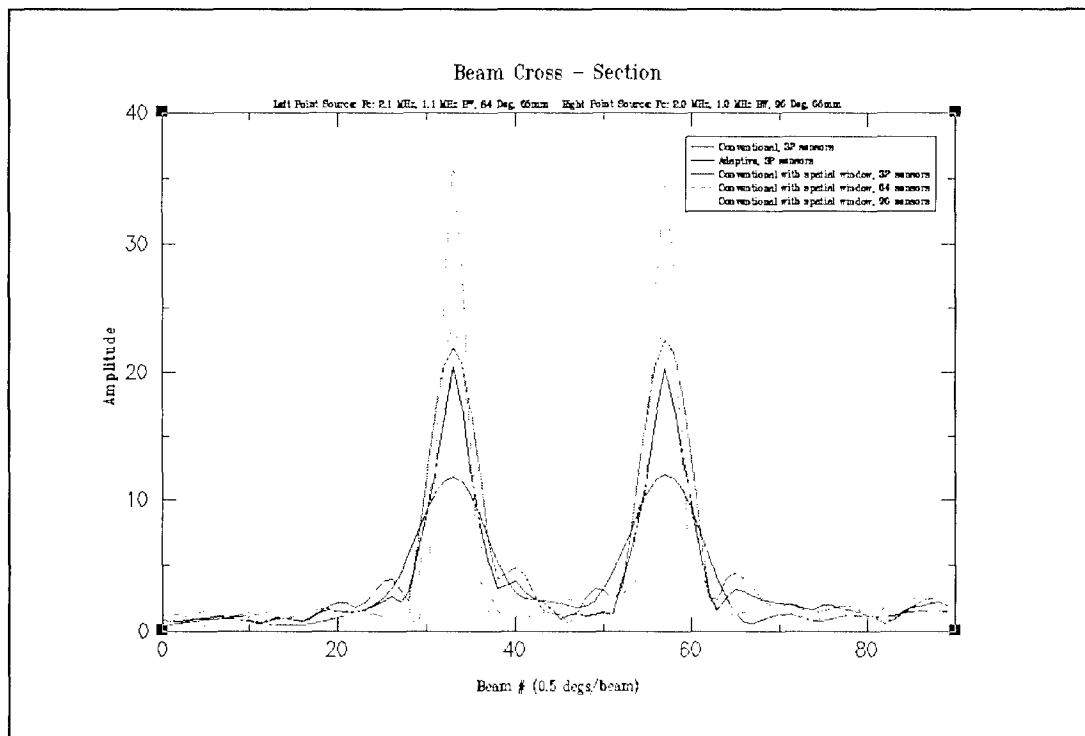


Figure 19. Beam pattern resulting from Case I.

6.3.1.1 Case I: Results

The resulting broadband beam pattern plots from the experiments with the parameters defined as Case I are shown in Figure 19. The broadband beam pattern of the conventional beamformer with spatial shading is shown by the blue curve, and from the conventional beamformer with no spatial shading with the red curve. The black curve shows the broadband beam pattern for the

STMV-SA adaptive beamformer. These plots clearly show that the angular resolution provided by the STMV-SA advanced beamformer is superior of the conventional beamformer. The green and orange curves show the broadband beam patterns derived from the conventional beamformer with spatial windowing for an aperture size of 64 elements and 96 elements respectively. It is evident that the effective resolution achieved by the STMV-SA beamformer with 32 elements is approximately the same as the conventional beamformer with 96 elements.

Figure 20 shows the results of the beamformers in the time domain. The images plot the envelopes of the FM signals computed using the Hilbert transform, with time delay (depth) shown vertically and beams (angle) shown horizontally. The top row of images from left to right show the reconstructed image from the conventional beamformer with 32 detectors and spatial shading. The second image shows the result from the 64 element conventional beamformer without spatial shading. The third image shows the results from the conventional beamformer with spatial shading for a 96-element array. These images correspond to the blue, red and orange curves in Figure 19, respectively. The lower row shows the conventional beamformer with spatial shading for a 32 element on the left and the STMV-SA advanced beamformer for a 32-element array on the right. These images correspond to the green and black curves of Figure 19 respectively. These images confirm that the angular resolution of the STMV-SA beamformer is superior and equivalent to a 64 element conventional beamformer with spatial shading and approaches the angular resolution of a 96 element conventional beamformer with spatial shading.

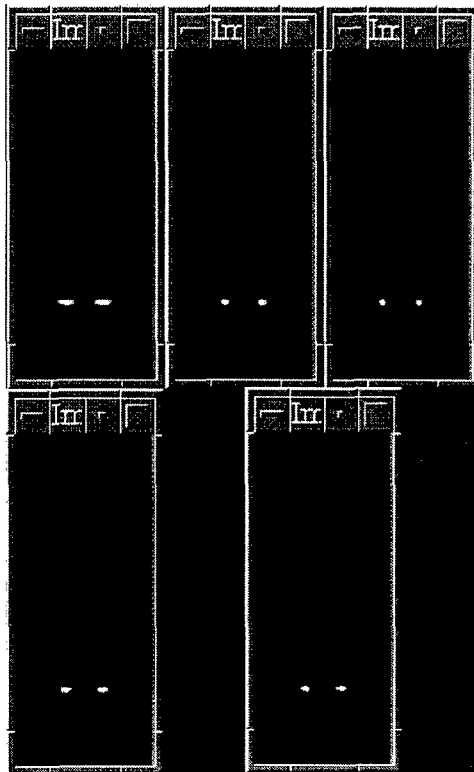


Figure 20. Reconstructed Images resulting from Case 1

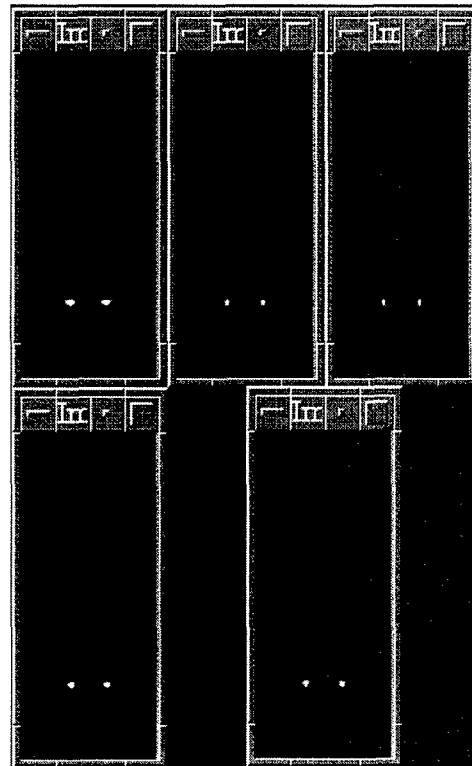


Figure 21: Reconstructed Images resulting from Case II.

6.3.1.2 Case II: Results

The resulting broadband beam patterns from the experiments with the parameters defined as Case II (see Table 2), are shown in Figure 22. The broadband beam pattern of the conventional beamformer with spatial shading is shown by the blue curve, and from the conventional beamformer with no spatial shading with the red curve. The black curve shows the broadband beam pattern for the STMV-SA adaptive beamformer. These plots once again show that the angular resolution provided by the STMV-SA advanced beamformer is superior of the conventional beamformer in the frequency regime defined for Case II. The green and orange curves show the broadband beam patterns derived from the conventional beamformer with spatial windowing for an aperture size of 64 elements and 96 elements respectively. In this case, the effective resolution achieved by the STMV-SA beamformer with 32 elements approaches that of the conventional beamformer with 64 elements.

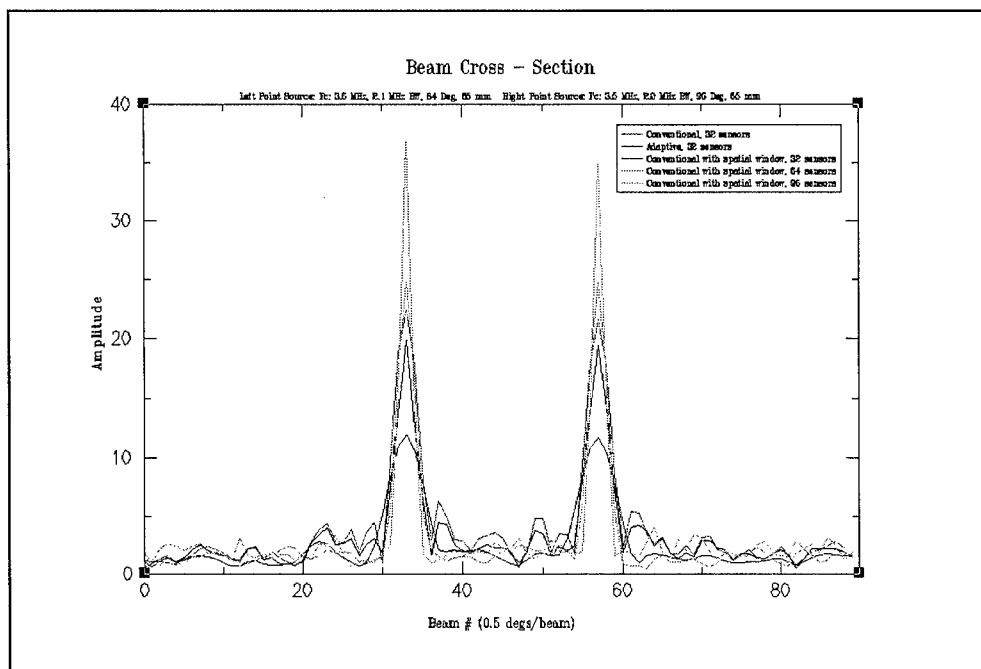


Figure 22. Beam pattern resulting from Case II.

Figure 21 shows the results of the beamformers in the time domain. The images plot the envelopes of the FM signals computed using the Hilbert transform, in the same manner as in Figure 20. The top row of images from left to right show the image from the conventional beamformer with 32 detectors and spatial shading. The second image shows the result from the 64-element conventional beamformer with spatial shading. The third image shows the results from the conventional beamformer with spatial shading for a 96-element array. These images correspond to the blue, red and orange curves in Figure 19 respectively. The lower row shows the conventional beamformer with spatial shading for a 32 element and the STMV-SA advanced beamformer for a 32-element array. These images correspond to the green and black curves of Figure 19 respectively. These images confirm that the angular resolution of the STMV-SA beamformer approaches the angular resolution of a 64 element conventional beamformer with spatial shading.

6.3.1.3 Case III: Results

Figure 23 shows the resulting broadband beam pattern plots from the experiments with the parameters defined as Case III (see Table 3). The broadband beam pattern from the conventional beamformer with spatial shading is shown by the blue curve, and from the conventional beamformer with no spatial shading with the red curve. The black curve shows the broadband beam pattern for the STMV-SA adaptive beamformer. Again, in this case, the angular resolution provided by the STMV-SA advanced beamformer is superior to the conventional beamformer in the frequency regime defined by the parameters of Case III (see Table III). However, the improvement is less marked than in the previous two cases. The green and orange curves show the broadband beam patterns derived from the

conventional beamformer with spatial windowing for an aperture size of 64 elements and 96 elements respectively. The improvements achieved in the previous cases are not as evident in this case (e.g. Case III).

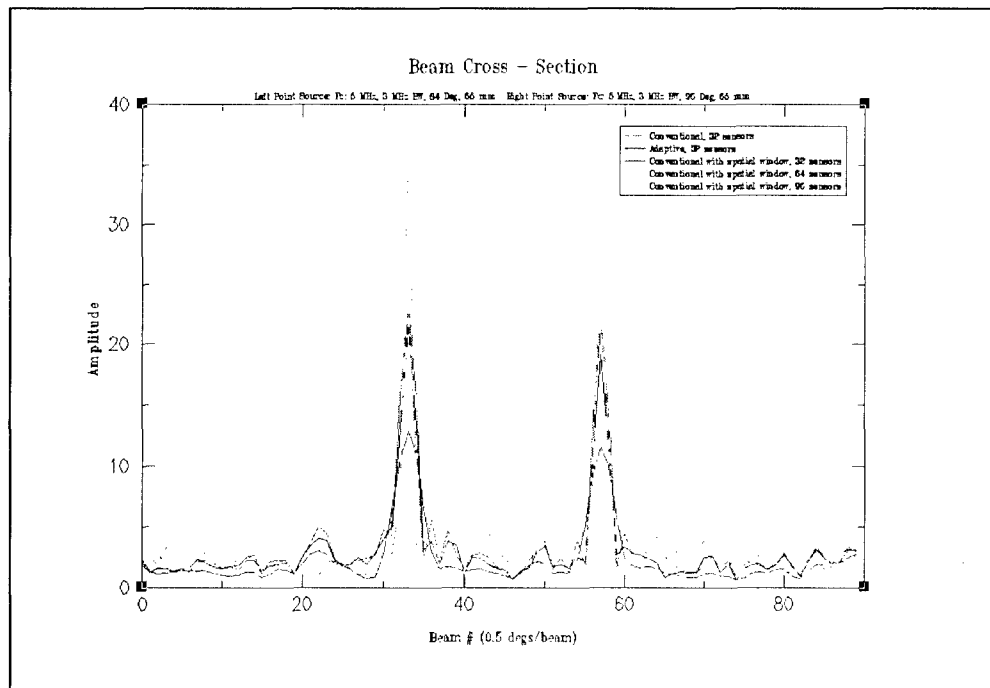


Figure 23. Beam pattern resulting from Case III.

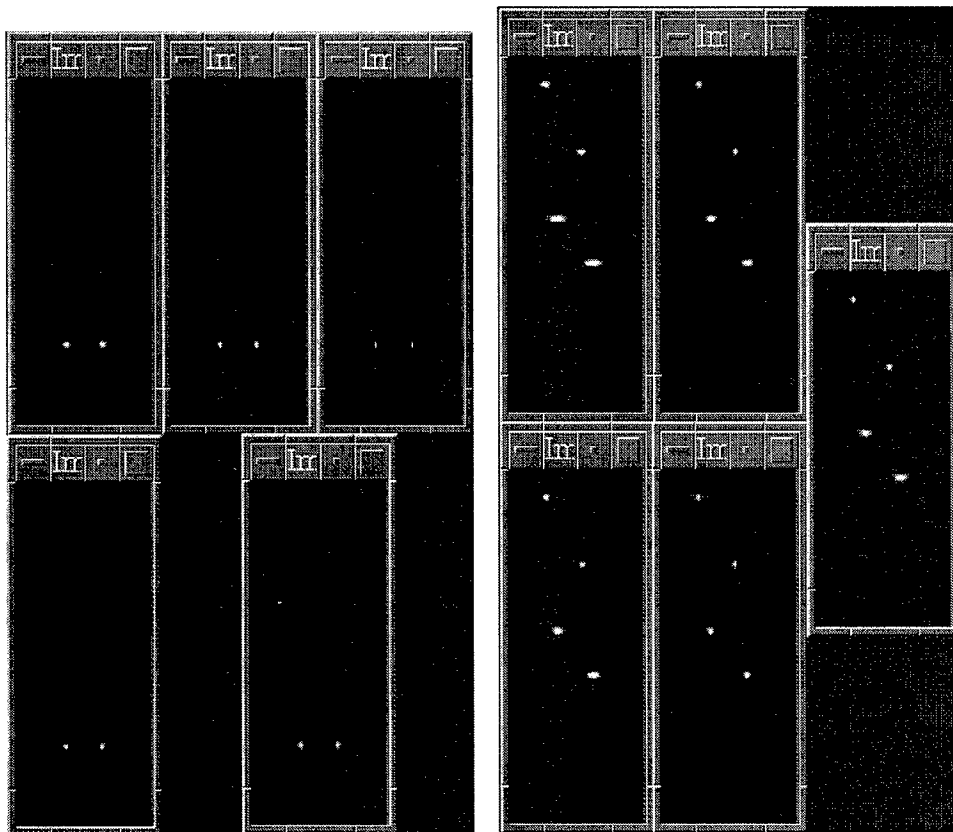


Figure 24. Images resulting from Case III.

Figure 25. Images resulting from Case IV.

Figure 24 shows the image reconstruction results of the beamformers in the time domain. The images plot the envelopes of the FM signals computed using the Hilbert transform, in the same manner as in Figures 20 and 21. Since the frequency regime of Case III is higher than the design frequency of the array, this affects the STMV-SA beamformer's performance; and the gains achieved are not as evident as in the previous two cases. Therefore, the conclusion from these simulations is that for the advanced beamformers to achieve optimum performance, in terms of angular resolution, it is essential that the frequency regime of the deployed ultrasound signals should be close to the design frequency of the array.

6.3.1.4 Case IV: Results

The images in Figure 25 show the operation of the beamformers in a more general case. The parameters of the sources are defined in Table 3. The upper two images show the results from the conventional beamformer with spatial window for a 32-element array on the left, and a 64-element array on the right. The lower two images show the conventional beamformer with no

spatial shading for a 32-element array on the left and a 64 element array on the right. The rightmost image shows the results from the STMV-SA beamformer for a 32-element array. Comparison of the results from the STMV-SA beamformer and the conventional beamformer with spatial shading show that the STMV-SA beamformer provides better angular resolution than the conventional beamformer employing a 64 element array. Without spatial shading, the angular resolution of the 64 element conventional beamformer is approximately equivalent with that of the STMV-SA beamformer, but it suffers from sidelobe effects, which are most evident with the closest source. Overall, these results show that the STMV-SA beamformer provides improved angular resolution over the conventional beamformer with spatial shading. In addition, it provides improved sidelobe suppression over that of the conventional beamformer with no spatial shading.

6.3.2 Synthetic Data Results for Ultrasound Systems Deploying Planar Arrays

The synthetic data experiments for the planar array was carried out using the Field II ultrasound simulator program obtained from the Technical University of Denmark (<http://www.it.dtu.dk/~jaj/field>). The simulator simulates point sources, and was set up to simulate 5,000 point sources arranged in a spherical shell, conforming to the specifications of the system defined in Section 6.2. Specifically, a 32x32 planar array on receive and a 12x12 array on transmit were simulated, with element spacing of 0.3 mm and sampling frequency of 33 MHz. The FM pulse was centred at 2.5 MHz, with a bandwidth of 4.0 MHz. The illumination pattern is as described in Figure 17, but with six transmit beams spaced 10° apart covering 60° in each direction (azimuth and elevation). The result was a total of 36 sectors. A conventional beamformer was used to process the data received by the 32x32 array. The array decomposition was preformed as defined in Section 5.2.4, processing each row of the array to obtain azimuth beams, and then processing the azimuth beams for a given direction for all of the rows to obtain 3D azimuth and elevation beams. A complete reconstruction of the beams into a volume was then performed.

The C-scans derived from the 3D reconstructed volumes of the spherical shell are shown in Figure 26. In this image, which shows a slice of the spherical shell, the expected ring that corresponds to the cross section of a shell is visible. The left and right images in Figure 26 correspond to the 3D conventional and adaptive beamformers, respectively. The better performance of the adaptive beamformer is evident in this case as it provides better detection and image definition than the corresponding conventional beamformer. The visualization software was provided by Prof. Sakas of Fraunhofer (National Research Institute, Darmstadt, Germany) [60], as part of our technical exchanges within the framework of the European-Canadian project MITTUG [81].

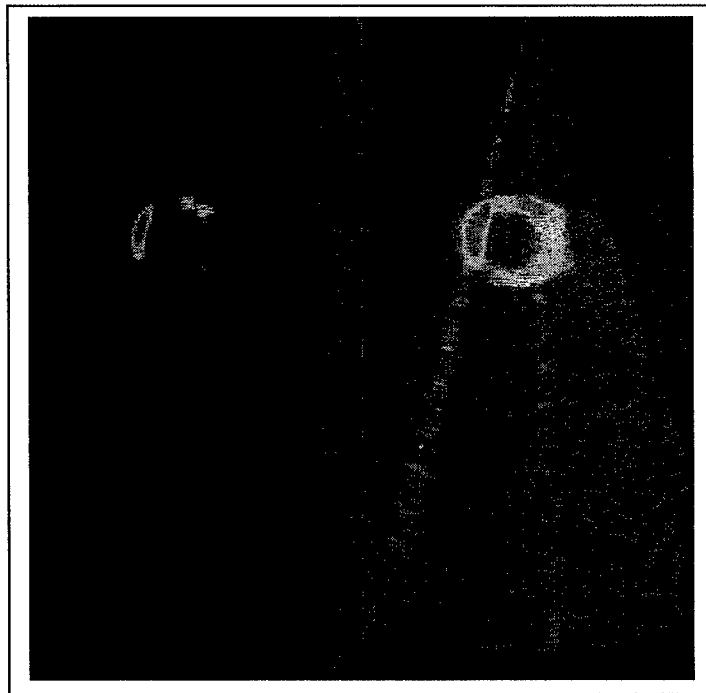


Figure 26. C-scans derived from the 3D reconstructed images of the simulated spherical shell. Left image, reconstructed with the 3D conventional beamformer. Right image, reconstructed with the 3D adaptive beamformer.

Figure 27 shows the 3D volume reconstruction of the spherical shell using the 3D conventional (left image) and the 3D adaptive (right image) ultrasound beamformers defined in the present report. As was the case with the C-scans (Figure 26), the results in Figure 27 show that the 3D adaptive beamformer provides better image definition than the corresponding 3D conventional beamforming results.

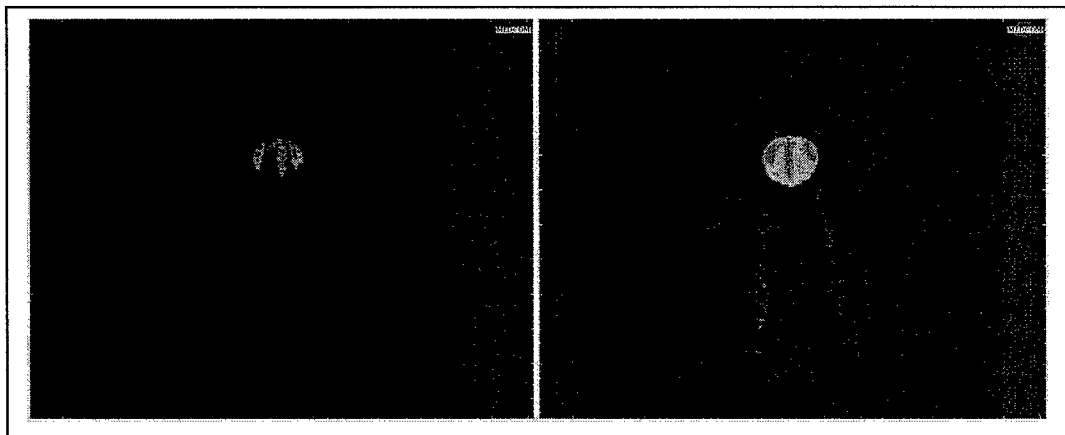


Figure 27. 3D volume reconstruction of the simulated spherical shell. Left image, reconstructed with the 3D conventional beamformer. Right image, reconstructed with the 3D adaptive beamformer.

6.3.3 Real Data Results for Ultrasound Systems Deploying Linear Arrays

The real data tests were carried out using the equipment described at the beginning of this section (Section 6) and shown in Figures 15 and 16. The ultrasound system employs a 96-element array, of which only 32 are active at any given time. The first 32 elements of the array are selected, and 8 of these elements transmit an RF pulse to illuminate the object of interest. The illumination is focused to the broadside of the 32 elements selected, and at a selected focal distance. The 32 elements then receive reflections. This is for one active transmission. For the next transmission, a new set of 32 elements is selected and the process is repeated. The new 32 elements are selected in a sliding window fashion, using 31 from the previous active transmission, and one new element. In other words, the active elements slide over (or pitch) by one detector. This process is repeated by sliding one detector for each transmission until 64 active transmissions are made, and all elements have been exhausted. The experiments were carried out using data acquired in this manner. In the standard operation of the ultrasound system more active illuminations are achieved by using the so called "edge-effects" where the active elements begin with 16 active elements initially, and increase with each pitch (or active transmission) to a maximum of 32. When the last valid pitch that allows 32 active detectors is reached, the system continues until decreasing the number of active elements until there are only 16 elements active. In other words, in standard operation, the system pretends that there are 16 non-working detectors before the 96-element array, and 16 more after it, making it a potential 128-element array. By using a sliding window of length of 32 elements, then there are 96 active transmissions (and reflections received) possible. In the experiments, only the 64 pitches where 32 physical elements were active were used, hence there are 64 transmissions to broadside. The received reflections are beamformed to broadside, and a selected focal depth for these 64 data segments received. This yields an image with 64 rows – one for each active transmission position.

The phantoms used in the experiments were:

Two wire cross sections simulating two point sources in space suspended in a water bath.

A ball suspended in a water bath.

The resulting images from the ultrasound system, the conventional beamformer with spatial shading, and the STMV-SA beamformer are shown in Figures 28 and 29. The leftmost image of Figure 28 shows the image obtained from the ultrasound system under standard operating conditions. The centre image shows the results obtained by processing the raw data captured by the data acquisition with a conventional beamformer including spatial shading. The right most image shows the image obtained by processing the raw data with the STMV-SA beamformer. These two images to the right are plotted using a logarithmic scale to show the background effects more clearly. The left image and the two right images do not employ the same magnification factor. Comparison of these images shows the improvement in detection.

There are three major factors that affect the performance of the beamformers in this scenario. First, the frequency regime is well outside of the design frequency of the array. With an element spacing of approximately 0.4 mm the design frequency of the array is approximately 1.875 MHz, while the centre frequency of the RF pulses is approximately 8 MHz with 8 MHz bandwidth. The second factor is the lack of dynamic range of the

A/D converter, which is equivalent to 4-bit. Thus, the A/D converter does not exploit the full dynamic range during data acquisition, thereby compromising the SNR of the system. The third factor is the sensitivity of the data acquisition system to background interferences. The interference pattern created by this in combination with the lack of dynamic range is visible as diagonal lines, and spots that form a diagonal pattern in Figures 28 and 29. Figure 29 shows the results with the ball phantom in the same format as Figure 28. Despite the interference, the improvement in detection by the STMV-SA beamformer is evident. There are currently efforts underway to improve the cabling and electronics of the data acquisition system, shown in Figure 16, to reduce the sensitivity to interference. In addition, variable amplifiers will be added to exploit the full dynamic range of the system's A/DC peripheral.

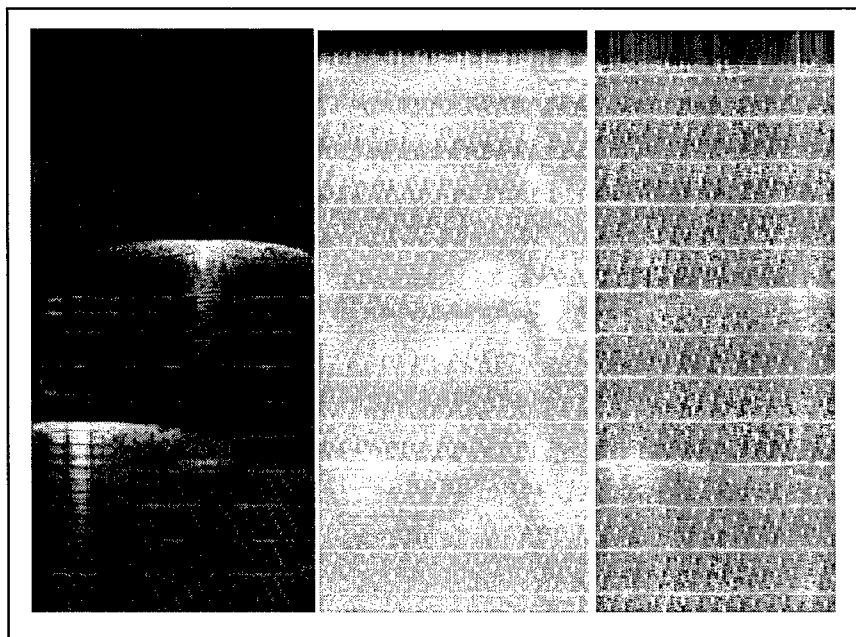


Figure 28. Results with wire phantom.

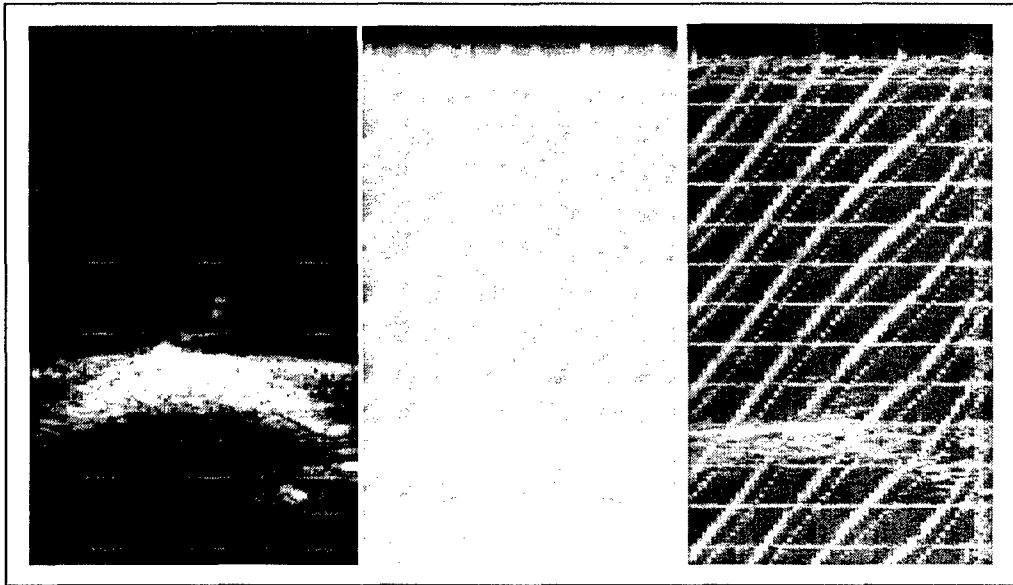


Figure 29. Results with Ball Phantom.

7. Conclusion

The synthetic and real data results of this report indicate that the generic multi-dimensional adaptive concept addresses practical concerns of near-instantaneous convergence, shown in Figures 18-29, for ultrasound systems. The performance characteristics of the sub-aperture adaptive beamformer compared with that of the conventional beamformer are reflected as improvements in directional estimates of azimuth and elevation angles and suppression of reverberation effects. This type of improvement in azimuth and elevation bearing estimates is essential for 3-D ultrasound operations.

In summary, a generic beamforming structure has been developed for multi-dimensional sensor arrays that allows the implementation of conventional, synthetic aperture and adaptive signal processing techniques in integrated active-passive real time systems. The proposed implementation is based on decomposing the 2-D and 3-D beamforming process in sub-sets of coherent processes and creating sub-aperture configurations that allow the minimization of the number of degrees of freedom of the adaptive processing schemes. The proposed approach has been applied to line, planar, and cylindrical arrays of sensors where the multi-dimensional beamforming is decomposed into sets of line-array and/or circular array beamformers. Moreover, the application of spatial shading on the generic multi-dimensional beamformer is a much simpler process than that of the fully coherent 3-D beamformer. This is because the decomposition process allows two simple and separate applications of spatial shading (i.e. one for circular and the other for line arrays).

The beamformers have been applied to real and simulated data sets of ultrasound systems. In general ultrasound systems require near-field beamforming. The results with the real and synthetic data sets show that firstly, the decomposition and sub-aperture techniques hold true for focused beamformers. Also, the results show that the performance of the advanced beamformer is not affected by the near-field conditions presented in ultrasound systems, and that performance gains over conventional beamformers are achieved.

The fact that the sub-aperture adaptive beamformers provided array gain improvements for FM signals under a real time data flow as compared with the conventional beamformer demonstrates the merits of these advanced processing schemes for practical ultrasound applications. In addition, the generic implementation scheme of this study suggests that the design approach to provide synergism between the conventional beamformer, the synthetic aperture and the adaptive processing schemes, (e.g., see results in Figures 22 and 23) is an essential property for system applications.

Although the focus of the implementation effort included only a few adaptive processing schemes, the consideration of other types of spatial filters for real time ultrasound applications should not be excluded. The objective here was to demonstrate that adaptive processing schemes could address some of the challenges that the next generation ultrasound systems will have to deal with in the near future. Once a generic signal processing structure is established, as suggested in the report, the implementation of a wide variety of processing schemes can be achieved with minimum efforts for real time systems deploying multi-dimensional arrays. Finally, the results presented in this report indicate that the sub-aperture STMV adaptive scheme address the practical concerns of near-instantaneous convergence associated with the implementation of adaptive beamformers in ultrasound systems.

8. References

- [1] S. Stergiopoulos, "Implementation of adaptive and synthetic aperture processing schemes in integrated active-passive sonar systems", *Proc. IEEE*, **86**(2), 358-396, 1998.
- [2] W.C. Knight, R.G. Pridham and S.M. Kay, "Digital Signal Processing for Sonar", *Proceedings of the IEEE*, **69**(11), pp. 1451-1506, 1981.
- [3] B. Windrow et. al., "Adaptive Antenna Systems", *Proceedings IEEE*, **55**(12), pp. 2143-2159, 1967.
- [4] A. A. Winder, "Sonar System Technology, *IEEE Trans. on Sonic Ultrasonics*, **SU-22**(5), pp. 291-332, 1975.
- [5] A.B. Baggeroer, "Sonar Signal Processing" (article in Applications of Digital Signal Processing - Editor: A.V. Oppenheim), Prentice-Hall, 1978.
- [6] S. Stergiopoulos and A.T. Ashley, "Guest Editorial " for a Special Issue on Sonar System Technology, *IEEE, J. Oceanic Eng.*, **18**(4), 361-366, 1993.
- [7] Dhanantwari A.C., Stergiopoulos S. and Grodski J., "Implementation of Adaptive processing in Integrated Active-Passive Sonars deploying cylindrical arrays", *Proceedings of Underwater Technology '98, UT'98*, Tokyo Japan, April-1998.
- [8] W. C. Queen, "The Directivity of sonar receiving arrays", *J. Acoust. Soc. Am.*, **47**, 711-720, 1970.
- [9] V. Anderson and J. Munson, "Directivity of spherical receiving arrays", *J. Acoust. Soc. Am.*, **35** 1162-1168, 1963.
- [10] W. M. Carey and W.B. Moseley, "Space-time processing, environmental-acoustic effects", *IEEE J. Oceanic Eng.*, **16**, pp. 285-301, 1991; also in *Progress in Underwater Acoustics*, N.Y.: Plenum, pp. 743-758, 1987.
- [11] S. Stergiopoulos and E.J. Sullivan, "Extended towed array processing by overlapped correlator ", *J. Acoust. Soc. Am.*, **86**(1), 158-171, 1989.
- [12] S. Stergiopoulos, "Optimum bearing resolution for a moving towed array and extension of its physical aperture ", *J. Acoust. Soc. Am.*, **87**(5), 2128-2140, (1990).
- [13] E.J. Sullivan, W.M. Carey and S. Stergiopoulos, "Editorial" special issue on Acoustic Synthetic Aperture processing, *IEEE J. Oceanic Eng.*, **17**(1), 1-7, 1992.
- [14] S. Stergiopoulos and H. Urban, "An Experimental Study in Forming a Long Synthetic Aperture at Sea", *IEEE J. Oceanic Eng.*, **17**(1), 62-72, 1992.
- [15] G.S. Edelson and E.J. Sullivan, "Limitations on the overlap-correlator method imposed by noise and signal characteristics", *IEEE J. Oceanic Eng.*, **17**(1), pp. 30-39, 1992.
- [16] G.S. Edelson and D.W. Tufts, "On the ability to estimate narrow-band signal parameters using towed arrays", *IEEE J. Oceanic Eng.*, **17**(1), pp. 48-61, 1992.
- [17] N.L. Owsley, "Sonar array processing", S. Haykin, Editor, Prentice-Hall Signal Processing Series, A.V. Oppenheim series editor, pp.123, 1985.
- [18] B. Van Veen and K. Buckley, "Beamforming: a Versatile Approach to Spatial Filtering", *IEEE ASSP Mag.*, pp. 4-24, 1988.
- [19] H. Cox, R.M. Zeskind and M.M. Owen, "Robust Adaptive Beamforming", *IEEE- Trans. Acoustic Speech Signal Proc.*, **ASSP-35**(10), pp. 1365-1376, 1987,

- [20] H. Cox, "Resolving power and sensitivity to mismatch of optimum array processors", *J. Acoust. Soc. Am.*, **54**(3), pp. 771-785, 1973.
- [21] A.H. Sayed and T. Kailath, "A State-Space Approach to Adaptive RLS Filtering", *IEEE SP Mag.*, pp. 18-60, July-1994.
- [22] J. Capon, "High resolution frequency wavenumber spectral analysis", *Proc. IEEE*, **57**, pp. 1408-1418, 1969.
- [23] T.L. Marzetta, "A new interpretation for Capon's Maximum Likelihood Method of frequency-Wavenumber Spectra Estimation", *IEEE- Trans. Acoustic Speech Signal Proc.*, **ASSP-31**(2), pp. 445-449, 1983.
- [24] S. Haykin, "Adaptive Filter Theory", Prentice-Hall, Englewood Cliffs, NJ, 1986.
- [25] A. Tawfik, A.C. Dhanantwari, and S. Stergiopoulos, "A Generic beamforming structure allowing the implementation of adaptive processing schemes into 2-D & 3-D arrays of sensors", *Proceedings MTS/IEEE OCEANS'97*, Halifax, Nova Scotia, Oct. 1997.
- [26] A. Tawfik, A.C. Dhanantwari, and S. Stergiopoulos, "A Generic beamforming structure for adaptive schemes implemented in 2-D & 3-D arrays of sensors", *J. Acoust. Soc. Am.*, **101**(5) Pt. 2, 3025, 1997.
- [27] S. Stergiopoulos, A. Tawfik and A.C. Dhanantwari, "Adaptive Microphone 2-D and 3-D Arrays for Enhancement of Sound Reception in Coherent and Incoherent Noise Environment", *Proceedings of Inter-Noise '97*, OPAKFI H-1027 Budapest, August 1997.
- [28] A. Tawfik A. and S. Stergiopoulos, "A Generic Processing Structure Decomposing the Beamforming process of 2-D & 3-D Arrays of Sensors into Sub-Sets of Coherent Processes", *Proc. of CCECE'97*, Canadian Conference on Electrical & Computer Engineering, St. John's, NF, May 1997.
- [29] N.L. Owsley, "Systolic array adaptive beamforming" NUWC Report **7981**, Sept. 1987.
- [30] S. Stergiopoulos, "Limitations on towed-array gain imposed by a non isotropic ocean", *J. Acoust. Soc. Am.*, **90**(6), pp. 3161-3172, 1991.
- [31] A.D. Whalen, "Detection of Signals in Noise", Academic Press, NY, 1971.
- [32] D. Middleton, "Introduction to Statistical Communication Theory", New York, McGraw-Hill, 1960.
- [33] H.L. Van Trees, "Detection, estimation and modulation theory," New York, Wiley, 1968.
- [34] S. Stergiopoulos, "Noise Normalization Technique for Beamformed Towed Array Data", *J. Acoust. Soc. Am.*, **97**(4), 2334-2345, (1995).
- [35] S. Stergiopoulos, "Influence of Underwater Environment's Coherence Properties on Sonar Signal Processing", *Proceedings of 3rd European Conference on Underwater Acoustics, FORTH-IACM*, Heraklion-Crete, **V-I**, 453-458, 1996.
- [36] F.J. Harris, "On the use of windows for harmonic analysis with discrete Fourier transform", *Proc. IEEE*, **66**, 51-83, 1978.
- [37] A. C. Dhanantwari, "Adaptive Beamforming with Near-Instantaneous Convergence for Matched Filter Processing", *Master Thesis*, Dept. of Elect. Eng., Technical University of Nova Scotia, Halifax, N.S., Canada, Sept. 1996.
- [38] J. Krolik and D.N. Swingler, "Bearing Estimation of Multiple Broadband Sources using Steered Covariance Matrices", *IEEE Trans. Acoust. Speech, Signal Proc.*, **ASSP-37**, pp. 1481-1494, 1989.

- [39] H. Wang and M. Kaveh, "Coherent signal-subspace processing for the detection and estimation of angles of arrival of multiple wideband sources", *IEEE Trans. Acoust. Speech, Signal Proc.*, **ASSP-33**, pp. 823-831, 1985.
- [40] A. Antoniou, "Digital Filters: Analysis, Design, and Applications", 2nd Ed., McGraw-Hill, NY, 1993.
- [41] A. Mohammed, "A high-resolution spectral analysis technique", DREA Memorandum **83/D**, Defence Research Establishment Atlantic, Dartmouth, N.S., Canada, 1983.
- [42] A. Mohammed, "Novel methods of digital phase shifting to achieve arbitrary values of time delays", *DREA Report 85/106*, Defence Research Establishment Atlantic, Dartmouth, N.S., Canada, 1985.
- [43] S. Stergiopoulos & A.T. Ashley, "An Experimental Evaluation of Split-Beam Processing as a Broadband Bearing Estimator for Line Array Sonar Systems", *J. Acoust. Soc. Am.*, **102**(6), 3556-3563, Dec. 1997.
- [44] L.J. Griffiths, C.W. Jim, "An Alternative Approach to Linearly Constrained Adaptive Beamforming", *IEEE Trans. on Antennas and Propagation*, **AP-30**, pp. 27-34, 1982.
- [45] D.T.M. Slock, "On the Convergence Behaviour of the LMS and the Normalized LMS Algorithms", *IEEE Trans. Acoust. Speech, Signal Proc.*, **ASSP-31**, pp. 2811-1825, 1993.
- [46] D. Middleton and R. Esposito, "Simultaneous Optimum Detection and Estimation of Signals in Noise", *IEEE Trans. of Information Theory*, **IT-14**, pp. 434-444, 1968.
- [47] P. Wille and R. Thiele, "Transverse horizontal coherence of explosive signals in shallow water", *J. Acoust. Soc. Am.*, **50**, pp. 348-353, 1971.
- [48] P.A. Bello, "Characterization of randomly time-variant linear channels", *IEEE Trans. Commun. Syst.*, **10**, pp. 360-393, 1963.
- [49] D.A. Gray, B.D.O. Anderson and R.R. Bitmead, "Towed Array Shape Estimation Using Kalman Filters - Theoretical Models", *IEEE J. Oceanic Eng.*, **18**(4), October 1993.
- [50] B.G. Ferguson, "Remedying the Effects of Array Shape Distortion on the Spatial Filtering of Acoustic Data from a Line Array of Sensors", *IEEE J. Oceanic Eng.*, **18**(4), Oct. 1993.
- [51] J.L. Riley and D.A. Gray, "Towed Array Shape Estimation Using Kalman Filters - Experimental Investigation", *IEEE J. Oceanic Eng.*, **18**(4), October 1993.
- [52] B.G. Ferguson, "Sharpness applied to the adaptive beamforming of acoustic data from a towed array of unknown shape", *J. Acoust. Soc. Am.*, **88**(6), pp. 2695-2701, 1990.
- [53] F. Lu, E. Milios and S. Stergiopoulos, "A New Towed Array Shape Estimation Method for Sonar Systems", submitted to *IEEE J. Oceanic Eng.*, July 1999.
- [54] N.C. Yen and W. Carey, "Application of synthetic-aperture processing to towed-array data", *J. Acoust. Soc. Am.*, **86**, pp. 754-765, 1989.
- [55] S. Stergiopoulos and H. Urban, "A New Passive Synthetic Aperture Technique for Towed Arrays", *IEEE J. Oceanic Eng.*, **17**(1), pp. 16-25, 1992.
- [56] V.H. MacDonald and P.M. Schulteiss, "Optimum passive bearing estimation in a spatially incoherent noise environment", *J. Acoust. Soc. Am.*, **46**(1), pp. 37-43, 1969.
- [57] G.C. Carter, "Coherence and time delay estimation", *Proc. IEEE*, **75**(2), pp. 236-255, 1987.
- [58] C.H. Knapp and G.C. Carter, "The generalized correlation method for estimation of time delay", *IEEE Trans. Acoust. Speech Signal Processing*, **ASSP-24**, pp. 320-327, 1976.

- [59] D.C. Rife and R.R. Boorstyn, "Single-tone parameter estimation from discrete-time observations", *IEEE Trans. Infor. Theory*, **20**, pp. 591-598, 1974.
- [60] Stergiopoulos S., "Handbook on Advanced Signal processing; Theory and Implementation for Sonar, Radar and Medical Imaging", CRC Press LLC, Radon, FL, Dec 2000.
- [61] Stergiopoulos S., "*Implementation of Adaptive processing in Radar & Sonars Including Multidimensional Arrays of Sensors*", Proceedings of ASAP Workshop, MIT Lincoln Lab, 1997.
- [62] Stergiopoulos S. and Dhanantwari A., "Adaptive beamforming structure for multi-dimensional ultrasound applications", **US Patent Application No. 09/718,516**, May 1998.
- [63] Detmer PR, Bashein G, Hodges T, Beach KW, Filer EP, Burns DH, Strandness DE: 3D ultrasonic image feature localization based on magnetic scanhead tracking: *in vitro* calibration and validation. *Ultrasound in Med & Biol* 20:923-936, 1994.
- [64] Elliot TL, Downey DB, Tong S, Mclean CA, Fenster A: Accuracy of prostate volume measurements in vitro using three-dimensional ultrasound. *Academic Radiology* 3:401-406, 1996.
- [65] Tong S, Downey DB, Cardinal HN, Fenster A: A three-dimensional ultrasound prostate imaging system. *Ultrasound in Med & Biol* 22:735-746, 1996.
- [66] Fenster A, Downey D: 3-Dimensional Ultrasound Imaging: A Review. *IEEE Engineering in Med. and Biol.* **15**, 41-51, 1996.
- [67] Nelson TR, Downey .D, Pretorius DH, Fenster A. *Three-Dimensional Ultrasound*. Lippincott, Williams and Wilkins, Philadelphia. 1999.
- [68] Downey, D., Fenster, A: Three-Dimensional Ultrasound: A Maturing Technology. *Ultrasound Quarterly* **14**(1), 25-39, 1998.
- [69] Fenster A., Dunne S, Chan T, Downey D: "Method and System for Constructing and Displaying Three-Dimensional Images." **US Patent No. 5,454,371**, October 3, 1995.
- [70] Picot PA, Rickey DW, Mitchell R, Rankin RN, Fenster A: Three-dimensional colour Doppler imaging. *Ultrasound in Med & Biol* 19:95-104, 1993.
- [71] Sherebrin S, Fenster A, Rankin R, Spence D: Freehand three-dimensional ultrasound: implementation and applications. *SPIE: Physics of Medical Imaging*, 2708, 296-303, 1996.
- [72] Hughes SW, Arcy TJD, Maxwell DJ, Chiu W, Milner A, Saunders JE, Shepperd RJ: Volume estimation from multiplanar 2D ultrasound images using a remote electromagnetic position and orientation. *Ultrasound in Med & Biol* 22:561-572, 1996.
- [73] Leotta DF, Detmer PR, Martin RW: Performance of a miniature magnetic position sensor for three-dimensional ultrasound imaging. *Ultrasound in Med & Biol* 23:597-609, 1997.
- [74] F. Zhang, A. Bilas, A. Dhanantwari, K.N. Plataniotis, R. Abiprojo and S. Stergiopoulos. "Parallelization and Performance of 3D Ultrasound Imaging Beamforming Algorithms on Modern Clusters". Proceedings of the 16th International Conference on Supercomputing (ICS'02), New York, June 2002.
- [75] Ishikawa I., et. al., "RWC PC Cluster II and Score Cluster System Software - High Performance Linux Cluster", Proceedings of the 5th Annual Linux Expo, 55-62, 1999.
- [76] Boden N.J., et.al., "Myrinet: A Gigabit-per-Second Local Area Network", *IEEE Micro*, 15(1):29-36, 1995.
- [77] O'Carroll F., et.al., "MPICH-PM: Design and Implementation of Zero Copy MPI for PM" Technical Report TR-97011, Real World Computing, March 1998.

- [78] FFTW library, developed at MIT, free software under the GNU General Public License (GPL), <http://www.fftw.org>.
- [79] ADUMS: Adaptive 4D Processing for Digital Ultrasound Medical Systems, a European Commission project, EC-IST-2001-34088, May, 2002.
- [80] New Roentgen: X-ray CT for Cardiac Imaging Diagnostic Applications, a European Commission project, EC-Esprit-26764, July 2000.
- [81] MITTUG: Minimally Invasive Tumor Therapy 3D Ultrasound Guided, a European Commission project, EC-IST-1999-10618, Jan. 2000.
- [82] MRI-MARCB: MRI System Development Correcting Motion Artifacts for Cardiac Diagnostic Applications, a European Commission project, EC-IST-2000-28168, August, 2001.

9. List of symbols / abbreviations / acronyms / initialisms

$()^*$	Complex Conjugate Transpose Operator
A/DC	Analog-to-Digital Converter
$A_s(f_i)$	Power spectral density of signal $s(t_i)$
α	Small positive number designed to maintain stability in NLMS adaptive algorithm
AG	Array Gain
BW	Signal Bandwidth
$b(f, \theta_s)$	Beams for conventional or adaptive beamformers, of an array steered at direction θ_s and expressed by $b(f, \theta_s) = \sum_{n=1}^N X_n(f) d_n(f, \theta_s)$
$B(f, \theta_s)$	Narrowband beam power pattern of an array expressed by $B(f, \theta_s) = b(f, \theta_s) b^*(f, \theta_s)$
$B(\theta)$	Broadband beam power pattern of an array steered at direction θ
CFAR	Constant False Alarm Rate
C	Signal blocking matrix in GSC adaptive algorithm,
c	speed of sound in a medium (i.e. human body)
DT	Detection Threshold
δ	sensor spacing for a line array receiver
d	Detection Index of Receiver Operating Characteristic (ROC) curve
$\bar{D}(f_i, \theta)$	Steering vector having its n^{th} phase term for the signal wave arrival with angle θ being expressed by $d_n(f_i, \theta) = \exp\left[j2\pi \frac{(i-1)f_s}{M} \tau_n(\theta)\right]$,
$\bar{\mathcal{E}}$	Noise vector component with n th element $\mathcal{E}_n(t_i)$ for sensor outputs (i.e. $\bar{\mathcal{X}} = \bar{\mathcal{S}} + \bar{\mathcal{E}}$)
$E\{\dots\}$	Expectation operator

ETAM	Extended Towed Array Measurements
θ	Angle of plane wave arrival with respect to an array receiver
f	Frequency in Hz
f_s	Sampling frequency
$\Phi(t_i, \theta_s)$	Steered spatial covariance matrix (STCM) in time domain
GSC	Generalized Sidelobe Canceller
\bar{h}	Vector of weights for spatial shading in beamforming process
\bar{I}	Unit vector of ones
i	Index of time samples of sensor time series, $\{x_n(t_i), i=1, 2, \dots, M\}$
\bar{k}	wavenumber parameter
k	Iteration number of adaptation process
LCMV	Linear Constraint Minimum Variance
λ	wavelength of signal with frequency f , where $c=f\lambda$
L	Size of line array expressed by $L = (N-1)\delta$
MVDR	Minimum Variance Distortionless Response
M	Number of time samples in sensor time series, where $\{x_n(t_i), i=1, 2, \dots, M\}$
μ	Convergence controlling parameter or “step size” for the NLMS algorithm.
N	Number of sensors in an array receiver, where $\{x_n(t_i), n=1, 2, \dots, N\}$
NLMS	Normalized Least Mean Square
N_e	Noise energy flux density at the receiving array
n	Index for space samples of sensor time series $\{x_n(t_i), n=1, 2, \dots, N\}$

$\xi(\theta_s, t_i)$	Beam time series, output of time-domain beamformer, $\xi(\theta_s, t_i) = \sum_{n=1}^N x_n(t_i - \tau_s)$ or formed by using FFTs and fast convolution of frequency domain beamformers, $\xi(\theta_s, t_i) = \text{IFFT}\{b(f, \theta_s)\}$
OMI	Operator-Machine Interface
P_D	Probability of Detection for ROC curves
P_{FA}	Probability of False Alarm for ROC curves
π	3.14159
$R(f_i)$	Spatial correlation matrix with elements $R_{nm}(f, d_{nm})$ for received sensor time series
$\rho_{nm}(f, \delta_{nm})$	Crosscorrelation coefficients given from, $\rho_{nm}(f, d_{nm}) = R_{nm}(f, d_{nm}) / \tilde{X}^2(f)$,
ROC	Receiver Operating Characteristic (ROC) curve
\bar{S}	signal vector whose n th element is expressed by $s_n(t_i) = s_n[t_i + \tau_n(\theta)]$
S	Spatial correlation matrix for the received signal $s_n(t_i)$
$S(f_i, \theta)$	Spatial correlation matrix for the plane wave signal in Frequency domain. It has as its n th row and m th column defined by, $S_{nm}(f_i, \theta) = A_s(f_i) d_n(f_i, \theta) d_m^*(f_i, \theta)$.
STCM	Steered Covariance Matrix
STMV	Steered Minimum Variance
SVD	Singular Value Decomposition method
$\sigma_n^2(f_i)$	Power spectral density of noise, $\varepsilon_n(t_i)$.
\bar{X}^*	Row vector of received N - sensor time series $\{x_n(t_i), n=1, 2, \dots, N\}$
$X_n(f)$	is the Fourier transform of $x_n(t_i)$
$X_n(f_i, \theta_s)$	Pre-steered sensor time series in frequency domain. In time domain are denoted by
$x_n(t_i, \tau_n(\theta_s))$	Pre-steered sensor time series in time domain

$X^2(f)$	Mean acoustic intensity of time sequences at frequency bin f
$\tau_n(\theta)$	Time delay between the 1 st and the n th sensor line array for an incoming plane wave with direction of propagation θ ,
$T(f_k, \theta)$	Diagonal steering matrix with elements those of the steering vector, $\bar{D}(f_i, \theta)$
$\bar{W}(f_i, \theta)$	Adaptive steering vector
ω	Frequency in radians/second
$\bar{Z}(f_i, \theta_s)$	Result of the signal blocking matrix C being applied to presteered sensor time series
	$\bar{X}(f_i, \theta_s)$

DOCUMENT CONTROL DATA SHEET

1a. PERFORMING AGENCY

DRDC Toronto

2. SECURITY CLASSIFICATION

UNCLASSIFIED
Unlimited distribution -

1b. PUBLISHING AGENCY

DRDC Toronto

3. TITLE

(U) Advanced beamformers for 3D ultrasound systems deploying linear and planar phased array probes

4. AUTHORS

Stergios Stergiopoulos, Amar Dhanantwari

5. DATE OF PUBLICATION

May 10 , 2002

6. NO. OF PAGES

95

7. DESCRIPTIVE NOTES

8. SPONSORING/MONITORING/CONTRACTING/TASKING AGENCY

Sponsoring Agency:

Monitoring Agency:

Contracting Agency :

Tasking Agency:

9. ORIGINATORS DOCUMENT NO.

Technical Report TR 2002 058

10. CONTRACT GRANT AND/OR
PROJECT NO.

6ca31

11. OTHER DOCUMENT NOS.

12. DOCUMENT RELEASABILITY

Unlimited distribution

13. DOCUMENT ANNOUNCEMENT

Unlimited announcement

14. ABSTRACT

(U) The present report outlines the development of an advanced digital ultrasound imaging technology leading to a next-generation field-portable 4D diagnostic imaging system. The proposed technology consists of:

- „h Adaptive beamforming schemes [1-6] to provide high image-resolution for ultrasound diagnostic systems
- „h 3D visualization imaging techniques to assist imaging during field-deployable minimally invasive operations
- „h time-reversal pulse design for ultrasound signals to eliminate aberration effects, which cause fuzziness in reconstructed ultrasound images; and
- „h investigations on computing architectures and planar ultrasound sensor arrays allowing system integration of the proposed technologies as a compact-portable system for field-deployable operations.

The aim is to investigate a new ultrasonic sensing and imaging technology that would lead to the design of portable, compact and field deployable 3D ultrasound diagnostic systems. The performance characteristics of the proposed diagnostic systems include minimization of the aberration effects and significant improvement in image resolution to allow for tissue identification and 3D tomographic imaging of internal body-organs. The adaptive processing schemes of this study are characterized as Dual-Use technologies and have been tested in operational active sonars of the Canadian Navy [1,4-6]. Real data results have shown that they provide array gain improvements for signals embedded in anisotropic noise fields, similar to those in the human body.

15. KEYWORDS, DESCRIPTORS or IDENTIFIERS

(U) 3D ultrasound; adaptive beamformers, linear ultrasoun dprobes, plannar array ultrasound probes, phased array ultrasound probes

Defence R&D Canada

Canada's leader in defence
and national security R&D

R & D pour la défense Canada

Chef de file au Canada en R & D
pour la défense et la sécurité nationale



www.drdc-rddc.gc.ca

